

RICE UNIVERSITY

Ion Dynamics in Strongly Coupled Plasmas

by

Sampad Laha

A THESIS SUBMITTED
IN PARTIAL FULFILLMENT OF THE
REQUIREMENTS FOR THE DEGREE

Doctor of Philosophy

APPROVED, THESIS COMMITTEE:

Thomas C. Killian, Chair
Associate Professor of Physics and Astronomy

F. Barry Dunning
Sam and Helen Worden Professor of Physics

Junichiro Kono
Associate Professor of Elec & Comp Engineering

HOUSTON, TEXAS

AUGUST 2007

Abstract

Ion Dynamics in Strongly Coupled Plasmas by

Sampad Laha

A study of ion dynamics in strongly coupled ultracold neutral plasma (UCNP) is presented here. Plasma is created by photo-ionizing laser-cooled Sr atoms. Immediately after photo-ionization, the correlation between the ion and the electron temperature and density dictate the evolution of the plasma. By extracting the ion's total energy and temperature, and studying their variation with position and time we can get information about the dynamics of the plasma. To do this we use absorption imaging, and for the first time in UCNP, fluorescence imaging and spectroscopic diagnostics, the results of which are presented in this thesis. Using the imaging techniques, we can also study the size change of the plasma with time, which is described by an exact solution of the Vlasov equations for appropriate initial conditions. Also, using fluorescence imaging and spatially resolved spectroscopy, we are able to separate the thermal temperature of ions from the kinetic energy due to expansion and show that the temperature of ions decreases at later times due to adiabatic cooling.

Acknowledgments

First and foremost, I would like to take this opportunity to acknowledge the support and guidance that I got from my advisor, Prof. Thomas Killian. From him, I learned not only about physics, but also how to plan things for the future. I would like to thank him especially for his faith and patience with me and for constant appreciation of my good works. Rice has been a stepping stone in my career, and no matter what I do in future, Tom would have a special value in my endeavors.

I would also like to thank my committee members, Prof. F. Barry Dunning and Prof. Junichiro Kono for agreeing to review my work. I would also like to thank the funding agencies Research Corp, Sloan Foundation, Packard Foundation, Department of energy, and National Science Foundation, without whose money, perhaps, this research would not have seen the light of the day.

I would also like to thank all my lab mates in keeping such a playful and fun-loving atmosphere in the lab. Everybody in the lab has made this lab a place worth working at. Clayton and Sarah, thanks for the companionship that you have given me throughout the six years. Pascal, I would never forget your jokes, and Natali, I would never get tired of teasing you. Also, my research would really have been a hard task if I had not got the help of Ying Chen and then Hong Gao. Jose, Dan, Andrew, Aditya, lab would not have been such a joyful place if you guys were not there.

This research and my life in general would have remained incomplete had it not been for my parents and my wife, Anushree. My parents had always relentlessly

supported and encouraged me for getting better education right from my childhood. My wife has been there through thick and thin of my life. Her support and love had been very vital throughout all my days, without which the rewards of accomplishing something, would have been negligible.

There were also my numerous friends, Arnab Chakrabarti, Joy, Ravi, Nachiappan, Janardan, Arnab Mukherjee, just to name a few, who were also there in my good and bad times and with whom no time seemed long enough.

Contents

1	Introduction to Ultracold neutral plasma	1
2	Creation of ultracold neutral plasma	3
2.1	Laser cooling and trapping of atoms	3
2.2	Photoionization of MOT	7
2.3	Some previous works on UCNP	10
3	Ion dynamics	13
3.1	Disorder induced heating	14
3.2	Kinetic energy oscillations of ions in UCNP	18
3.3	Suppression of oscillations due to dephasing	20
3.4	Expansion of ions in UCNP	22
4	Diagnostics of UCNP - Absorption Imaging and spectroscopy	29
4.1	Introduction	29
4.2	Importance of optical imaging	29
4.3	Brief introduction of absorption and fluorescence	31
4.3.1	Electronic levels of Sr ion	32
4.4	Generating the spectrum for absorption	35
4.5	Spectrum with expansion and annular analysis	37
4.5.1	Obtaining the spectrum and T_{eff} experimentally	41
5	Results - Annular analysis of absorption data	43
5.1	Spectrum of annular regions	43
5.2	Number and density distribution of ions	44
5.3	Spatial distribution of thermal temperature	48
5.4	Results-Rydberg atoms	53
6	Diagnostics of UCNP - Fluorescence Imaging and spectroscopy	59
6.1	Introduction	59
6.2	Importance of fluorescence imaging	60
6.3	Fluorescence imaging	62
6.4	Fluorescence spectroscopy	68
6.4.1	Spectrum without approximating G_1 and G_2 to 1	70
6.5	Saturation of the fluorescing level	71
6.6	Positioning the camera on image plane	72

7	Results-Fluorescence Data	75
7.1	Size expansion of the plasma	75
7.2	Fluorescence spectrum and temperature determination	79
7.3	Spatially resolved spectroscopy	82
7.3.1	Checking for increase in observed temperature due to re-absorption of fluorescence signal	90
7.3.2	Checking for expansion effect in the experimental thermal tem- perature	91
8	Conclusion	98
A	Code to calculate T_i using equation 3.1	100
B	Analysis of plasma image strip with smaller strip width	105
C	Experimental Realization of an Exact Solution to the Vlasov Equa- tions for an Expanding Plasma	109

List of Figures

2.1	Momenta exchange between photon and atom	4
2.2	Energy level of Sr atom	6
2.3	Schematic of MOT setup	7
3.1	Disorder induced heating	14
3.2	Variation of DIH temperature	16
3.3	Thermal temperature versus temperature	17
3.4	Dephasing of ion oscillations	21
3.5	Expanding plasma	23
4.1	Set-up of 422 nm imaging system	32
4.2	Sr ion energy level diagram	33
4.3	Absorption imaging of Sr ion	36
4.4	Spatially-resolved absorption imaging.	38
4.5	Analyzing annular regions	42
5.1	Spectra of annular regions	44
5.2	Number variation with ρ for various times	46
5.3	Areal density variation with ρ for various times	47
5.4	Temperature versus ρ evolution with time	49
5.5	Temperature versus ρ evolution with time	50
5.6	T_i versus ρ evolution for later times	52
5.7	Number distribution of Rydberg atoms with respect to ρ	54
5.8	Comparing T_{eff} versus ρ evolution for Rydberg atoms with normal plasma.	56
5.9	Comparing T_{eff} versus ρ evolution for Rydberg atoms with normal plasma.	57
5.10	Comparing T_{eff} versus ρ evolution for Rydberg atoms with normal plasma.	58
5.11	Comparing T_{eff} versus ρ evolution for Rydberg atoms with normal plasma.	58
6.1	Fluorescence imaging of Sr ion	62
6.2	Observing plasma by fluorescence imaging.	66
6.3	Size correction along the x-axis.	67
6.4	Finding average value of z	69
6.5	Fluorescence spectra of regions.	70
6.6	Fluorescence signal versus laser power plot.	72
6.7	Imaging lens setup	73

6.8	Sheet fluorescence image on the camera	74
7.1	Density profile of the plasma	76
7.2	Density profile of the plasma	77
7.3	Density profile of the plasma	78
7.4	Plasma size versus time	80
7.5	Spectra plots versus time	81
7.6	RMS velocity versus time	83
7.7	Thermal temperature of ions	85
7.8	Thermal temperature of ions	85
7.9	Thermal temperature of ions	86
7.10	Variation of electron-ion collision rate	87
7.11	Observed thermal temperature with re-absorption of fluorescence signal	91
7.12	Thermal temperature after increasing the width of the spatial region.	92
7.13	Thermal temperature after increasing the width of the spatial region.	94
7.14	Thermal temperature variation in outer regions.	95
7.15	Thermal temperature variation in outer regions.	96
7.16	Calculating thermal temperature with modified cooling and EIC rates.	97
7.17	Calculating thermal temperature with modified cooling and EIC rates.	97
B.1	Density profile of the plasma	106
B.2	Density profile of the plasma	107
B.3	Density profile of the plasma	108
C.1	Recording fluorescence of UNPs.	114
C.2	Evolution of the areal density of plasma	116
C.3	Evolution of the plasma size.	118
C.4	Sample spectrum and evolution of the rms ion velocity.	119

List of Tables

Chapter 1

Introduction to Ultracold neutral plasma

Plasma is a collection of positively and negatively charged particles and is the most widely existing state of visible matter in the universe. Most naturally occurring plasmas, like our Sun, or lightning, have a very high temperature because it requires energy to have the attracting charges separated. High temperature of the plasma implies that the kinetic energy of the constituent charged particle is greater than the electrostatic Coulomb interaction among them. This prevents development of any short or long range coupling between the particles, and thus a lot of collective features in the plasma are not present in these plasma. This type of plasma is usually categorized by defining a quantity called the Coulomb Coupling Parameter (Γ) which is given as the ratio of the average Coulomb energy over the average thermal temperature. If a is the average particle distance distance and T the thermal temperature of a plasma, then, $\Gamma = (1/4\pi\epsilon_0) (q^2/ak_B T)$, where, q is the charge of the species. In the above mentioned plasmas, $\Gamma < 1$, which implies weak Coulomb coupling, and thus, this type of plasmas are called weakly coupled plasma.

There is another type of plasma where the coulomb interaction between the con-

stituents can be higher than the kinetic energy ($\Gamma > 1$). This type of plasma is called strongly coupled plasma [1] and they can have short and/or long range coupling among its constituents. This results in observation of collective features like Coulomb crystals [2], thermal oscillations [3], etc. Typical examples of this type of plasma occurring naturally are white dwarf and neutron stars. Although these stars have very high temperature, very massive gravity collapses these stars to extremely high densities, and that's how their inter-particle distances are small, which results in the higher coulomb interaction.

Another way of getting strongly coupled plasma in the laboratory itself is by reducing the temperature of the plasma, thereby reducing its kinetic energy. This type of plasma is called ultracold plasma. Usually, this type of plasma is electrically neutral, and is thus also called ultracold neutral plasma (UCNP). To obtain ultracold plasmas, atoms are first cooled using laser cooling and trapping, a technique without which ultracold plasma would not probably have existed and which is discussed briefly in the following section. After this, the atoms are photo-ionized with another laser to get ultracold neutral plasma [4]. Although by laser cooling and trapping, atoms can be cooled to as low as pK temperatures [5], to obtain ultracold plasmas, atoms need to be cooled to only about mK temperature before being photo-ionized. This is because after photoionization, the ions in the plasma reach an equilibrium temperature of the order of a Kelvin in just a couple of hundred nano-seconds [6].

Chapter 2

Creation of ultracold neutral plasma

This chapter talks about the two main processes that are involved in creation of ultracold plasma. The first is laser cooling and trapping of atoms to get a MOT (magneto-optical trap). The second is to photoionize the trapped atom to get a neutral plasma, whose initial temperature of the ions is the same as that of the cold trapped atoms. In the end of this chapter we will also learn about some of the previous work done on UCNP.

2.1 Laser cooling and trapping of atoms

The technique of laser cooling is very deeply based on the fact that any wave (here, photons) have momentum too. Thus, when light interacts with matter (atoms), it not only exchanges its energy, but momentum too. An atom thus goes to a higher excited state because it absorb's the light's energy, but also gets a kick because of light's momentum. It is true that the atom re-emits the absorbed photon at a later time (spontaneous emission), but since this process is random, the average momentum change due to lot of spontaneous emissions of a single atom amounts to zero. If the

light used is a laser, the photons have almost the same momenta (both magnitude and direction), and thus, the momentum of the atoms could be changed in a specific direction. For example, Fig. 2.1 shows collision of an atom having velocity v_0 , mass m and a photon having angular frequency ω and angular wavenumber k . The photon will have a momentum of $\hbar k$ and thus the atom's velocity will change by an amount $\hbar k/m$ after the head on collision.

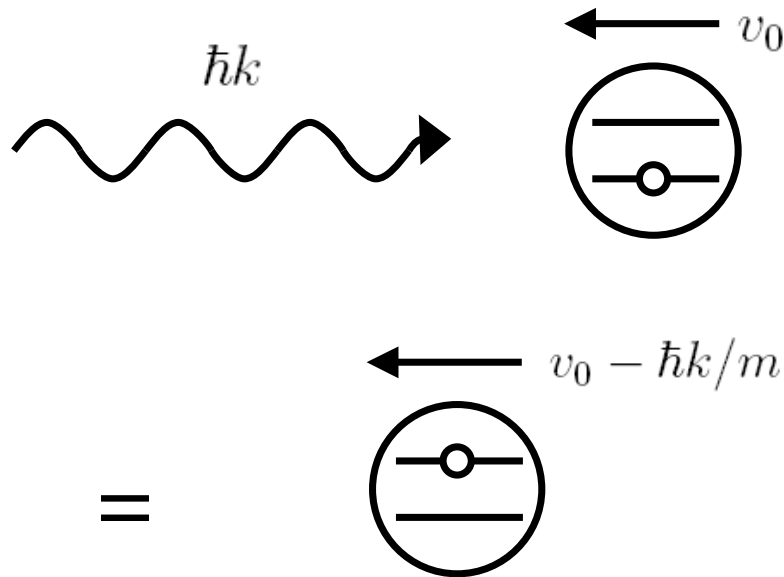


Figure 2.1: Slowing of the atoms by bombardment of photons. This happens due to momentum exchange during the collision. The electron in the lower state absorbs the photon and goes to the excited state.

Technologically, the process of laser cooling is far more involved, but the key concept remains the same. The first step in laser cooling is deceleration of an atomic beam, which has very wide velocity spreads and due to Doppler shifts a laser resonant to the atomic transition won't be so effective to slow the whole atomic beam. To achieve cooling over the wide spread of velocities, the laser frequency can be changed constantly so that it can interact with various velocity classes. This technique is

called “chirp-cooling”, and was first experimentally demonstrated by Ertmer et al. in 1985 [7]. Another technique that is used in beam deceleration is called Zeeman cooling. In this technique, the atoms are passed through a varying magnetic field so that the change in Zeeman shift of the atomic frequency compensates the changing Doppler shift of the atoms as they cool [8]. For the cooling to work, the magnetic field is maximum (say, B_0) where atomic velocity is the highest (say, v_0). Then the magnetic field is slowly decreased to compensate for the decreasing velocity. The frequency of the laser is set so that it is resonant with atoms having velocity v_0 and zeeman shift corresponding to the magnetic field B_0 . This also implies that the laser has to be red-detuned because the Doppler shift usually exceeds the Zeeman shift. In our lab too, we use Zeeman cooling as the primary way of cooling the atomic beam, where the 461 nm transition ($^1S_0 \rightarrow ^1P_1$) of Sr atom (Fig. 2.2) is used as the primary cooling transition. The 461 nm light is produced from a frequency doubled 922 nm Ti:Saph laser and is red detuned to 580 MHz frequency, which slows the atoms down from a peak value of 280 m/s to about 50 m/s.

Once the atomic beam is slowed down, the atoms need to be slowed down further to get ultracold atoms. Different groups have been successful in trapping neutral atoms using magnetic means [9], and optical means [10], but the most commonly used trapping method is a combination of both which is usually referred to as magneto-optical trap (MOT). This type of cooling was first experimentally shown in 1987 [11]. Atoms are trapped in a magnetic field and between counter-propagating laser beams

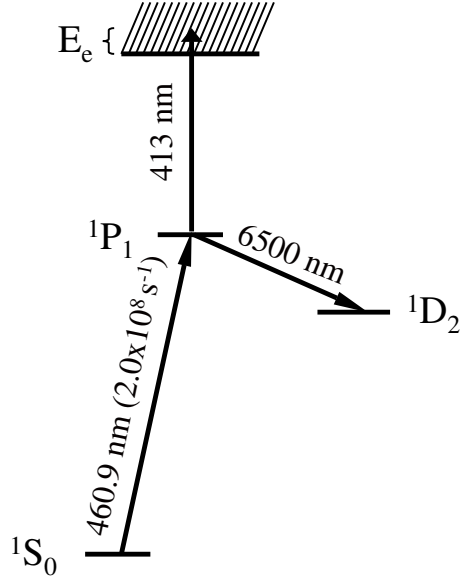


Figure 2.2: Energy level diagram of Strontium atom. The 460.9 nm transition is used as the main transition to optically trap Strontium. The shaded region is the continuum where the electron can have positive energy.

having opposite circular polarization. The laser beams are also red-detuned, that is, their frequency is smaller than the zero-velocity atomic resonance frequency. A typical setup that is used in our lab is shown in Fig. 2.3, where the beams propagate in three orthogonal cartesian axes. The laser used for our Sr MOT is 461 nm and it is red-detuned by about 55 MHz so that the laser can be in resonance with the atoms moving toward the laser. The idea of magneto-optical trap is to split the degeneracy of the excited level by a magnetic field gradient. We produce a magnetic field gradient of 115 G/cm , (with the zero at what will be the center of the trap) by using water cooled coils in anti-helmholtz configuration. The magnetic field not only splits the excited energy level, but it also produces a gradient in the energy level. And given the fact that the σ_+ and σ_- polarized light interacts with the positive and negative

m_j levels respectively, by carefully choosing the directions of the polarized light, the atoms can be made to trap toward the center. A very good explanation of this process is given in the book “Laser cooling and trapping“, by Metcalf and Straten [12]. By using the magneto-optical trapping technique, in our lab we trap about 400 million Sr atoms having densities of the order of $10^{15} - 10^{16} \text{ m}^{-3}$, and a temperature of about 10 mK [13]. This density and temperature is perfect to ionize the atoms to get strongly coupled ultracold plasma.

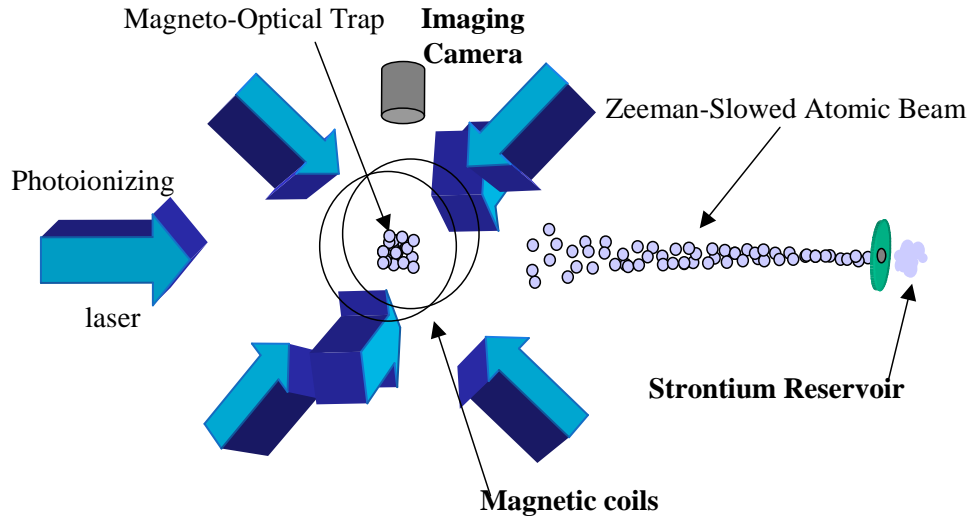


Figure 2.3: Figure showing a typical setup to get Sr atom MOT and then to photoionize the MOT to get ultracold plasma.

2.2 Photoionization of MOT

Atoms can be photoionized to get ions. In our case, the photoionization process is a two step one. During the cooling and trapping of Sr atoms, some atoms are already there in the excited 1P_1 state. After letting the MOT expand to get the desired density, the population of the 1P_1 state is increased by shining a 10 ns pulsed

laser (which has peak intensity of 25 W/cm²) tuned to the ¹S₀ → ¹P₁ transition. In the same instance, another 10 ns pulsed dye laser is used to ionize the atoms in the ¹P₁ state. By this technique of pulsed amplification process, we are able to achieve an ionization fraction of about 60 %. Because of the small electron-to-ion mass ratio, most of the dye laser photon's energy is transferred to the electron's kinetic energy, E_e , during the photoionization. Assuming the electrons to be a free gas with three degrees of freedom, its temperature can be calculated using the formula

$$E_e = \frac{3}{2}k_B T_e = h\nu_{laser} - \Phi_{IP}, \quad (2.1)$$

where, ν_{laser} is the frequency of the photo-ionizing laser and $\Phi_{IP} = 4.819 \times 10^{-19}$ J, is the ionization potential of the ¹P₁ state. In our experiments, $2E_e/3k_B$ can be as small as 67 mK, which is the bandwidth of the laser [14]. Usual value of $2E_e/3k_B$ in our experiments range from about 10 K to 150 K, but the data presented in this thesis will be mostly limited to about 50 to 100 K range so that some radiative and three body recombination process could be minimized.

It should be added here that by using the photo-ionizing laser, not only can plasma be produced, but if we tune the energy of the laser to slightly below the ionization threshold, we can get atoms with very high values of principal quantum number. These atoms are called Rydberg atoms [15] and they also play an important role for plasma evolution. Studies have revealed that just by blackbody radiation and collisions Rydberg atoms can spontaneously evolve into plasma [16]. Rydberg atoms

are also the final product of a process called three body recombination (TBR), where, an ion in a plasma interacts with two electrons and results in a Rydberg atom and an electron, which carries off the extra energy [17]. This process plays a significant role in ion number loss and electron heating. Thus, study of Rydberg atoms is necessary in order to get a complete picture of ion dynamics. Our system gives us a tool by which we can produce plasma and/or Rydberg atoms by controlling the photo-ionizing laser frequency and study both their properties and evolutions.

Immediately after photoionization, the ions have the same initial shape and size of the MOT. The atom density has a gaussian distribution over space,

$$n_i(r) = n_0 \exp(-r^2/2\sigma^2), \quad (2.2)$$

with $\sigma \simeq 10^{-3}$ m and peak density, $n_0 \simeq 10^{16}$ m⁻³. Thus, the ions also have this Gaussian distribution of shape. This variation of density with position brings in a lot of significant effects in the ion dynamics, which are discussed in the following chapter. The number of atoms in the trap and number of ions is different though. Owing to about 40-60 % ionization fraction, the number of ions is roughly 200 million, given the fact that the rough number of atoms in the trap is 400 million.

The ions initially have similar temperature as the atoms, which is about 10 mK. This is due to the fact that the ions are about 20000 times more massive than electrons. But the ions soon attain an equilibrium temperature of about 1 K in a couple of hundred nano-seconds due to disorder induced heating (DIH) [6]. This happens

because immediately after formation, the atoms are not correlated in space, and thus, their potential energy is quite high. They soon start going into a more ordered state which has lesser potential energy. Since the process is adiabatic, the kinetic energy goes up thus bringing the temperature to about 1 K. Apart from DIH, there are whole lot of other phenomena that happen during the plasma evolution, like, kinetic energy oscillations, suppression of the oscillations due to dephasing, and plasma expansion. All of these processes are discussed in detail in the next chapter, as all of them play important role in plasma evolution and are very important to study.

2.3 Some previous works on UCNP

After creation of UCNP in National Institute of Standards and Technology, Gaithersburg, by Killian *et al.* [4], lot of experimental and theoretical work on UNCPS have come into prominence. The main feature of UCNP is the high precision control of the initial experimental parameters. The initial electron temperature in this type of plasma can be varied from about 1-1000 K, which depends mostly on the frequency of the photoionizing laser. As mentioned in the previous section, the ionic temperature is about 1 K and the peak density is of the order of 10^{16} m^{-3} .

By studying UNCPS in general and some of its key properties (like temperature, size, density), we can gather lot of information about the key physics that plays a deep role in the formation and evolution of the plasmas. For example, from fluorescence measurements, the density profile of calcium plasma was obtained [18], and from that

the authors were able to conclude that the plasma was strongly coupled in nature. In fact, in the creation of UCNP paper [4], the authors used electric field measurements to conclude that the plasma was strongly coupled.

There has been lot of work on strongly coupled plasma which manifest of lot of interesting physics like collective modes [19] and Coulomb crystals [2]. Achieving ultracold plasma by experiments not only gives a chance to study these interesting phenomenon, but it also lends some insight into plasma behavior in fusion reaction experiments.

Studying plasma expansion [20, 21, 22, 23, 24] can also give us a lot of information about plasma dynamics in general and electron, ion temperature in particular. For example, in [24, 25], study of electron temperature has been used as an aid to understand plasma expansion. Some type of plasma expansion in UCNP also satisfies a particular condition for solutions to Vlasov equation [26] which is experimentally verified in [27]. Vlasov equations are very important for the kinetic theory of plasma and its solutions are very important to study expansion of plasma into a vacuum, a problem which has received tremendous focus in the past few decades, both theoretically [28, 29, 30] and experimentally [31, 32] and both [33].

The dynamics of UCNP could be understood by not only understanding the behavior of the electron temperature, but also the ion temperature. For example, from [20, 34, 3], we can see the direct manifestation of disorder induced heating (DIH) [6] onto the temperature of the ions. Also, [34, 3] go one step ahead to show the

presence of localized kinetic energy oscillations in the plasma, which tells a lot about the nature of Coulombic interactions in the system.

Numerical modeling of UCNP [35] has shown that if the ions undergo adiabatic cooling, then plasma expansion can be used to get very highly coupled plasma, in spite of the low Coulomb coupling parameter due to DIH. Here, we have used absorption and fluorescence imaging techniques to extract the ion thermal temperature and we try to verify if the ions really undergo adiabatic cooling.

Chapter 3

Ion dynamics

This chapter looks into the processes that go through in a plasma while they evolve in time. For example, the moment ultracold plasma is formed, Coulomb interactions between the charges determine the evolution of the plasma. During this time, the ions gain kinetic energy by a process called disorder induced heating. When they form, the ions' spatial arrangement does not favor a minimum potential energy configuration. Thus, the ions move to attain minimum potential configuration, and while they are moving, they might overshoot their equilibrium position too. This gives rise to localized motional oscillations in the plasma. As far as the electrons are concerned, they thermalize immediately after plasma formation, a topic covered in Priya Gupta's PhD thesis [36]. Owing to their lower mass than the ions, the electrons share most of the ionizing photon's energy. This means that the electrons are highly energetic, and thus the electrons' pressure causes the whole plasma to expand. By knowing how and when these physical processes happen in time, we can know a lot about the physics of the plasma, making these processes an integral part of study of plasma dynamics.

3.1 Disorder induced heating

In plasmas formed by photoionizing laser-cooled atoms [4], the ions have relatively low kinetic energy immediately after formation as most of the photon's energy is carried off by the electrons. However, the ions' spatial distribution remains uncorrelated and they have a higher Coulombic potential energy than in thermodynamic equilibrium. To lower their potential energy, ions move to a more ordered and correlated state. This process happens in an adiabatic environment, and so, the total energy has to be conserved. Thus, the kinetic energy of ions increases, heating up the ions in the ultracold plasma to an equilibrium temperature. This phenomenon of heating is called disorder induced heating (DIH) and it was first predicted in [6] and observed experimentally in [20]. A schematic of DIH is shown in Fig. 3.1.

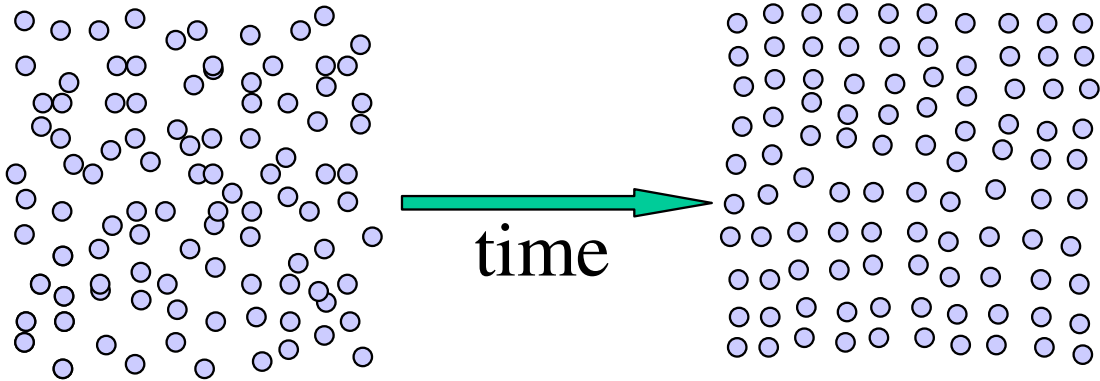


Figure 3.1: The ions start off with highly uncorrelated state where their potential energy is higher than that of equilibrium. Due to this, they go over to a lower potential state, which is a more correlated arrangement. Since the whole process is adiabatic, the kinetic energy of the ions increases, heating up the plasma.

It has been already pointed out that the temperature of the electrons far exceeds that of the ions. This means that the coupling between them and also between

them and ions would be negligible. In this case, the electrons screen the Coulomb interactions between the ions, and the ions interact with each other through the Yukawa potential model, $U(r) = e^2 \exp(-r/\lambda_D)/r$, where $\lambda_D = \sqrt{\epsilon_0 k_B T_e / n_e e^2}$ is the electron Debye screening length. In these conditions and assuming complete disorder in the initial state, it has been shown in [6] that the equilibrium temperature due to DIH is given as [6]

$$T_i = \frac{2}{3} \frac{e^2}{4\pi\epsilon_0 a k_B} \left| \tilde{U}(\kappa, \Gamma_i) + \frac{\kappa(n_i, T_e)}{2} \right|. \quad (3.1)$$

Here, T_e is the electron temperature, $n_e \simeq n_i$ is the density of electrons and ions respectively, $a = (3/4\pi n_i)^{1/3}$ is the inter particle distance, $\kappa = a/\lambda_D$, and $\Gamma_i = e^2/4\pi\epsilon_0 a k_B T_i$ is the coulomb coupling parameter for the ions. For a typical density of $5 \times 10^{15} \text{ m}^{-3}$ and $T_e = 50 \text{ K}$, the inter particle distance has a value of $3.6 \mu\text{m}$ and that of λ_D is $7 \mu\text{m}$, and these values makes Γ_i equal to about 3, which puts the plasma in the strongly coupled regime. Also in the above equation, \tilde{U} , the excess potential energy per particle in units of $e^2/4\pi\epsilon_0 a$, is tabulated in [37] using a molecular dynamics simulation.

It should be noted from Eqn. 3.1 that T_i varies with density as well as electron temperature. In fact, Eqn. 3.1 can be solved numerically using iterative techniques (Appendix A) and values of T_i for different densities and electron temperatures can be calculated. Figure 3.2 shows the typical variation for the range of values that we mostly use in our experiments. As can be seen from the figure, the DIH temperature increases with increasing density, because this decreases the inter particle spacing and

thus more Coulomb interactions heat up the ions. It can also be observed from the figure that since increasing electron temperature decreases their screening, Coulomb forces between the ions become stronger which increases the DIH temperature.

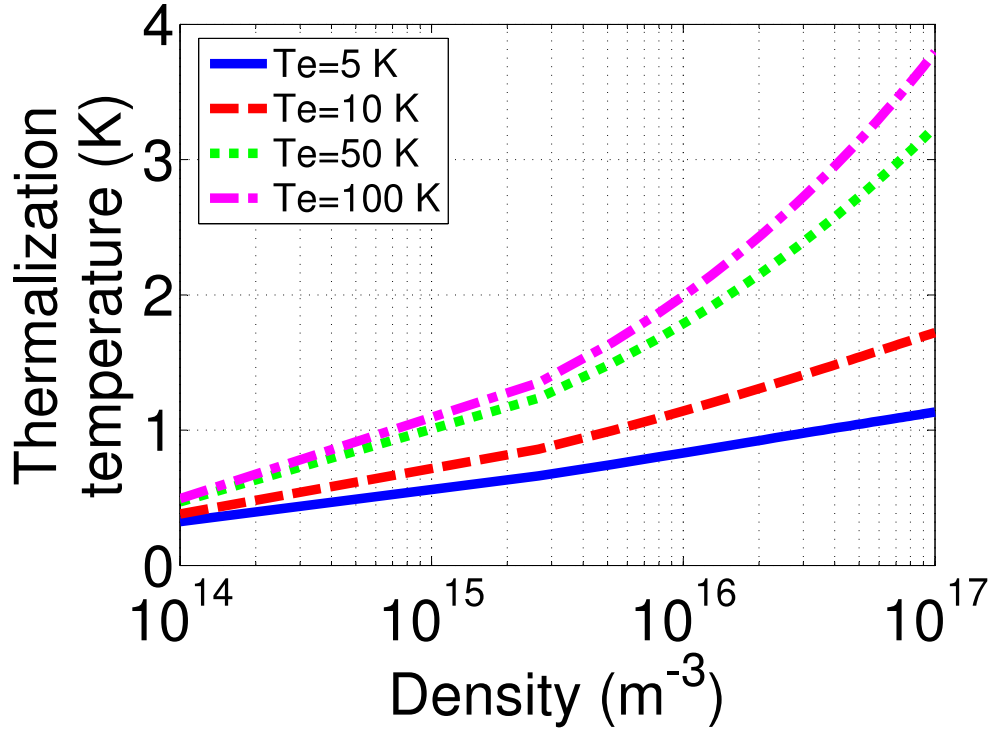


Figure 3.2: Variation of equilibrium temperature due to DIH for various values of density and electron temperature.

Equation 3.1 was confirmed experimentally in [20, 34, 3]. In [34], a study of the effect of electron screening on the ion temperature was done. From that work, it can be seen that when the electron screening is low, the DIH equilibrium temperature is higher. This points to the fact that this type of heating is indeed due to Coulomb interactions of the ions. In [3], Eqn. 3.1 was used to calculate the thermal temperature of the ions, and it can be seen from Fig. 3.3 that the fitted curve (where, the density, electron temperature, size of the plasma, and a damping factor were used as the

fitting parameters) agreed very well with the data.

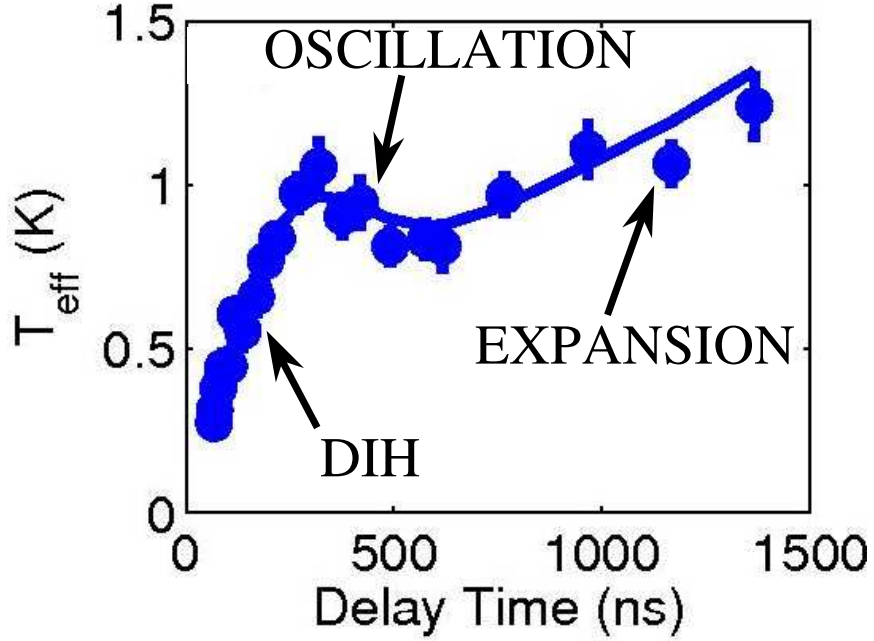


Figure 3.3: This figure has been taken from [3]. The points are temperature data and the continuous curve is a fit which uses Eqn. 3.1 to calculate the DIH equilibrium temperature. Also, it should be noted that instead of saturating to the DIH equilibrium value, the temperature shows local maximum and minimum with respect to time, hinting toward the presence of local thermal oscillations in the plasma.

As can be seen from Fig. 3.3, it takes finite amount of time for the ions to reach DIH equilibrium temperature (about 1K in this case). This amount of time is also another characteristic of the plasma. An ion in a plasma responds according to the Coulomb potential that is created due to the other ions. This characteristic time of response is usually termed the ion plasma frequency and is given by $\omega_{pi} = \sqrt{n_{0i}e^2/m_i\epsilon_0}$, where, n_{0i} is the ion-density and m_i is the mass of the ion. From simple classical arguments, it can also be seen that ω_{pi} is the inverse of time that an ion takes to travel through a rough distance of $a = (3/4\pi n_i)^{1/3}$ under a Coulomb force of $(1/4\pi\epsilon_0)(e^2/a^2)$. From the plasma frequency expression it can also be seen that a plasma’s “response time“

will be quicker (higher ω_{pi}) if the density is higher. This means that the nearest neighbor distance of the ions is smaller, thus implying increased Coulomb interactions. This shows that the plasma ion frequency does have origins in Coulombic interactions.

The fact that the ion temperature due to DIH does not instantly reach equilibrium, but depends on the response time of the plasma, which has its origin in a radial restoring force leads to the question of whether the ion temperature will stop changing once it has reached its DIH equilibrium value. In fact, from Fig. 3.3 it is clearly seen that the temperature has a local maximum at about 300ns, and then a local minimum at 600 ns. It should also be pointed out that in the experimental condition in [3], $2\pi/\omega_{pi}$ is about equal to 600 ns. This suggests that the ions could be undergoing kinetic energy oscillations in reaching equilibrium. The next section throws some light on these types of oscillations as we can infer a lot about the plasma characteristics and dynamics by studying them.

3.2 Kinetic energy oscillations of ions in UCNP

Plasma by definition is a collection of charged particles that are free to move by external influence. If the equilibrium condition is changed inside a plasma, the particles will try to reach equilibrium again, and this is what gives rise to any kind of oscillation. If we consider electrons in the plasma, then it is easy to show that a displacement of the electrons from the ions results in a restoring simple harmonic force, and the electrons undergo oscillations whose frequency is given by $\omega_{pe} = \sqrt{n_0 e^2 / m_e \epsilon_0}$. This

quantity is called the electron plasma frequency [38], and is the resonant frequency of oscillation at which the electrons in a plasma would oscillate.

The situation is different in the case of ion motion. Ion-plasma oscillations are observed only when the wave vector, $k > 1/\lambda_D$, where, $\lambda_D = \frac{1}{\omega_{pe}} \sqrt{k_B T_e / m_e}$ is the electron Debye screening length with T_e being the electron temperature. When $k > 1/\lambda_D$, the electrons are not effective in screening out the coulombic force between the ions. The concept of ion-oscillations can be understood from the dispersion relationship of ion acoustic waves in a two component plasma, given by [39]

$$1 - \frac{\omega_{pe}^2}{\omega^2 - k^2 v_e^2} - \frac{\omega_{pi}^2}{\omega^2 - k^2 v_i^2} = 0, \quad (3.2)$$

where, $k = 2\pi/\lambda$ is the wave vector and $v_{e,i} \simeq \sqrt{k_B T_{e,i} / m_{e,i}}$ are the electron and ion thermal velocities. Assuming that $\omega \ll \omega_{pe}$ and $T_e \gg T_i$, which results in the approximation $v_i \ll \omega/k \ll v_e$, the dispersion relation becomes,

$$1 + \frac{\omega_{pe}^2}{k^2 v_e^2} - \frac{\omega_{pi}^2}{\omega^2} = 0 \quad (3.3)$$

$$\Rightarrow 1 + \frac{1}{k^2 \lambda_D^2} - \frac{\omega_{pi}^2}{\omega^2} = 0 \quad (3.4)$$

$$\Rightarrow \omega = \omega_{pi} \sqrt{\frac{k^2 \lambda_D^2}{1 + k^2 \lambda_D^2}}. \quad (3.5)$$

It is clear from the above equation that at large values of k , the frequency of the wave approaches the ion plasma frequency, ω_{pi} . This is because $k = 2\pi/\lambda \simeq 2\pi/a$, and increasing k would mean decreasing the inter-ionic distance a , which means that

there will be fewer electrons between the ions to screen their interaction, and the ions would undergo local thermal oscillations in their own potential field. A rough physical insight into these oscillations can be found in [40], where a small derivation has been done to show the presence of these kind of oscillations if the ions were to be in a body centered cube (BCC) configuration. Plasma ion oscillations are very important phenomenon because by studying these oscillations we can comment a lot about the electron screening in general and the plasma density in particular.

3.3 Suppression of oscillations due to dephasing

Once it is established that the ion velocity undergoes characteristic oscillations with frequency $\omega_{pi} = \sqrt{n(r)e^2/m_i\epsilon_0}$, it should be noted that the ion density, $n(r)$, is not a constant. In fact, as pointed out earlier, the density profile has the same Gaussian form as the neutral MOT, where, $n(r) = n_0\exp(-r^2/2\sigma^2)$. This variation of density with position varies the plasma frequency with position too. This would mean in the plasma, that would be a superposition of infinite waves of uncorrelated frequency. The random frequency of these waves brings down the amplitude of the resultant superposed wave, a phenomenon called dephasing. Figure 3.4 shows this phenomenon graphically. There are three ordinary sinusoidal waves (represented by the non-continuous lines), which don't show any damping individually. The waves have the same initial phase, but different frequencies. But when lots of such sinusoids are added up, the amplitude of the resulting wave (continuous line) decreases progres-

sively. Although there is no damping term involved in the summation of the waves, it is clearly seen from the resultant wave, that the amplitude decreases monotonically. This is called dephasing.

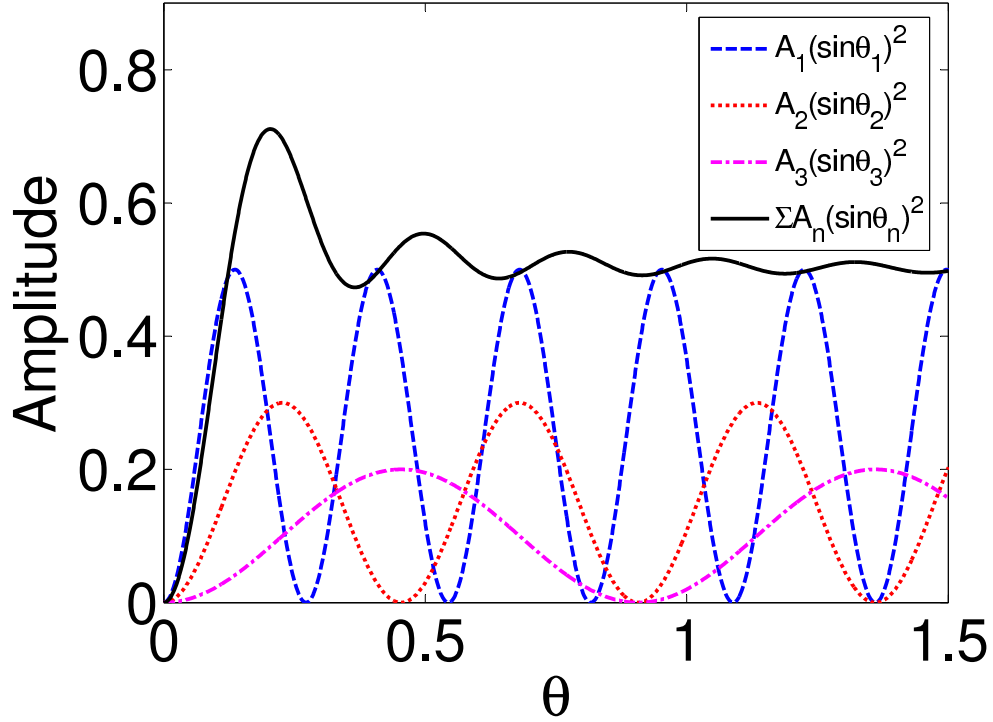


Figure 3.4: Three square of sinusoid waves (represented by the non-continuous lines) don't show any damping. But when lots of such waves are added up, it results in a summed wave (represented by the continuous line) which damps out. Although there is no damping term involved in the summation of the waves, it is clearly seen from the resultant wave, that the amplitude decreases monotonically. This is called dephasing.

This phenomenon of dephasing would mean that when studying oscillations of the whole plasma, the waves would seem to damp out sooner in time than they would if the plasma were to have a constant density. This implies that if we do the spectral analysis on the whole plasma cloud to get an average temperature of the ions, the oscillations in that temperature will be significantly dephased and hard to study. On the other hand, if we analyze very small regions of the plasma cloud, the variation

of density in that region would be significantly less, which would reduce the effect of dephasing. For this reason, we analyze the plasma cloud's temperature in cylindrical annular regions, and then extract the average temperature in those annuli, which should show more prominent oscillations. In fact, by dividing the plasma cloud into lot of annular regions and extracting temperature from each of them, this gives us a powerful tool by which we can also study the temperature and density with respect to position. The next chapter has more details on this type of analysis technique, where details of plasma oscillations with time will also be shown.

3.4 Expansion of ions in UCNP

After DIH and plasma oscillations, this is one of the final process that influences the ion temperature. The process of expansion can be visualized better by keeping in mind that after photo-ionization, electrons take up most of the energy of the photons. Due to this excess energy, immediately after photo-ionization, some of the electrons escape the plasma. This creates a quasi-neutral plasma cloud, which is more or less neutral, but the slight charge-imbalance in favor of the ions, creates a potential well for the electrons. But eventually the electrons' pressure forces the plasma to radially expand [22, 20, 21, 23, 41, 18]. This type of expansion changes the plasma size too which has been optically imaged (see Fig. 3.5).

The way ultracold plasmas are created gives us a lot of control on the expansion characteristics. For example, the expansion of the plasma is very much dominated

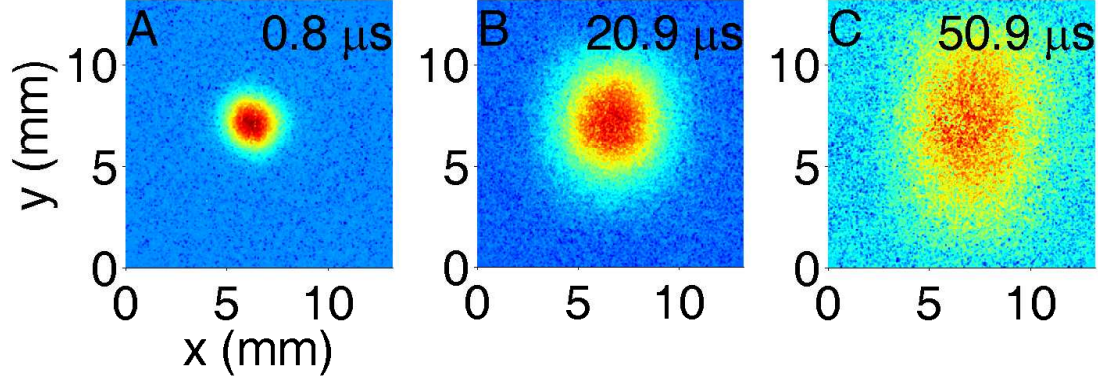


Figure 3.5: Expanding plasma. These are the optical images showing the expansion of the plasma. The y-axis of the images show the real size of the expansion. Plasma size along the x-axis is modified due to Gaussian distribution of intensity of the laser along x. The red color (center) denotes a high density plasma, whereas, blue denotes (along the periphery) denotes low density. Note that how the size of the plasma increases with time. The data shown here has initial electron temperature of $2E_e/3k_B = 105 \pm 3$ K, initial peak ion-density of $n_0 = 18 \pm 0.2 \times 10^{15} \text{ m}^{-3}$, and initial size, $\sigma_0 = 0.84 \pm 0.1$ mm.

by electron temperature. The beauty of ultracold plasmas is that the temperature of the electrons can be very finely controlled by changing the photo-ionizing laser's frequency. Also, the initial size of the plasma determines the rate of expansion, and it can be changed by letting the neutral MOT undergo free expansion before photo-ionization. Choosing a bigger initial size, the rate of expansion can be made slower so that more time is available to diagnose the expansion.

Another usefulness of expanding UCNP is that it can be used as an experimental tool [27] to study exact solutions of the Vlasov kinetic equations, which give the solutions for the ion and electron distribution functions [26]. Vlasov equations describe the time variation of distribution functions in the absence of dissipative forces, like electron-ion thermalization, collision and three body recombination. Vlasov equations are very important for the kinetic theory of plasma. Solutions to the Vlasov equations

are also very important to study expansion of plasma into a vacuum, a problem which has received tremendous focus in the past few decades, both theoretically [28, 29, 30] and experimentally [31, 32] and both [33].

It is shown in [42], that if we assume a collisionless system and that the Coulomb coupling parameter of both the electrons and ions be less than one, then the Vlasov equation [43] describing the electron or ion distribution function, $f_\alpha(\mathbf{r}, \mathbf{v})$, is given as

$$\frac{\partial f_\alpha}{\partial t} + \mathbf{v}_\alpha \frac{\partial f_\alpha}{\partial \mathbf{r}_\alpha} - \frac{q_\alpha}{m_\alpha} \frac{\partial f_\alpha}{\partial \mathbf{v}_\alpha} \frac{\partial \phi_\alpha(\mathbf{r}_\alpha)}{\partial \mathbf{r}_\alpha} = 0. \quad (3.6)$$

Here, $\alpha = e, i$ stands for electrons and ions respectively. m_α denotes the mass and q_α denotes the charge of the respective species. Also, in the above equation, $\phi_\alpha(\mathbf{r}_\alpha)$ is the mean field potential of the system. In general, Eqn.3.6 does not have a closed form analytical solution, but by making further assumptions of quasi-neutrality, spherical symmetry, self-similar Gaussian expansion and that the velocity distribution is Maxwell-Boltzmann, we can get a closed analytical form solution. These assumptions are valid in some cases of UCNP. For example, the UCNP is mostly quasi-neutral since the electron and ion density is almost the same locally. We can also create a spherically symmetric plasma by making the atomic cloud (before photoionization) symmetric by balancing the power of the MOT beams. Also, if the expansion velocity of the ions is proportional to their distances from the center of the plasma ($\mathbf{u}(\mathbf{r}, t) = \gamma(t)\mathbf{r}$), and there are no significant collisional or radiative processes, then the plasma should follow a self-similar Gaussian expansion. We will verify this assumption for our case

in this thesis. The last assumption of a Maxwell-Boltzmann distribution also makes the Vlasov equations even valid in the case of collisional systems.

Making use of the quasi-neutrality assumption, it can be shown that the mean field potential, ϕ , is given by [42]

$$e \frac{\partial \phi_\alpha}{\partial \mathbf{r}} = k_B T_e \frac{1}{\rho_e} \frac{\partial \rho_e}{\partial \mathbf{r}} \approx k_B T_i \frac{1}{\rho_i} \frac{\partial \rho_i}{\partial \mathbf{r}}, \quad (3.7)$$

where, $\rho_{e,i}$ is the density of electrons and ions. Also, the Gaussian distribution of density and Maxwell-Boltzmann distribution of velocities means that the distribution function will be of the form

$$f_\alpha(\mathbf{r}, \mathbf{v}) \propto \exp \left[-\frac{r^2}{2\sigma^2} - \frac{m_\alpha(\mathbf{v} - \gamma(t)\mathbf{r})^2}{2k_B T_\alpha} \right], \quad (3.8)$$

where, the expansion velocity is given as

$$\mathbf{u}(\mathbf{r}, t) = \gamma(t)\mathbf{r} \quad (3.9)$$

Putting the above two equations in Eqn.3.6, and neglecting electron-ion collisions, the following sets of differential equations are obtained [42] which describe the

evolution of the size, expansion velocity, and temperature of the plasma as

$$\frac{\partial \sigma^2}{\partial t} = 2\gamma\sigma^2 \quad (3.10a)$$

$$\frac{\partial \gamma}{\partial t} = \frac{k_B T_e + k_B T_i}{m_i \sigma^2} - \gamma^2 \quad (3.10b)$$

$$\frac{\partial k_B T_i}{\partial t} = -2\gamma k_B T_i \quad (3.10c)$$

$$\frac{\partial k_B T_e}{\partial t} = -2\gamma k_B T_e. \quad (3.10d)$$

Multiplying Eqn. 3.10c by σ^2 and Eqn. 3.10a by $k_B T_i$, and adding the resulting equations, it can be seen that $\partial(\sigma^2 k_B T_i)/\partial t = 0$, which implies, $\sigma^2 T_i = \text{constant}$, which is expected during adiabatic cooling of a UCNP. Similarly, it can also be shown that $\sigma^2 T_e = \text{constant}$ too. The above two conditions give us two constants of motion. There is also another constant of motion too, the total energy of the system, which can be written as $E_{tot} = E_{thermal} + E_{exp}$. Here, $E_{thermal}$ is the total thermal energy and owing to three degrees of freedom equals to $(3/2)N_i k_B (T_e + T_i)$. Since electronic mass is very small compared to that of the ions, we can neglect the contribution of the electronic expansion energy to the total expansion energy. Thus the energy of the system due to expansion, E_{exp} , can be approximated to that of the ions alone, which can be calculated using the distribution function (Eqn. 3.8) and the expansion

velocity expression (Eqn. 3.9) as follows

$$\begin{aligned}
E_{exp} &= \frac{1}{2} N_i m_i \frac{\int d^3r d^3v \mathbf{u}^2(\mathbf{r}, t) f_i(\mathbf{r}, \mathbf{v})}{\int d^3r d^3v f_i(\mathbf{r}, \mathbf{v})} \\
&= \frac{1}{2} N_i m_i \frac{\int_0^\infty (r^2 dr) \gamma^2 r^2 \exp\left(-\frac{r^2}{2\sigma^2}\right)}{\int_0^\infty (r^2 dr) \exp\left(-\frac{r^2}{2\sigma^2}\right)} \\
&= \frac{3}{2} N_i m_i \gamma^2 \sigma^2.
\end{aligned} \tag{3.11}$$

Using the three constants of motions, Eqns. 3.10 can be solved [42] to yield the following solutions

$$\sigma^2(t) = \sigma^2(0) (1 + t^2/\tau_{exp}^2) \tag{3.12a}$$

$$\gamma(t) = \frac{t/\tau_{exp}^2}{1 + t^2/\tau_{exp}^2} \tag{3.12b}$$

$$T_\alpha(t) = \frac{T_\alpha(0)}{1 + t^2/\tau_{exp}^2}, \tag{3.12c}$$

where, the expansion rate is determined by the characteristic expansion time

$$\tau_{exp} = \sqrt{m_i \sigma(0)^2 / k_B [T_e(0) + T_i(0)]}. \tag{3.13}$$

The value of τ_{exp} is approximately equal to 14 μ s for our Strontium plasma for a typical initial size $\sigma(0) = 1$ mm, initial electron temperature, $T_e(0) = 50$ K and initial ion temperature, $T_i(0) = 1$ K. The expression for $\sigma(t)$ above (Eqn. 3.12a) gives the change of the plasma size during expansion. It also indicates that if the expansion time (τ_{exp}) is smaller, then expansion will be more rapid. Equation 3.12b shows that

the expansion velocity of ions ($\mathbf{u}(\mathbf{r}, t) = \gamma(t)\mathbf{r}$) is not only proportional to the position from the center, it is also proportional to time, if $t < \tau_{exp}$. Although, if time t is significantly large than τ_{exp} , then $\gamma(t) \approx 1/t$, signifying that the expansion velocity starts slowing down at later times. The last equation (3.12c) in the set of equations shows adiabatic cooling of the thermal temperature of the ions and electrons. This thesis's aim is to prove equations 3.12 (3.12c for the case of ions only) experimentally (see chapter 7), which will characterize the plasma expansion. For a more direct proof of 3.12c for the case of electrons, the reader can refer to [24].

If the root-mean-squared velocity of ions in a particular direction (say, x) is represented by $v_{i,rms}$, then, it is given as [27]

$$\begin{aligned} v_{i,rms} &= \sqrt{\frac{\int d^3r d^3v (\mathbf{v} \cdot \hat{x})^2 f_\alpha(\mathbf{r}, \mathbf{v})}{\int d^3r d^3v f_\alpha(\mathbf{r}, \mathbf{v})}} \\ &= \sqrt{\frac{k_B}{m_i} \left\{ \frac{t^2}{\tau_{exp}^2} [T_e(t) + T_i(t)] + T_i(t) \right\}}, \end{aligned} \quad (3.14)$$

where, v is the total ion velocity including random thermal motion and expansion. One of our goal in this thesis is also to verify Eqn.3.14 experimentally (see chapter 7). This, along with the verification of equations 3.12 will prove the validity of the exact solution of Vlasov equations in the case of UCNF.

Chapter 4

Diagnostics of UCNP - Absorption Imaging and spectroscopy

4.1 Introduction

In order to know characteristic behavior of plasma, we need to know some of its key physical properties, like, temperature, density, and size of the plasma cloud. In this chapter we will see how we can extract the size, density and the temperature variation with position and time using absorption imaging spectroscopy and annular analysis. The goals are to confirm self-similar expansion and to see how the thermal temperature varies with time and whether we are able to see adiabatic cooling of ions [35].

4.2 Importance of optical imaging

Numerous techniques have been invented to obtain the above mentioned physical properties from the plasma. For example, the Langmuir probe, in which electrodes with electric potentials are used to generate electric field and obtain response of the

plasma. Determining the response, the plasma parameters (temperature, charge, density etc.) can be extracted. Magnetic probes have also been used to find out the rate of change of magnetic field which gives the electric field and current density of the plasma [44]. The Charged particle detection setup can also be used to probe the time of flight measurement of the charged particles and get the electric field information of the plasma.

Although all of these probes are effective in obtaining key parameters of the plasma, nevertheless, they may not be the best solution for the experiments we envision to do. For example, our plasma density can be very low making it harder to use electric field probes. Our main goal is to measure the temperature and size of the plasma and to see its variation with time and space with sufficient resolution. Lot of phenomena like disorder induced heating happen in the first micro-second of the plasma formation, and thus, our probe has to be able to measure with about hundred nano-second resolution. Spatially too, the size of the plasma itself is about a mm, thus needing spatial resolution in the μm scale. Probing the plasma with a laser beam [20, 18] (absorption or laser induced fluorescence (LIF) imaging) provides a way to achieve these requirements as we can image the plasma with about 10 ns time and about 100 μm spatial resolution. The time and spatial resolution is achieved by recording the image on a gated charge-coupled device (CCD) camera. A schematic of the imaging and laser system is shown in Fig. 4.1. The imaging laser (422 nm) is produced by frequency doubling 844 nm light, which is obtained from an extended

cavity diode laser. The flipper mirror in the figure allows us to use the same beam for absorption as well as fluorescence (from here on, fluorescence will refer to LIF only). By using both these techniques, we can do spatially resolved Doppler spectroscopy on our plasma from which we know the temperature dependence on space and time. Also, by taking direct images of the plasma, we can know its size variation with time too. Although, absorption and fluorescence are quite similar physical processes (kind of like two sides of the same coin), fluorescence gives us the freedom to image the plasma in a different direction than the imaging laser. We will see in the next chapter that due to this, we are able to separate the expansion velocity from the thermal velocity.

4.3 Brief introduction of absorption and fluorescence

As mentioned in the previous section, absorption and fluorescence (LIF) are quite similar processes. This is because, in absorption when light is incident on matter (atoms, ions etc.), electrons in the matter absorb the photons and go to excited levels. Thus, the intensity of light drops after passing through the matter, and we can see a shadow of the matter. Similarly, in LIF the matter first absorbs the light, and the electrons go to excited states, and then they re-radiate the light which we observe as fluorescence. In other words, if we observe the matter along a direction other than the laser's, we will see fluorescence light. Analyzing the shadow (in the case of absorption), or the light (in the case of fluorescence) can give us information

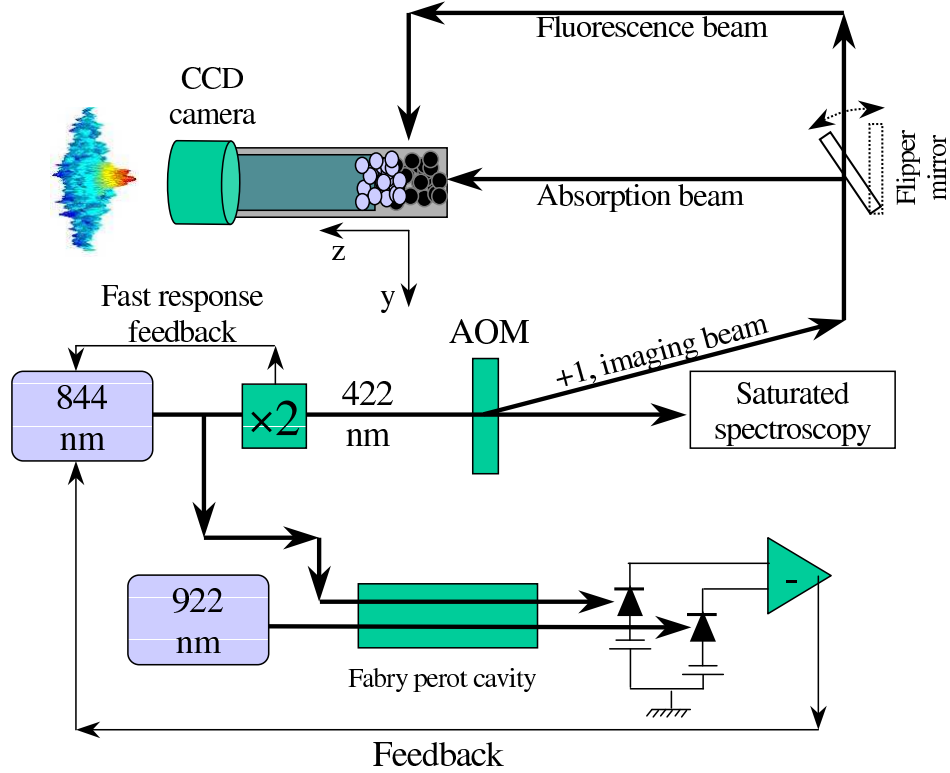


Figure 4.1: Set-up of 422 nm imaging system. The imaging laser (422 nm) is produced [45] by frequency doubling 844 nm light, which is obtained from an extended cavity diode laser. The timing is controlled by using an AOM and spatial resolution is achieved by recording the image on a charge-coupled device (CCD) camera. The flipper mirror in the figure allows us to use the same beam as absorption or fluorescence imaging beam. The 844 nm laser is locked to its frequency in reference to 922 nm (Ti:Saph) by using a Fabry Perot cavity.

about the size and temperature of the matter. This is the main principle of absorption or fluorescence imaging.

4.3.1 Electronic levels of Sr ion

Since the electronic levels dictate how much light the matter will absorb or fluoresce, before we proceed into details, it is good to know a little about the Sr ions electronic structure. The two main levels that we use for imaging Sr ions are $^2S_{1/2}$ (ground state), and $^2P_{1/2}$ (excited state) (see Fig. 4.2). The energy difference between

these states is 421.7 nm, a wavelength which is in the visible range and easily produced by standard laser sources and frequency doubling techniques [46]. For precision, the time of the exposure is controlled by an Acousto-optic modulator (AOM), and the intensity of light is controlled by an RF attenuator. In Sr ion energy levels, there is another level, $^2D_{3/2}$ (see Fig. 4.2), which has a branching ratio of 7%, to which the ions can decay. But the intensity and exposure time of absorption beam is chosen to be low enough that the ions scatter less than one photon in the whole exposure. This ensures that we are not pumping ions into the D state. However, in different experiments on laser cooling of Sr ions, the intensity of light is close to saturation, and optical pumping to the $^2D_{3/2}$ state is a big issue. The reader can see Clayton Simien’s PhD thesis [45] for more information on this.

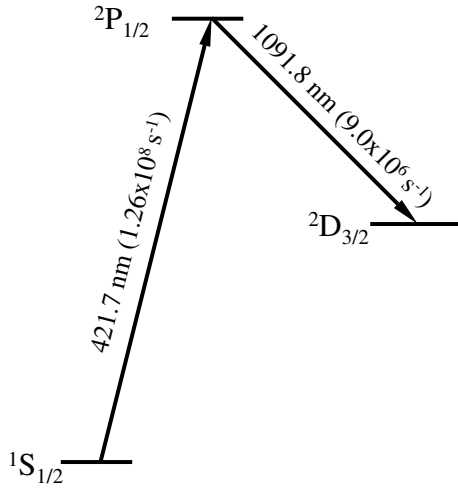


Figure 4.2: Sr ion energy level diagram. $^2S_{1/2} \rightarrow ^2P_{1/2}$ is used to do imaging of Sr ions. The branching ratio of $^2D_{3/2}$ is about 7%, but the intensity of absorption light that is used is low enough that the ions scatter less than one photon in the whole exposure.

We have already seen that both absorption and fluorescence (LIF) rely on how much light matter (ions in our case) can absorb. Thus, both the processes are intrin-

sically dependent on the absorption cross section (power of light absorbed per unit incident intensity of light) of the matter. Theoretically, the absorption cross section is given by

$$\alpha(\nu, T_i, \nu^{\hat{k}}) = \frac{3^* \lambda^2}{2\pi} \frac{\gamma_0}{\gamma_{eff}} \int_{-\infty}^{\infty} ds \frac{1}{1 + \left[\frac{2(\nu-s)}{\gamma_{eff}/2\pi} \right]^2} \frac{1}{\sqrt{2\pi} \sigma_D [T_i(r)]} \exp \left\{ -\frac{[s - \nu_0 - \nu^{\hat{k}}]^2}{2\sigma_D^2 [T_i(r)]} \right\}, \quad (4.1)$$

where, α is primarily a function of ν , the frequency of incident light, T_i , the thermal temperature of the ions and $\nu^{\hat{k}} = v^{\hat{k}}/\lambda$, the Doppler shift of the laser frequency due to any directed velocity ($v^{\hat{k}}$) (see section 3.4) of the ions along the laser wave vector, \hat{k} . It should be noted that whether the system has reached local thermal equilibrium or not, we characterize the kinetic energy arising from random motion by a temperature T_i that may vary with position.

Also in the above equation, ν_0 is the resonance frequency of transition and $\lambda = 422$ nm, is the transition wavelength. γ_{eff} is the full-width half-maximum (FWHM) of the observed transition and if the dominant broadening is because of laser linewidth and natural linewidth, then, $\gamma_{eff} = \gamma_0 + \gamma_{laser}$, where, $\gamma_0 = 2\pi \times 20.21 \times 10^6 \text{ s}^{-1}$ is the natural linewidth and $\gamma_{laser} = 2\pi \times (5 \pm 2) \times 10^6 \text{ s}^{-1}$ is the laser linewidth. The symbol 3^* in the equation is a factor which depends on the laser and ion polarization [47]. In our case, due to random alignment of ions and linear polarization of the laser, the symbol 3^* equals 1. It should also be mentioned that the above expression of α is a Voigt profile which is a convolution of Lorentzian and Doppler broadenings. The

Lorentzian linewidth is γ_{eff} and the term $\sigma_D(T_i) = (1/\lambda)\sqrt{(k_B T_i/m_i)}$ would be the Doppler broadening if the ions velocities consisted of purely thermal energy.

4.4 Generating the spectrum for absorption

The absorption cross section (α) can be related to experimental quantities by using Beer's law which is defined as

$$\ln \left[\frac{I_{bg}}{I_{plasma}} \right] = \int_{-\infty}^{\infty} n_i(r) \alpha \left(\nu, T_i, \nu^{\hat{k}} \right) dz, \quad (4.2)$$

where I_{plasma} and I_{bg} are the intensity of the laser when the plasma is present and when it is not, and $n_i(r)$ is the local plasma density. The integral is along z , because as shown in Figs. 4.1 and 4.3, the absorption laser is along the z direction. The quantity $\ln(I_{bg}/I_{plasma})$ is also called the optical depth, represented as OD , which is thus given as

$$OD(x, y, \nu, T_i, \nu^{\hat{k}}) = \int_{-\infty}^{\infty} n_i(r) \alpha \left(\nu, T_i, \nu^{\hat{k}} \right) dz. \quad (4.3)$$

To get the frequency dependence of ion absorption, we integrate the OD over x and y to get the spectrum as

$$S(\nu) = \int OD(x, y) dx dy \quad (4.4)$$

$$= \int d^3r n_i(r) \alpha(\nu, T_i, \nu^k) \quad (4.5)$$

$$= \frac{\lambda^2}{2\pi} \frac{\gamma_0}{\gamma_{eff}} \int_{-\infty}^{\infty} ds \frac{1}{1 + \left[\frac{2(\nu-s)}{\gamma_{eff}/2\pi} \right]^2} \int d^3r n_i(r) \frac{1}{\sqrt{2\pi}\sigma_D[T_i(r)]} \times \exp \left\{ -\frac{[s - \nu_0 - \nu^k]^2}{2\sigma_D^2[T_i(r)]} \right\} \quad (4.6)$$

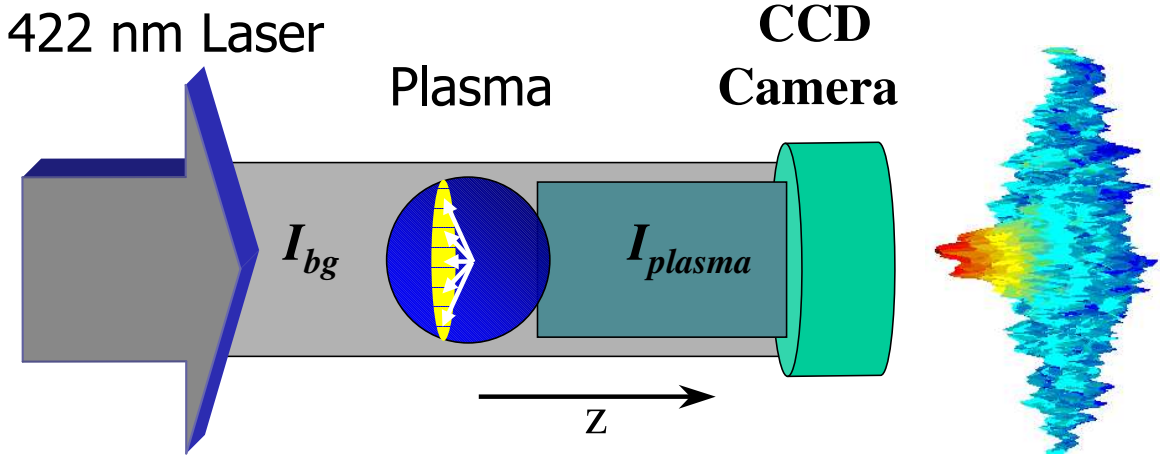


Figure 4.3: Absorption imaging of Sr ion is done using the $^2S_{1/2} \rightarrow ^2P_{1/2}$ transition. The shadow is recorded on a charge coupled device (CCD) camera and the optical depth of the image is calculated. Here, I_{plasma} and I_{bg} are the intensity of the laser when the plasma is present and when it is not. Depending on the detuning of the laser, a particular velocity class of ions (whose z projection of velocity equals λ times the detuning) are resonant with the beam. A false-colored OD (optical depth) is also shown on the right.

4.5 Spectrum with expansion and annular analysis

The spectrum given by Eqn. 4.6 is a very general one and will be valid for any thermal temperature T_i and shift in the resonance frequency $\nu^{\hat{k}}$. We can get more insight from the spectrum by dialing in some factual information about our system in Eqn. 4.6 so that we can extract the density and thermal temperature of our plasma and also get their spatial distribution. For example, as shown in Fig.4.3, since the laser is propagating along the z-axis, the z component of the expansion velocity will contribute to the Doppler shift on the resonance frequency. Thus,

$$\nu^{\hat{k}} = u_z/\lambda = \gamma(t)z/\lambda, \quad (4.7)$$

where, the expression of the expansion velocity has been used from Eqn 3.9.

Also, as pointed out earlier, both temperature and density depend on position, and therefore, to reduce averaging effects (like dephasing), it is needful to do the integration in Eqn. 4.6 over as small a region as possible. We cannot limit the z integration as it is our imaging axis. Thus, to lower the spatial averaging effects, we divide the plasma image into cylindrical annular regions with their axes passing through the center of the plasma and directed along the absorption laser beam (z direction). In Fig. 4.4, one such region is shown schematically. Theoretically, there can be as many regions as possible to get rid of the averaging effects, but practically, the number of regions is restricted by the resolution (inverse of number of pixels) of

the image. Thus, for the annular case, we rewrite the spectrum in a region as

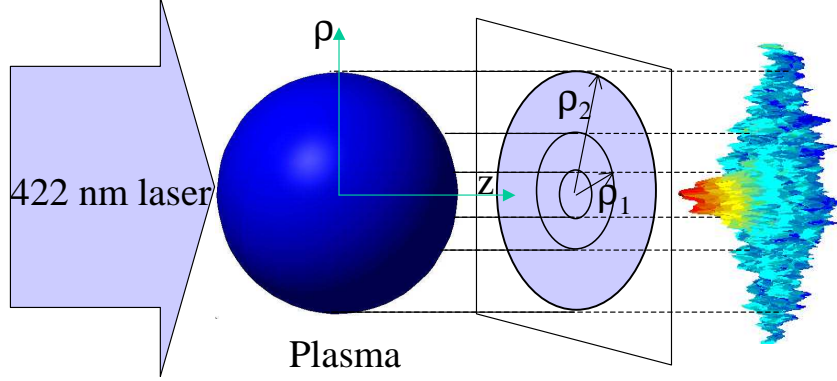


Figure 4.4: Spatially-resolved absorption imaging. The plasma-image is divided into cylindrical annular regions with its axis passing through the center of the plasma and directed along the absorption laser beam (z direction). Dividing the image in these annular regions reduces the averaging and dephasing effects in the analysis.

$$\begin{aligned}
 S_{reg}(\nu) &\equiv \int_{A_{reg}} OD(x, y) dx dy = \int_{\rho_1}^{\rho_2} 2\pi \rho d\rho \int_{-\infty}^{+\infty} dz n_i(r) \alpha(\nu, T_i, \nu^k) & (4.8) \\
 &= \frac{\lambda^2}{2\pi} \frac{\gamma_0}{\gamma_{eff}} \int_{-\infty}^{\infty} ds \frac{1}{1 + \left[\frac{2(\nu-s)}{\gamma_{eff}/2\pi} \right]^2} \times \int_{\rho_1}^{\rho_2} \int_{-\infty}^{+\infty} 2\pi \rho d\rho dz \frac{n_i(r)}{\sqrt{2\pi} \sigma_D [T_i(r)]} \times \\
 &\quad \exp \left\{ -\frac{[s - \nu_0 - \gamma(t)z/\lambda]^2}{2\sigma_D^2 [T_i(r)]} \right\}, & (4.9)
 \end{aligned}$$

where, $r = \sqrt{\rho^2 + z^2}$ is the relation between the spherical and polar coordinate variables and ρ_1 and ρ_2 define the boundaries of an annular region. We further assume that T_i is constant within those boundaries. This is true because we divide the whole plasma image into 50 annular regions, which gives us $\rho_1 - \rho_2 \approx 70\mu m$. To get a feel for numbers, if we consider the thermal temperature to have a distribution given by Eqn. 3.1, then T_i varies by only about 2% from ρ_1 to ρ_2 at $(\rho_1 + \rho_2)/2 = \sigma = 1$ mm, which is quite small and can be assumed to be a constant. Also, assuming a Gaussian

distribution of density, $n_i(r) = n_0 \exp(-r^2/2\sigma^2(t))$ (Eqn. 2.2), the expression for the spectrum above can be written as

$$S_{reg}(\nu) = \frac{\lambda^2}{2\pi} \frac{\gamma_0}{\gamma_{eff}} N_{reg} \int_{-\infty}^{\infty} ds \frac{1}{1 + \left[\frac{2(\nu-s)}{\gamma_{eff}/2\pi} \right]^2} \times \int_{-\infty}^{+\infty} dz \frac{\exp(-z^2/2\sigma^2(t))}{\sqrt{2\pi}\sigma(t)} \times \frac{\exp\left\{-\frac{[s-\nu_0-\gamma(t)z/\lambda]^2}{2\sigma_D^2(T_i)}\right\}}{\sqrt{2\pi}\sigma_D(T_i)} \quad (4.10)$$

$$= \frac{\lambda^2}{2\pi} \frac{\gamma_0}{\gamma_{eff}} N_{reg} \int_{-\infty}^{\infty} ds \frac{1}{1 + \left[\frac{2(\nu-s)}{\gamma_{eff}/2\pi} \right]^2} \frac{\exp\left(-\frac{(s-\nu_0)^2}{2[\sigma_\theta^2 + \sigma_D^2(T_i)]}\right)}{\sqrt{2\pi}\sqrt{\sigma_\theta^2 + \sigma_D^2(T_i)}} \quad (4.11)$$

$$= \frac{\lambda^2}{2\pi} \frac{\gamma_0}{\gamma_{eff}} N_{reg} \int_{-\infty}^{\infty} ds \frac{1}{1 + \left[\frac{2(\nu-s)}{\gamma_{eff}/2\pi} \right]^2} \frac{\exp\left(-\frac{(s-\nu_0)^2}{2\sigma_{D,eff}^2}\right)}{\sqrt{2\pi}\sigma_{D,eff}}, \quad (4.12)$$

where, N_{reg} is the number of ions in an annular region and $\sigma_\theta = \sigma(t)\gamma(t)/\lambda$. Looking at the final form of the expression of spectrum in Eqn.4.11, it can be seen that the spectrum is Doppler broadened because of an effective Doppler width, $\sigma_{D,eff} = \sqrt{\sigma_\theta^2 + \sigma_D^2(T_i)}$, which has contribution from both the expansion energy as well as the thermal energy. The temperature corresponding to this effective width in a given

time, t , will be given by,

$$\begin{aligned}
T_{eff}(t) &= \frac{\lambda^2 m_i}{k_B} \sigma_{D,eff}^2 \\
&= \frac{\lambda^2 m_i}{k_B} [\sigma_\theta^2 + \sigma_D^2(T_i(t))] \\
&= \frac{\lambda^2 m_i}{k_B} \left[\frac{\sigma^2(t) \gamma^2(t)}{\lambda^2} + \frac{k_B}{\lambda^2 m_i} T_i(t) \right] \\
&= \frac{m_i \sigma^2(t) \gamma^2(t)}{k_B} + T_i(t) \\
&= \frac{m_i}{k_B} \sigma^2(0) \left(1 + \frac{t^2}{\tau_{exp}^2} \right) \left(\frac{t/\tau_{exp}^2}{1 + t^2/\tau_{exp}^2} \right)^2 + T_i(t) \\
&= \frac{m_i}{k_B} \left(\frac{t^2}{\tau_{exp}^2} \right) \frac{1}{\tau_{exp}^2} \left(\frac{\sigma^2(0)}{1 + t^2/\tau_{exp}^2} \right) + T_i(t) \\
&= \frac{m_i}{k_B} \left(\frac{t^2}{\tau_{exp}^2} \right) \frac{k_B (T_e(0) + T_i(0))}{m_i \sigma^2(0)} \left(\frac{\sigma^2(0)}{1 + t^2/\tau_{exp}^2} \right) + T_i(t) \\
&= \left(\frac{t^2}{\tau_{exp}^2} \right) \frac{(T_e(0) + T_i(0))}{1 + t^2/\tau_{exp}^2} + T_i(t) \\
&= \left(\frac{t^2}{\tau_{exp}^2} \right) [T_e(t) + T_i(t)] + T_i(t), \tag{4.13}
\end{aligned}$$

where, we have used definitions of $\sigma(t)$, $\gamma(t)$, $T_e(t)$, and $T_i(t)$ from Eqns.3.12 and that of τ_{exp} from Eqn. 3.13. Also, from the above equation (Eqn. 4.13), we can derive an expression of

$$\sqrt{\frac{k_B T_{eff}(t)}{m_i}} = \sqrt{\frac{k_B}{m_i} \left\{ \frac{t^2}{\tau_{exp}^2} [T_e(t) + T_i(t)] + T_i(t) \right\}}, \tag{4.14}$$

which is exactly the same as the rms velocity of the ions as obtained from the distribution function of ions and electrons in Eqn. 3.14. Thus, T_{eff} measures the total rms velocity of ions.

4.5.1 Obtaining the spectrum and T_{eff} experimentally

To get T_{eff} and number of ions in a region, N_{reg} (from which we calculate the density) experimentally, we first find out the spectrum experimentally and then fit it to the Voigt given by Eqn.4.12. To get the spectrum, we image the plasma by varying the frequency of the imaging laser near the ion resonance. For a fixed frequency of the imaging laser, the OD is first integrated in each region, shown by the solid line in Fig. 4.5. Performing the same analysis for all the image beam detunings yields the three-dimensional OD distribution shown in the figure. Now, from this distribution, if we hold ρ constant, we will get the variation which is our usual spectrum given by Eqn. 4.12. In the figure, the dashed curve represents the typical spectrum at $\rho = 2.15$ mm.

Once we get the effective temperature, T_{eff} , we can calculate the ion thermal temperature, T_i , using Eqn.4.13. I would like to add a note here that in order to calculate T_i from Eqn.4.13, we also need to know the values of T_{e0} and σ_0 . This is done by fitting the rms velocity of ions versus time data to Eqn.4.14 assuming a constant $T_i(0)$ throughout the cloud which is given by Eqn.3.1. (For further reading on this, the reader may see [24] for details). The following chapter discusses the results of obtaining T_i and N_{reg} and seeing its variation with ρ through which we can find out the spatial distribution of the density and temperature of the plasma.

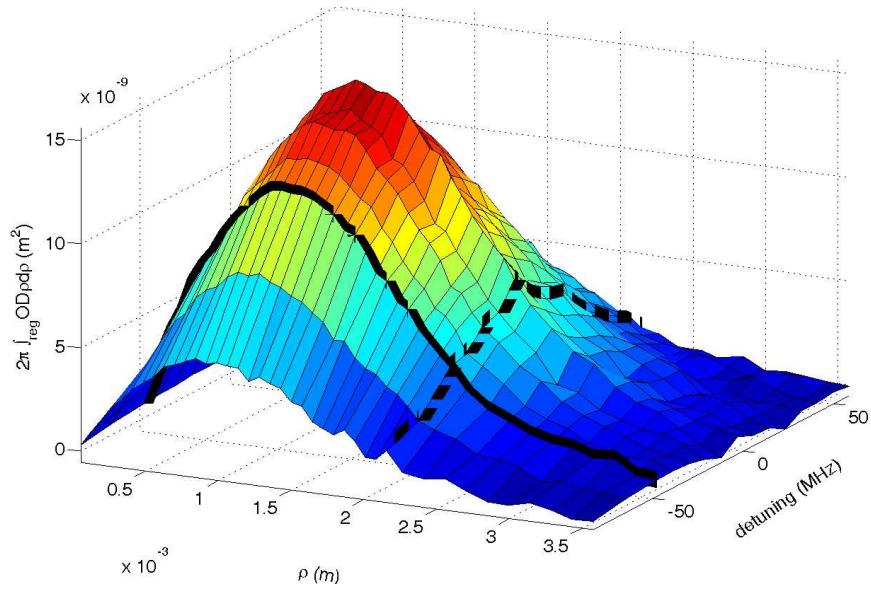


Figure 4.5: Variation of OD integral with respect to ρ and image laser detuning. The average perpendicular distance of a region from the axis is ρ . Every mesh intersection point represents a measurement. The solid line shows the integrated OD values from a single image with $\delta = -47$ MHz. The dashed line shows a spectrum for $\rho = 2.15$ mm constructed from many images.

Chapter 5

Results - Annular analysis of absorption data

5.1 Spectrum of annular regions

From the images, we first obtain the spectrum as described in Sec. 4.5.1. Typical spectra for 5 regions out of the 50 regions is shown in Fig. 5.1, where, the data has initial electron temperature, $2E_e/3k_B = 60 \pm 3$ K, initial peak ion-density of $n_0 = 2.42 \pm 0.2 \times 10^{15} \text{ m}^{-3}$, and initial size, $\sigma_0 = 1.0 \pm 0.1$ mm. Fitting the spectra to a Voigt profile given by Eqn. 4.10, gives us all the information about the number of ions, N_{reg} , and their effective temperature, T_{eff} , in a region. The solid lines in the spectra figure are such Voigt fits. One thing that is immediately evident from the figure is that the amplitude of the spectrum (which is also proportional to N_{reg}) increases from $\rho = 0$ mm to $\rho = 1.1$ mm, and then decreases to $\rho = 2.1$ mm. This is because of the fact that the annular regions are divided into regions of equal thickness, $\delta\rho$. And given the fact that the density of ions follows a Gaussian distribution,

$n(\rho, z) = n_0 \exp(-(\rho^2 + z^2)/2\sigma^2)$ (Eqn. 2.2), the number in a region will be given by,

$$N_{reg}(\rho) = \int_{\rho-\delta\rho/2}^{\rho+\delta\rho/2} (2\pi\rho' d\rho') \int_{-\infty}^{\infty} dz n_0 \exp(-(\rho'^2 + z^2)/2\sigma^2) \quad (5.1)$$

$$= \sqrt{2\pi} \sigma n_0 (2\pi\rho\delta\rho) \exp(-\rho^2/2\sigma^2), \quad (5.2)$$

which has a local maximum with respect to ρ .

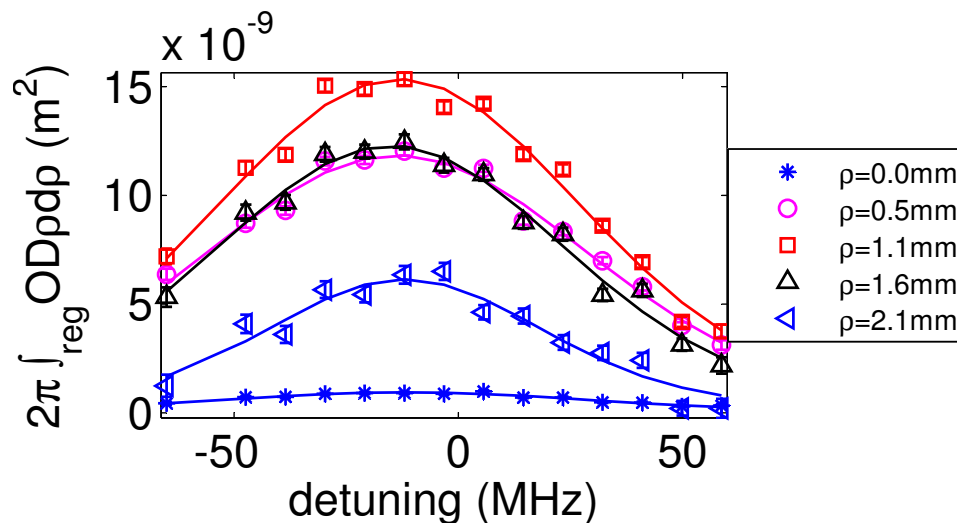


Figure 5.1: Spectra of annular regions. Typical spectra for 5 regions out of the 50 regions is shown, where, the data has initial electron temperature, $2E_e/3k_B = 60 \pm 3$ K, initial peak ion-density of $n_0 = 2.42 \pm 0.2 \times 10^{15} \text{ m}^{-3}$, and initial size, $\sigma_0 = 1.0 \pm 0.1$ mm. The marker points represent data taken at different detunings, and the errorbars of the points are almost hidden inside the markers. Fitting the spectra to a Voigt given by Eqn. 4.10, gives us all the information about the number of ions in a region, N_{reg} and the effective temperature, T_{eff} of that region. The continuous lines in the figure are those Voigt fits.

5.2 Number and density distribution of ions

To study the number of ions and density distribution of ions in more detail, we extract the parameter, N_{reg} , from each annular spectra and plot it with respect to

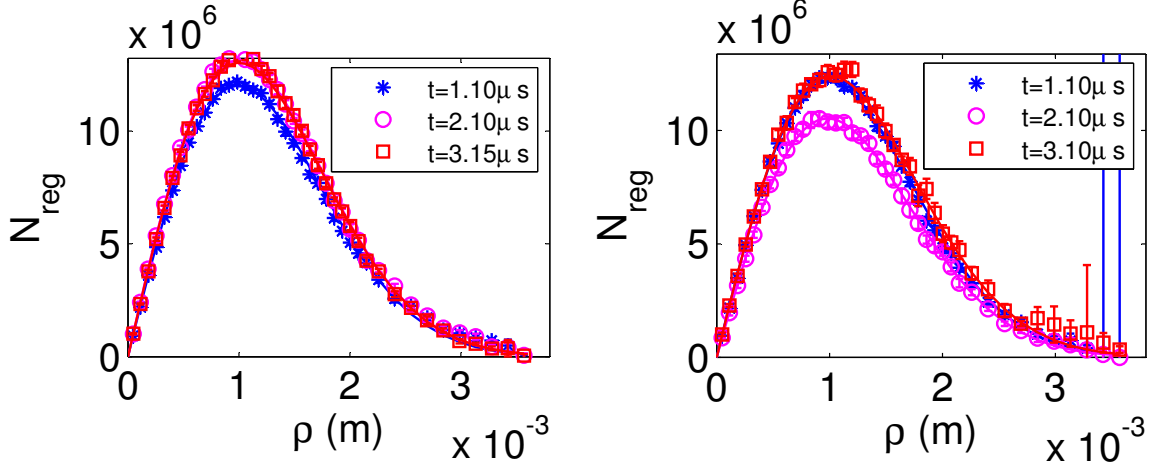
ρ . We also define another term named areal density (ρ_{areal}), which is defined as N_{reg} divided by the area of the annular region on the image. In mathematical terminology, it is written as

$$\rho_{areal}(\rho) = \frac{N_{reg}(\rho)}{2\pi\rho\delta\rho} \quad (5.3)$$

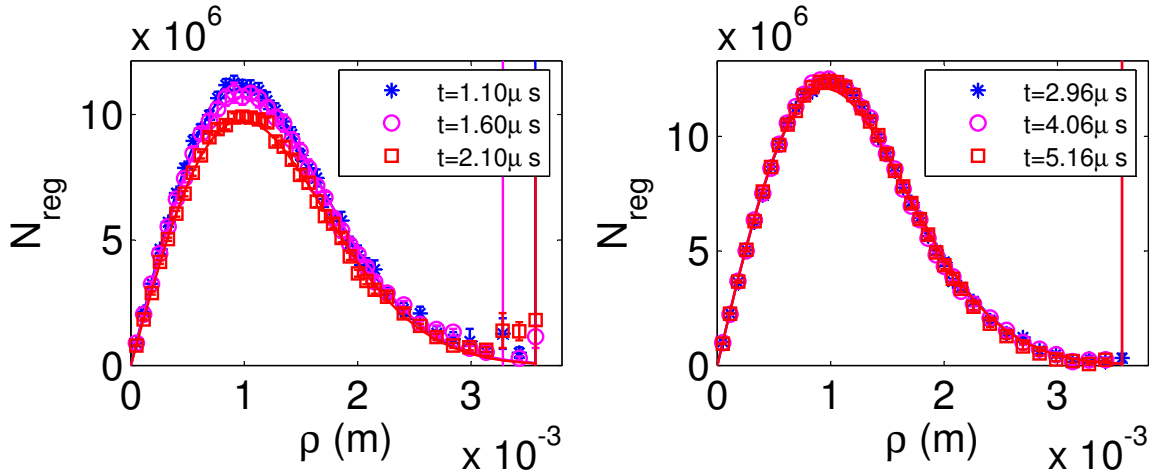
$$= \sqrt{2\pi} \sigma n_0 \exp(-\rho^2/2\sigma^2). \quad (5.4)$$

We repeat the process of obtaining $N_{reg}(\rho)$ and $\rho_{areal}(\rho)$ versus ρ for different times of ion evolution to study how the plasma cloud evolves with time. Some of the datasets for various initial conditions are shown in Fig. 5.2 and 5.3. From Fig. 5.2, the maximum of N_{reg} as described in the previous section is more directly evident.

The experimental data for the number and density are also fit to Eqn. 5.2 (for N_{reg} versus ρ , Fig. 5.2) and Eqn. 5.4 (for ρ_{areal} versus ρ , Fig. 5.3). The fact that the equations are very good fits of the data emphasizes the fact that the ion density distribution is indeed Gaussian and it remains Gaussian with time too. This means that the expansion of this plasma is a self-similar gaussian expansion, thus implying that Vlasov equation solutions will be valid in their exact form even in collisional systems.

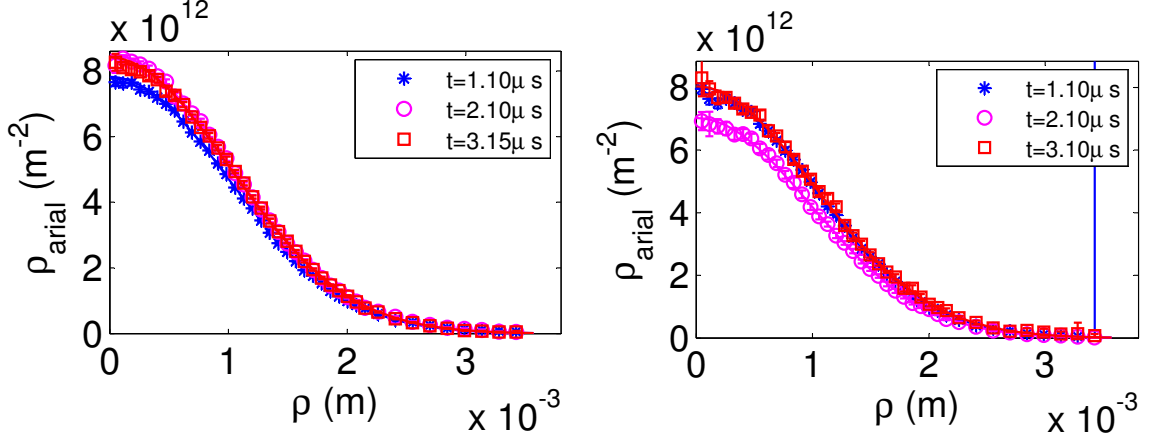


(a) $2E_e/3k_B = 25 \pm 3\text{K}$, $n_0 = 2.64 \pm 0.2 \times 10^{15} \text{ m}^{-3}$ (b) $2E_e/3k_B = 60 \pm 3\text{K}$, $n_0 = 2.42 \pm 0.2 \times 10^{15} \text{ m}^{-3}$

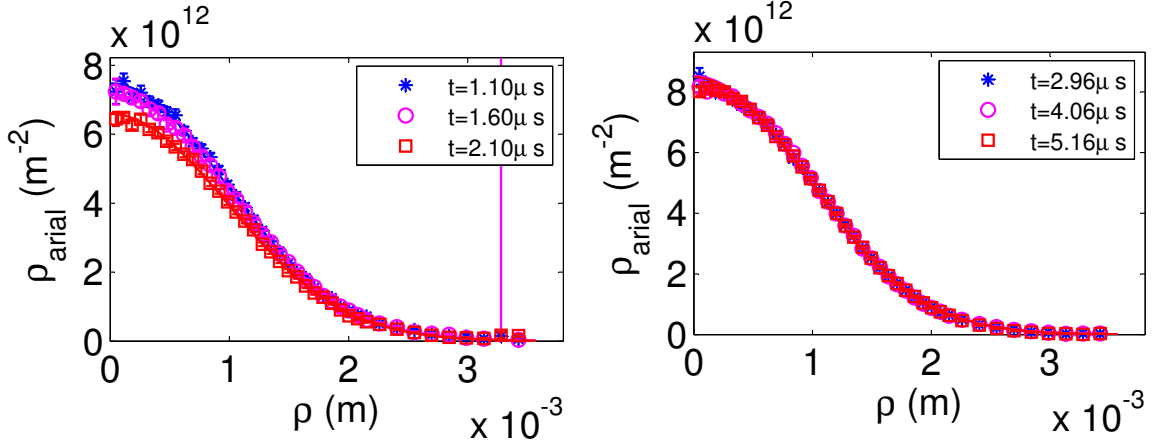


(c) $2E_e/3k_B = 116 \pm 3\text{K}$, $n_0 = 2.31 \pm 0.2 \times 10^{15} \text{ m}^{-3}$ (d) $2E_e/3k_B = 14 \pm 3\text{K}$, $n_0 = 2.20 \pm 0.2 \times 10^{15} \text{ m}^{-3}$

Figure 5.2: N_{reg} , the number of ions in a region with width $73 \mu\text{m}$ at ρ for various times. The different figures represent different initial conditions of the plasma. The markers are the data points obtained from the experiment and the continuous curves are fits to Eqn. 5.2. The fact that the equations are very good fits of the data emphasizes the fact that the ion density distribution is indeed Gaussian and it remains Gaussian with time too.



(a) $2E_e/3k_B = 25 \pm 3 \text{ K}$, $n_0 = 2.64 \pm 0.2 \times 10^{15} \text{ m}^{-3}$ (b) $2E_e/3k_B = 60 \pm 3 \text{ K}$, $n_0 = 2.42 \pm 0.2 \times 10^{15} \text{ m}^{-3}$



(c) $2E_e/3k_B = 116 \pm 3 \text{ K}$, $n_0 = 2.31 \pm 0.2 \times 10^{15} \text{ m}^{-3}$ (d) $2E_e/3k_B = 14 \pm 3 \text{ K}$, $n_0 = 2.20 \pm 0.2 \times 10^{15} \text{ m}^{-3}$

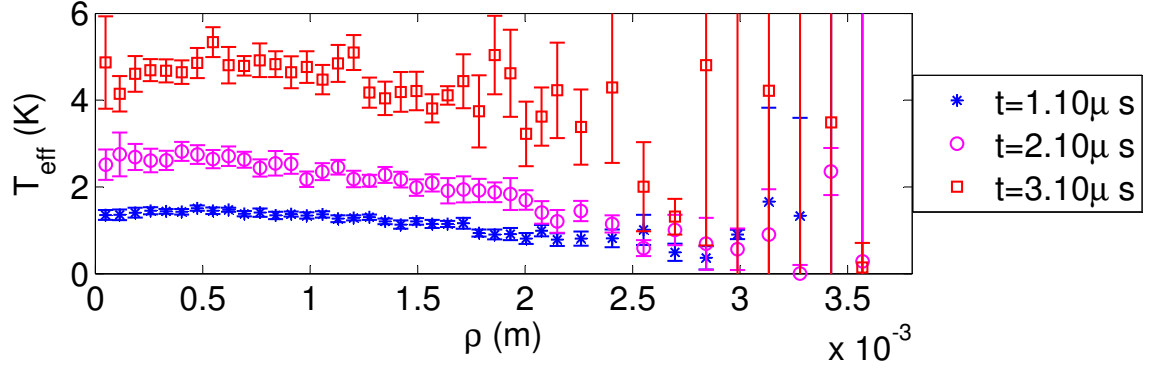
Figure 5.3: Areal density variation with ρ for various times. The different figures represent different initial conditions of the plasma. The markers are the data points obtained from the experiment and the continuous curves are fits to Eqn. 5.4. The fact that the equations are very good fits of the data emphasizes the fact that the ion density distribution is indeed Gaussian and it remains Gaussian with time too.

5.3 Spatial distribution of thermal temperature

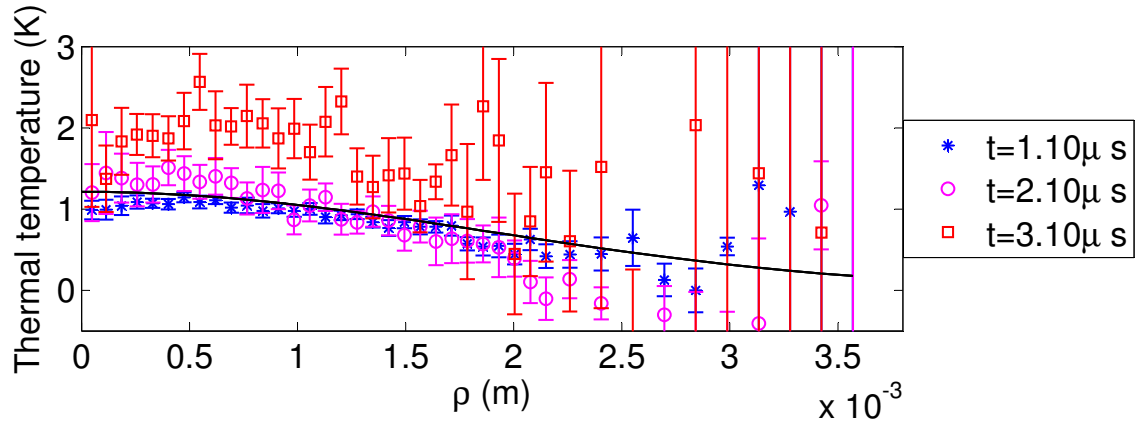
As mentioned in the previous chapter, we extract the effective temperature of ions, T_{eff} , from the annular spectra by fitting those to a Voigt profile. This gives us the average kinetic energy of the ions in that region, and studying it can give us insight into ion and electron dynamics inside the plasma. T_{eff} versus ρ plots for two datasets and also for various times are shown in figures 5.4(a) and 5.5(a). After extracting T_{eff} , we also calculate the ion thermal temperature, T_i using the Eqn. 4.13. Thermal temperature plots of the same datasets are shown in figures 5.4(b) and 5.5(b). The data sets in these figures are shown for early time when hopefully, expansion does not set in completely. This is because, as can be seen in the next couple of paragraphs, our model to extract thermal temperature does not seem to be fully valid during the full expansion.

As can be seen from the plots (figures 5.4(a) and 5.5(a)), that the effective temperature increases with increasing time, signifying the increase in electron velocity which increases the force on the ions. Another key feature that we see is that for a fixed time (more prominently for later times), T_{eff} falls off with ρ for $\rho > 2\sigma$ ($\sigma \approx 1$ mm for our datasets). We believe this happens because at later times, a lot of electrons have left the outer portion of the plasma, and thus there are less electrons to put pressure on the ions, thus decreasing their kinetic motion.

From the plots of T_i versus ρ (Figs. 5.4(b) and 5.5(b)), we note that the thermal temperature also decreases with increasing ρ . This happens because the density of

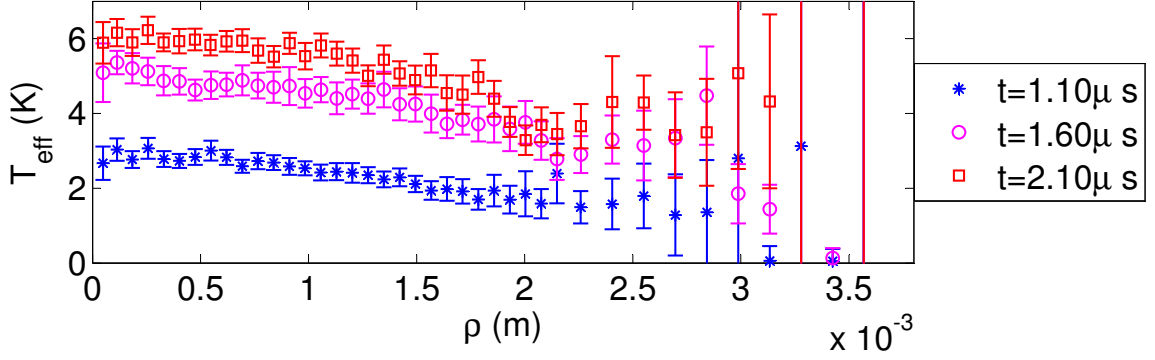


(a) Effective temperature.

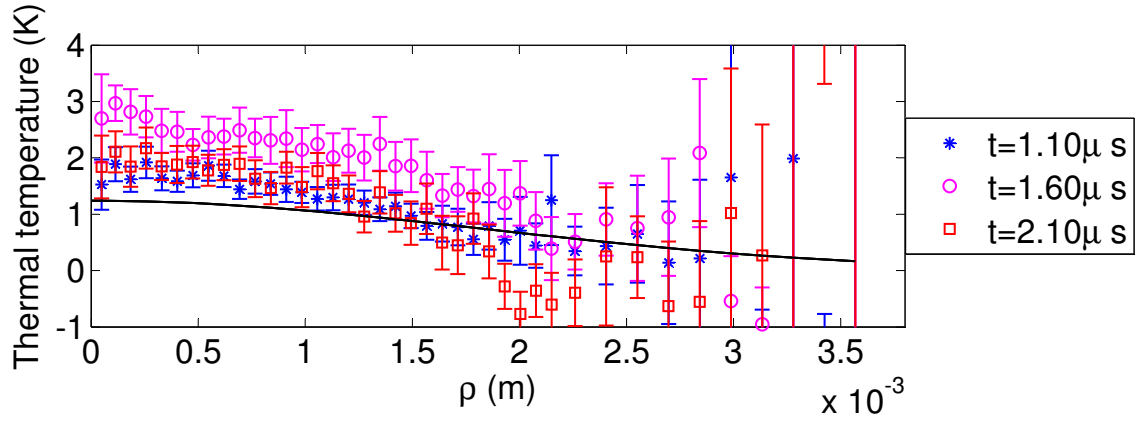


(b) Thermal temperature.

Figure 5.4: Plot of effective temperature, T_{eff} (a) and thermal temperature, T_i (b), versus ρ for various evolution times. T_{eff} is obtained by fitting the spectra of annular regions to a Voigt. The expansion energy is then subtracted off from the effective temperature, and the thermal temperature, T_i is calculated using Eqn.4.13. To compare the thermal temperature data to theory, a continuous line representing the thermalization temperature due to DIH as given by Eqn.3.1 is also shown. The above data-set had initial parameters as $2E_e/3k_B = 60 \pm 3$ K, $n_0 = 2.42 \pm 0.2 \times 10^{15} \text{ m}^{-3}$



(a) Effective temperature.



(b) Thermal temperature.

Figure 5.5: Plot of effective temperature, T_{eff} (a) and thermal temperature, T_i (b), versus ρ for various evolution times. T_{eff} is obtained by fitting the spectra of annular regions to a Voigt. The expansion energy is subtracted off from the effective temperature, and the thermal temperature, T_i is calculated using Eqn. 4.13. To compare the thermal temperature data to theory, a continuous line representing the thermalization temperature due to DIH as given by Eqn. 3.1 is also shown. The above data-set had initial plasma parameters as $2E_e/3k_B = 116 \pm 3$ K, $n_0 = 2.31 \pm 0.2 \times 10^{15} \text{ m}^{-3}$.

ions, having a Gaussian distribution, falls off with increasing distance from the center. For high densities, the correlation is strong among the ions, and thus temperature is high because of disorder induced heating (DIH). In fact, a continuous line is shown in each of Figs. 5.4(b) and 5.5(b), which represents the thermalization temperature due to DIH temperature as given by Eqn. 3.1, to compare it to the T_i data. Ideally, all the thermal temperature plots should have lied on the continuous line. But as we can see, Eqn. 3.1 can only be used as a rough guide for the thermal temperature when it is extracted via T_{eff} . In fact, if we notice the variation of T_i for later delay times (see Fig. 5.6), then we even get negative thermal temperatures, which is physically not possible. This can be because of the non-neutrality of the outer portion on the plasma (because Eqn. 4.13 itself is obtained by assuming quasi-neutrality of the charges), or probably because we are trying to stretch our technique too far by trying to extract a small T_i from a large T_{eff} (see Fig. 5.6). In short, we can say that although by finding T_{eff} from absorption imaging and annular analysis, we can in principle get the ‘thermal temperature’, we need to modify our theories or change our experimental techniques so that it we would get the real thermal temperature.

We solve the above problem by altogether changing the way we image our plasma. We do this by using fluorescence spectroscopy and the detailed procedure is mentioned in the following chapters. Using fluorescence imaging, we are able to get the real thermal temperature primarily for two reasons. One, because we are no longer restricted to image in the direction of the laser (as is the case in absorption), and thus, we

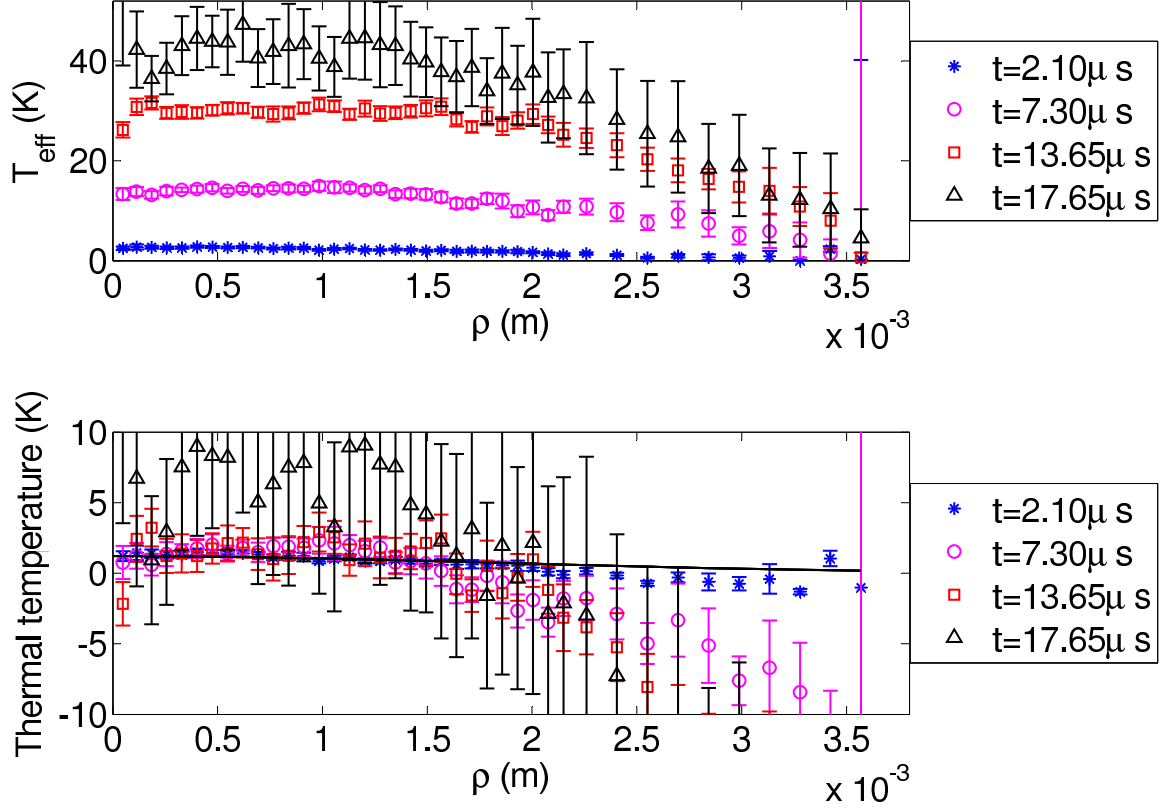


Figure 5.6: Plot of effective temperature, T_{eff} and thermal temperature, T_i , versus ρ for later evolution times. Here, $2E_e/3k_B = 60 \pm 3$ K, $n_0 = 2.42 \pm 0.2 \times 10^{15} \text{ m}^{-3}$. It can be seen from the figure that the thermal temperature data deviate a lot from the theoretical thermalization temperature, some of the data being negative too. This primarily happens because we are trying to extract a small temperature (T_i , of the order of 1K) from a large T_{eff} (of the order of 50 K). This calls for modifications in the theory or changing the experimental techniques. We choose the later.

can image the plasma in a perpendicular direction to the exciting laser. The second reason is that in this case, we are able to separate the Doppler shift due to expansion velocity and the Doppler broadening due to the thermal temperature, thus making them distinguishable.

5.4 Results-Rydberg atoms

As it was already mentioned in section 2.2, we can also make Rydberg atoms using our photoionizing setup. So, let us see what our probes can tell us about the dynamics of these Rydberg atoms. Analysis of two datasets, with set electron temperatures as -20 K and -10 K, is presented in this section. Although, the electrons are supposed to be in a bound state after plasma formation, nevertheless, they quickly evolve to free states due to collisions between Rydberg atoms and blackbody photo-ionization [16]. The resultant electron temperature can be found out from the variation of T_{eff} with time. That analysis is out of the scope of this thesis, but it was found that the -20 K electron temperature evolves to 42 K and -10 K goes to 40 K (The reader can see [24] to see the analysis technique). Since our tool here allows us to look at the number and thermal temperature spatially, we can try to see if studying their distribution can lead us to find out how Rydberg atoms evolve into ions. For example, the density distribution can tell us where Rydberg atoms are being converted into ions quickly. Also, since disorder induced heating depends on ion density only, we can tell where we have predominantly more ions.

First, let us start by looking at the regional number variation. Experimental data of the number versus position for various delay times (before expansion has set in) is shown in Fig.5.7, and the data is also fit to Eqn.5.2. As it can be seen from the curves and the fits, the experiment fits the theoretical curve very well, and that means that as far as the imaging probe is concerned, it gives the information that the

density is Gaussian in this case too implying presence of ions only. So, have all the Rydberg atoms converted to ions in this time scale? We cannot answer the question completely with this data because the Rydberg atoms could be behaving the same way as the ions to the imaging probe.

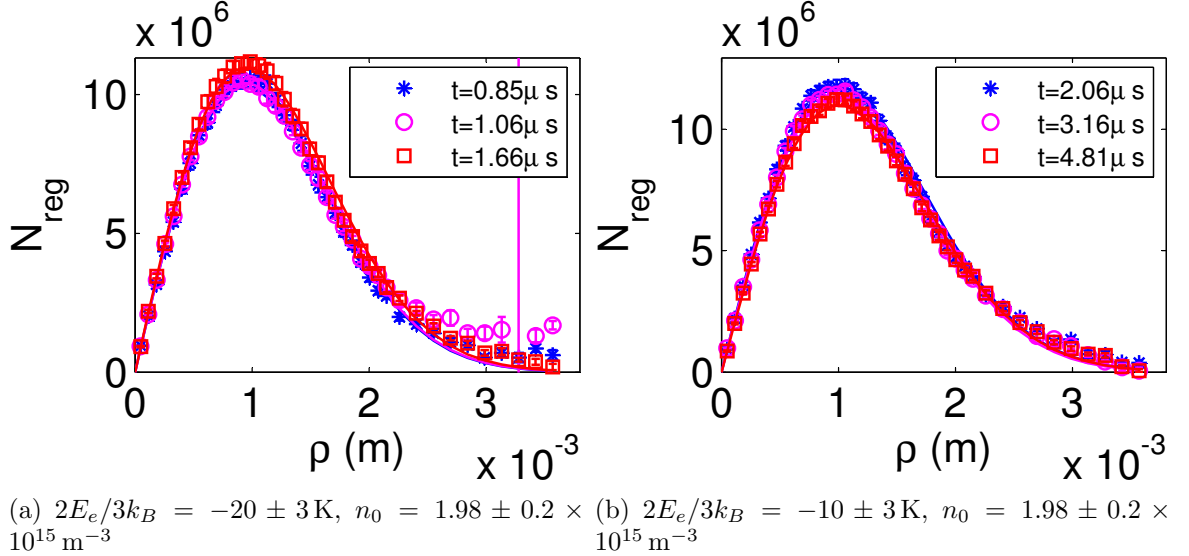


Figure 5.7: Plot of N_{reg} versus ρ for Rydberg atoms. The data is fit to Eqn. 5.2 which tells us that the plasma density is Gaussian in nature.

What we know for sure is that correlation effects will only be there among the ions and not among the Rydberg atoms. This correlation will heat up the ions (due to DIH) only. So, let us see if we can find any information by studying the thermal temperature distribution of the plasma. Since in the previous section we found out that the extraction of T_i from T_{eff} does not work very well, we will study T_{eff} for early times only as it will be close to the thermal temperature, as the expansion has not set in yet. Plots of T_{eff} for the two datasets are shown in Figs. 5.8 and 5.9. The

data is compared to that of a photo-ionized plasma (circular markers in the figure), which had similar ion density and whose set electron temperature was 14K. This data set had a peak density of $n_0 = 2.2 \pm 0.2 \times 10^{15} \text{ m}^{-3}$, which is comparable to that of the Rydberg atoms ($n_0 = 1.98 \pm 0.2 \times 10^{15} \text{ m}^{-3}$). From the analysis to find out the fitted electron temperature, it was found out that the -20 K and -10 K Rydberg atoms evolved to 42 and 40 K respectively, and 14 K evolved to about 23 K respectively. This fact comes about in the T_{eff} profile too (Figs. 5.8 and 5.9), where, it can be seen that T_{eff} increases very rapidly with time compared to the other normal plasma data. Thus, we see that T_{eff} here has contribution from the expansion energy and can not be treated as pure thermal temperature. Apart from this, it can also be seen from the comparison that the effective temperature for the Rydberg atoms is slightly lower than the normal plasma at the lowest time. This is despite the fact that the evolved temperature in the case of Rydberg atoms is higher than for the ordinary plasma. This gives us indication that we could be seeing this as all the Rydberg atoms might not have been converted to ions, and thus, disorder-induced heating is lower in this case.

Unfortunately, the expansion sets in the ions sets rather very quickly, and comparison between the Rydberg atoms and plasma temperature becomes difficult. Thus, instead of comparing the Rydberg data to other data sets, I am also plotting T_{eff} versus ρ for the earliest possible times that we have. These plots are given in Figs. 5.10 and 5.11. Unfortunately, at this point, apart from getting the spatial distribution

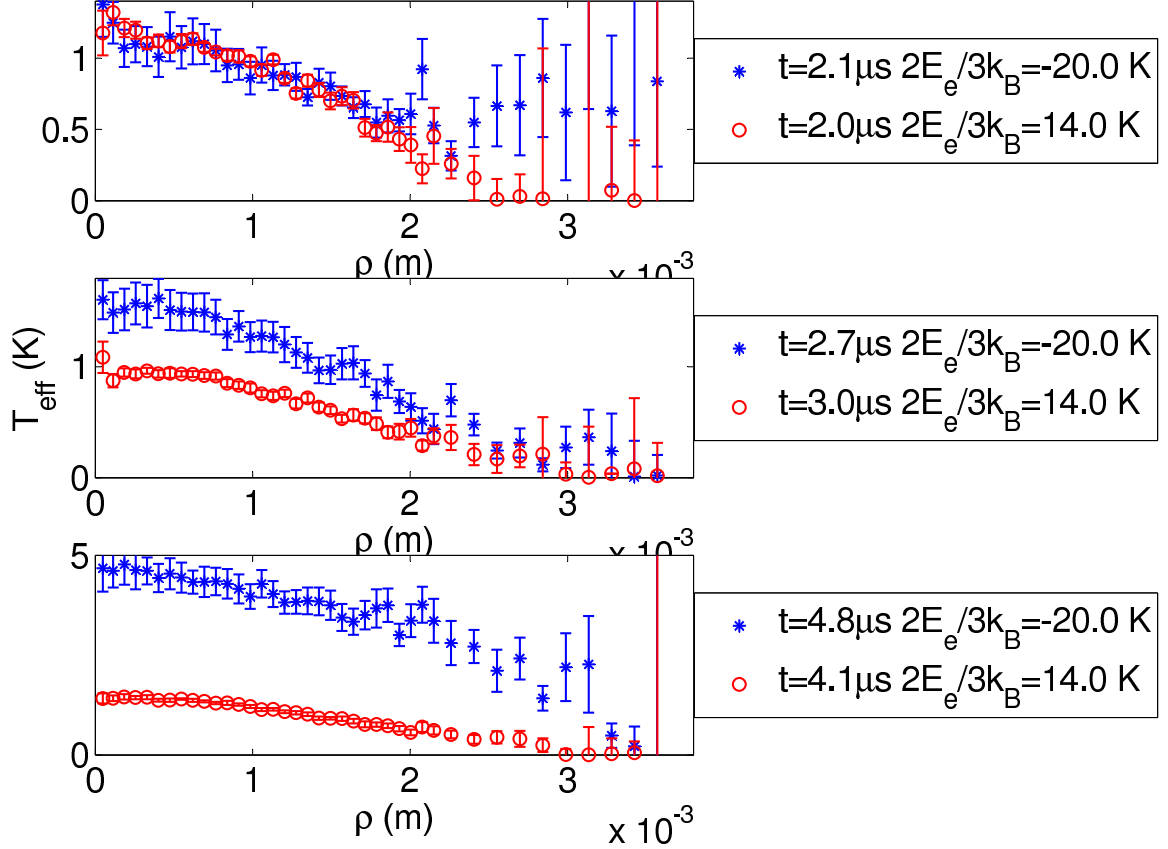


Figure 5.8: Plot of effective temperature, T_{eff} versus ρ evolution for Rydberg atoms with initial electron temperature = -20 K. The points with blue colored asterisk are the temperature of Rydberg atoms. The data is compared to that of a photo-ionized plasma (circular markers), whose set electron temperature was 14K. This data set had a peak density of $n_0 = 2.2 \pm 0.2 \times 10^{15} \text{ m}^{-3}$, which is comparable to that of the Rydberg ($n_0 = 1.98 \pm 0.2 \times 10^{15} \text{ m}^{-3}$).

of the effective temperature, we can't infer much from these curves because of the absence of a model to extract thermal temperature properly from the effective temperature. Numerical simulations on our plasma conditions will probably help in getting the effective temperature directly and then we can compare our data to the result.

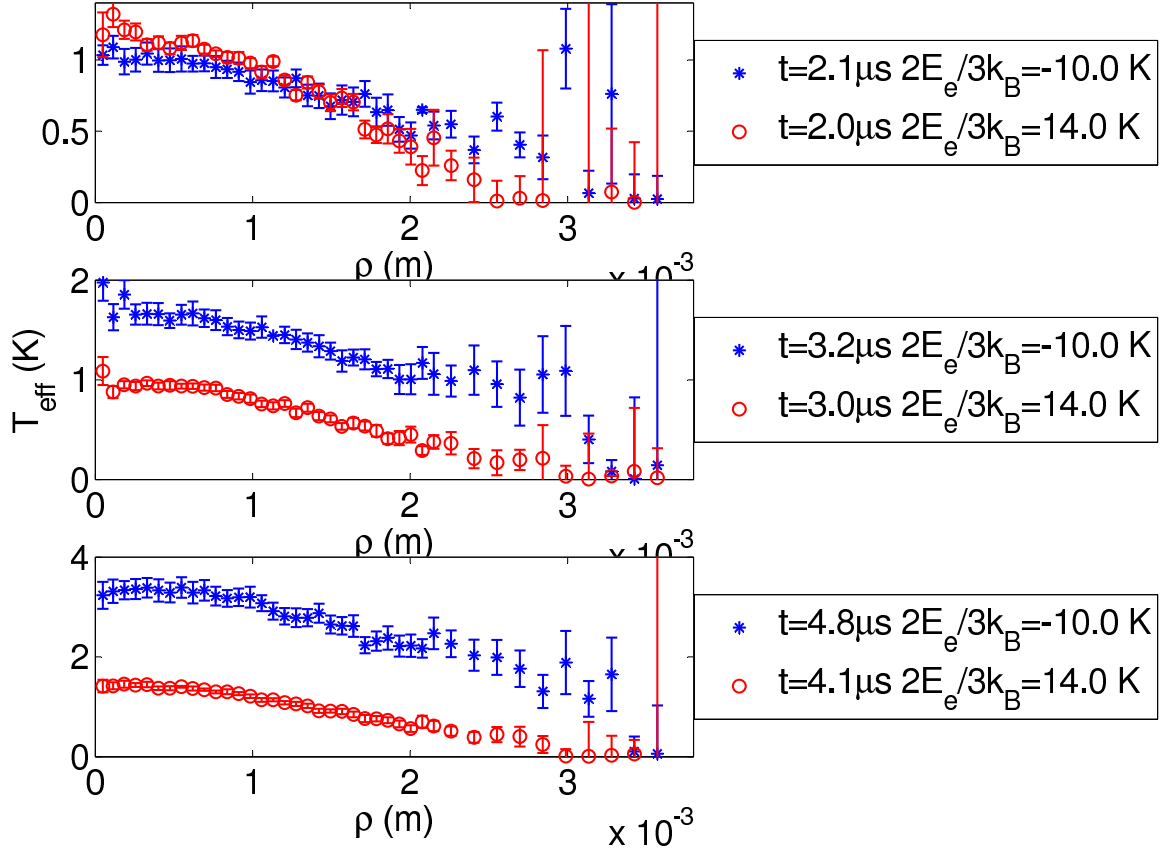


Figure 5.9: Plot of effective temperature, T_{eff} versus ρ evolution for Rydberg atoms with initial electron temperature = -10 K. The points with blue colored asterisk are the temperature of Rydberg atoms. The data is compared to that of a photo-ionized plasma (circular markers), whose set electron temperature was 14K. This data set had a peak density of $n_0 = 2.2 \pm 0.2 \times 10^{15} \text{ m}^{-3}$, which is comparable to that of the Rydberg ($n_0 = 1.98 \pm 0.2 \times 10^{15} \text{ m}^{-3}$).

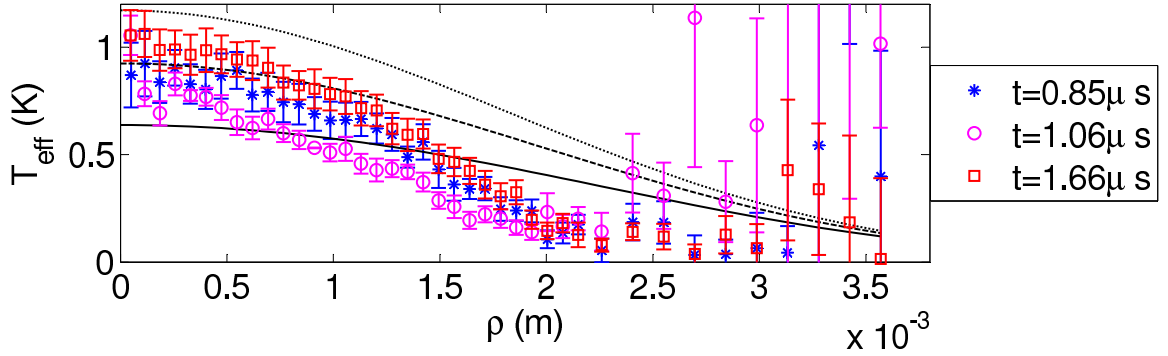


Figure 5.10: Plot of effective temperature, T_{eff} versus ρ evolution for Rydberg atoms with initial set electron temperature, $2E_e/3k_B = -20$ K. This data set had a peak density of $n_0 = 1.98 \pm 0.2 \times 10^{15} \text{ m}^{-3}$. The lines drawn are computed thermal temperature (according to Eqn.3.1) for the same density and corresponding electron temperatures of $T_e = 5$ K (continuous), $T_e = 15$ K (dashed) and $T_e = 50$ K (dotted).

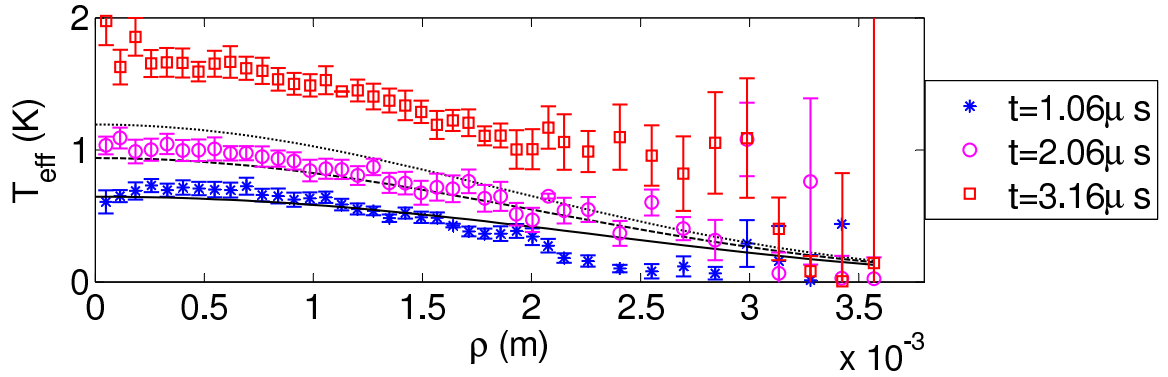


Figure 5.11: Plot of effective temperature, T_{eff} versus ρ evolution for Rydberg atoms with set initial electron temperature, $2E_e/3k_B = -10$ K. This data set had a peak density of $n_0 = 1.98 \pm 0.2 \times 10^{15} \text{ m}^{-3}$. The lines drawn are computed thermal temperature (according to Eqn.3.1) for the same density and corresponding electron temperatures of $T_e = 5$ K (continuous), $T_e = 15$ K (dashed) and $T_e = 50$ K (dotted).

Chapter 6

Diagnostics of UCNP - Fluorescence Imaging and spectroscopy

6.1 Introduction

We saw in the last chapter how absorption imaging falls short in our goal to extract the thermal temperature after the first few μs . Here, we will learn about another imaging technique (fluorescence), and how using spatially resolved spectroscopy with it, we can extract the thermal temperature of the ions in our plasma. In fact, this is the first experimental demonstration of the use of fluorescence spectroscopy in UCNP. By knowing the thermal temperature of the ions, we will be able to probe whether the plasma is undergoing adiabatic cooling. Also, since fluorescence gives us greater signal-to-noise, which gives us the ability to image the plasmas at later times (we have even imaged at $50 \mu\text{s}$), we will also probe Gaussian expansion of the density distribution using fluorescence imaging.

6.2 Importance of fluorescence imaging

As described in 4.3, in (laser induced) fluorescence, when a laser is incident on a matter (here, ions in our plasma), it absorbs the light and then re-radiates the light which we observe as fluorescence. Analyzing the signal with respect to frequency of the incident light and even position can give us information about the temperature, density and $1/\sqrt{e}$ size of the ions. This is the main principle of absorption or fluorescence imaging.

Fluorescence imaging has two distinct advantages. First one being increased signal to noise. This happens because, unlike absorption imaging, we don't have to subtract a background when the laser is present, thus reducing the intensity fluctuations that the laser profile might have. The second advantage is that we can do fluorescence imaging in almost any direction (barring the direction of the laser and the polarization axis of the light) that our apparatus gives us freedom to do, whereas in absorption imaging, we are restricted to imaging along the direction of the laser.

The second advantage of fluorescence imaging is that it allows us to image the plasma along a direction orthogonal to that of the laser. This enables us to actually get the signal from a particular velocity class of ions which are resonant to the laser frequency. Using this technique and spatially resolved spectroscopy, we are able to separate the (small but random) thermal temperature from the (large but directional) expansion velocities. This will be clear by observing the schematic of our fluorescence setup in Fig. 6.1. In this case, the fluorescence beam (assuming it to be detuned by an

amount δ) is traveling along the y -direction. Because of this non-zero detuning, the laser will be in resonance with a particular velocity class of ions whose y projection of velocity ($\mathbf{u} \cdot \hat{y}$) equals λ times the detuning. Since, the average radial acceleration of the ions is caused by the thermal pressure of the electrons, ion expansion velocity can be expressed in the form of $\mathbf{u} = \gamma(t)\mathbf{r}$ [26, 21]. Thus, the Doppler shift due to this velocity will be equal to $\mathbf{u} \cdot \mathbf{k} = \gamma(t)\mathbf{r} \cdot (k\hat{y}) = \gamma(t)ky$. This would mean that due to this Doppler shift, the center of our signal will be shifted from the center of the plasma cloud along the laser direction. This signal will be broadened due to the thermal velocities though, because of the randomness of the thermal velocities. This fact is shown in Fig. 6.1, where an actual image of the plasma is shown on the right. Now, if we choose a small region in the image and vary the laser detuning, the total signal that changes inside the region would purely reflect the change in the Doppler broadening due to the thermal velocities. This is because of the fact that upon varying the frequency, the resonant expansion velocity points will lie outside the small region. Thus, if we plot the spectrum (change of signal with respect to the laser frequency) of the total signal that we obtain in the small region only, it will be Doppler broadened by only the random component of the velocities, thus giving us the thermal temperature. To get quantitative results, let us obtain the expression for the signal and spectrum for the case of fluorescence.

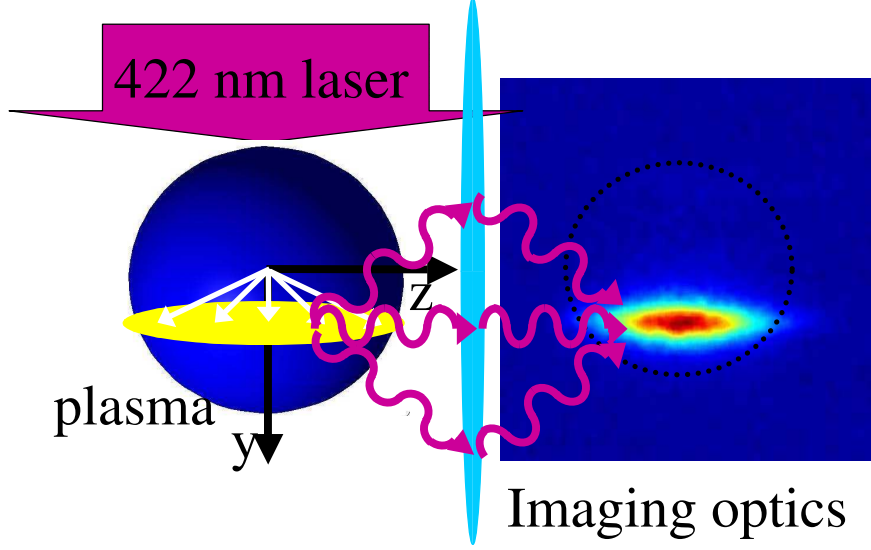


Figure 6.1: Fluorescence imaging of Sr ion is done using the $^2S_{1/2} \rightarrow ^2P_{1/2}$ transition. Depending on the detuning of the laser, a particular velocity class of ions (whose y projection of velocity equals λ times the detuning) are resonant with the beam. The x -axis in the figure is out of the plane of the paper.

6.3 Fluorescence imaging

To derive the fluorescence signal, we start from the expression of the absorption cross section, $\alpha(\nu, T_i, \nu^{\hat{k}})$ from Eqn. 4.1 in section 4.3, and note the fact that since the laser is propagating along y in case of fluorescence, the Doppler shift in the expression is given by $\nu^{\hat{k}} = u_y/\lambda = \gamma(t)y/\lambda$. Also, it should be pointed out here that in fluorescence imaging, the laser beam will have an attenuation along the y axis due to absorption by the plasma cloud. If we represent this absorption by $G_1(x, y, z, \nu)$, then it will be given by

$$G_1(x, y, z, \nu) = \exp \left[- \int_{-\infty}^y dy' n_i(x, y', z) \alpha(x, y', z, \nu) \right]. \quad (6.1)$$

When there is no absorption, $G_1 = 1$. Let us see by how much G_1 can deviate from 1. To calculate this, we know that the maximum value of the absorption cross section, α , is $\lambda^2/2$. Taking the peak density of ions as 10^{15} m^{-3} , and the σ of the cloud as 1 mm, it can be calculated that $G_1 = 0.8$. Thus, as a first order of approximation, G_1 can be assumed to be unity.

Similarly, any fluorescence signal that we measure on our camera will be attenuated due to absorption by the plasma cloud along the imaging (z) axis. If we represent this absorption by $G_2(x, y, \nu)$, then it will be given by

$$G_2(x, y, z, \nu) = \exp \left[- \int_{-\infty}^z dz' n_i(x, y, z') \alpha(x, y, z', \nu) \right]. \quad (6.2)$$

Using a similar treatment as that of G_1 , it can be shown here too, that the minimum value of G_2 is 0.8. So, as a first approximation, we can assume G_2 to be also equal to 1.

In light of all this and using the expression of absorption cross section, $\alpha(\nu, T_i, \nu^k)$ from Eqn. 4.1, we can write the expression for the fluorescence signal as

$$F(\nu, x, y) = \frac{\gamma_0}{2} \frac{\theta_s}{4\pi} f_{dip} f_{DE} \int_{-\infty}^{\infty} \frac{dz n_i(r)}{\sqrt{2\pi}\sigma_D[T_i(r)]} \frac{I(\mathbf{r})G_1(x, y, z, \nu)}{I_{sat}} G_2(x, y, \nu) \times \int_{-\infty}^{\infty} ds \frac{\gamma_0/\gamma_{eff}}{1 + \left[\frac{2(\nu-s)}{\gamma_{eff}/2\pi} \right]^2} \times \exp \left\{ - \frac{[s - \nu_0 - \gamma(t)y/\lambda]^2}{2\sigma_D^2[T_i(r)]} \right\}, \quad (6.3)$$

where we have neglected the effects of power broadening because in our case the

intensity of the laser, $I(\mathbf{r})$, is about 26 mW/cm^{-2} , whereas, the saturation intensity of the ${}^2\text{S}_{1/2} \rightarrow {}^2\text{P}_{1/2}$ transition for a linearly polarized light, is $I_{sat} = 114 \text{ mW/cm}^{-2}$. The factor $\gamma_0/2$ is there in the above expression because that is the highest rate at which ions can fluoresce from the ${}^2\text{P}_{1/2}$ to the ${}^2\text{S}_{1/2}$ state. The constant θ_s is the solid angle in which we collect the light and is equal to 0.15 steradian and f_{dip} is a constant arising due to the dipole radiation pattern. The detector collection efficiency, f_{DE} , for our CCD camera is about equal to 0.1. To get absolute calibration (mostly to get the exact number of $f_{dip} \cdot f_{DE}$) of the fluorescence signal, we often use it in conjunction with absorption spectroscopy. It should also be noted that if we neglect any absorption of the fluorescent beam by the plasma (which we do as a first order of approximation), the intensity profile, $I(\mathbf{r})$, in the above expression will have a typical Gaussian distribution and is given by

$$I(\mathbf{r}) = I_0 \exp\left(-\frac{2x^2 + 2z^2}{w^2}\right), \quad (6.4)$$

where, $w = 6 \text{ mm}$ is the $1/e^2$ radius of the laser profile, and $I_0 = 26 \text{ mW/cm}^{-2}$ is the peak intensity.

As mentioned earlier, we can use our fluorescence probe to measure the spatial profile of the plasma cloud. For this, we see that the total fluorescence signal profile over x and y , when summed over frequency, is proportional to the density averaged

intensity of light along the z direction. This means for $G_1 = G_2 = 1$,

$$\int d\nu F(\nu, x, y) \propto \int dz n_i(r) I(\mathbf{r}). \quad (6.5)$$

Experimentally, the integral of the signal over frequency space is done by adding images taken at equal frequency intervals. Further, using Eqn.6.4 in the above expression, we have

$$\begin{aligned} \int d\nu F(\nu, x, y) &\propto \int dz n_0 \exp\left(-\frac{x^2 + y^2 + z^2}{2\sigma^2}\right) I_0 \exp\left(-\frac{2x^2 + 2z^2}{w^2}\right) \\ &\propto \rho_{areal}(x, y) I_0 \exp\left[-x^2 \left(\frac{1}{2\sigma^2} + \frac{2}{w^2}\right) - \frac{y^2}{2\sigma^2}\right]. \end{aligned} \quad (6.6)$$

As can be inferred from the above expression, if the fluorescence laser's $1/e^2$ radius is big enough compared to the plasma size, σ , then, the correction term $2/w^2$ can be neglected and we would image a symmetric Gaussian expansion along x and y . But in reality, $w = 5.86$ mm, is comparable to the size of the plasma cloud during expansion, and this manifests itself in images showing an unsymmetric expansion as shown in Fig.6.2. We notice from the above expression that the y -axis is free from the laser size correction, and in the figure, that direction shows us the real expansion that the plasma is going through. Whereas, in the x -axis, due to the term $2/w^2$, the expansion seems slower than along that of y .

This variation of the observed sizes along x and y will be better understood, if we first extract the respective sizes. To do this, the plasma images as shown in Fig.6.2

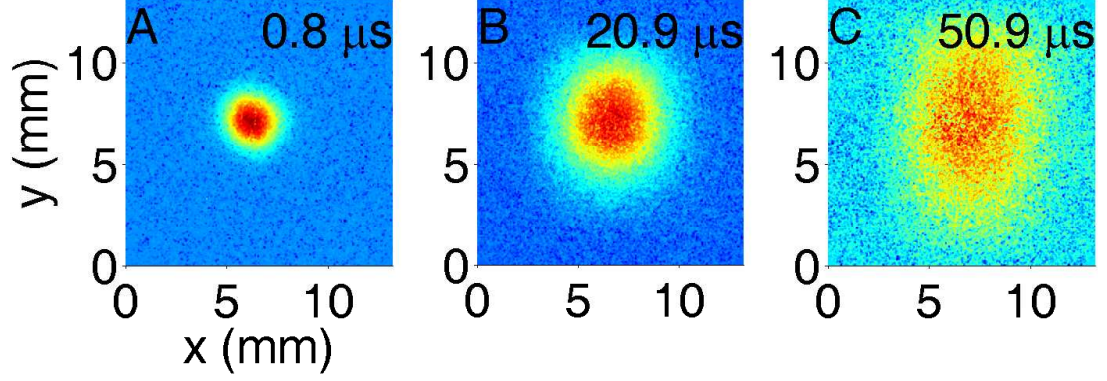


Figure 6.2: Fluorescence images showing expansion of the plasma. The indicated time is time after photoionization. In (A), the plasma is small enough that the correction term $2/w^2$ can be neglected in Eqn. 6.6 and we image a symmetric Gaussian size along x and y . By (C), the finite size of the fluorescence excitation laser elongates the plasma fluorescence, even though the expansion is spherically symmetric. This distortion must be accounted for in order to accurately measure the size and areal density, as in Eq. 6.6. The data shown here has initial electron temperature of $2E_e/3k_B = 105 \pm 3$ K, initial peak ion-density of $n_0 = 18 \pm 0.2 \times 10^{15} \text{ m}^{-3}$, and initial size, $\sigma_0 = 0.84 \pm 0.1$ mm.

is fit to a two-dimensional Gaussian profile of the form of $A \exp[-x^2/2\sigma'_x{}^2 - y^2/2\sigma'_y{}^2]$,

where, σ'_x and σ'_y are the respective observed $1/\sqrt{e}$ sizes along the x and y directions.

Comparing this Gaussian expression to that given at Eqn. 6.6, we can see that $\sigma'_y = \sigma$

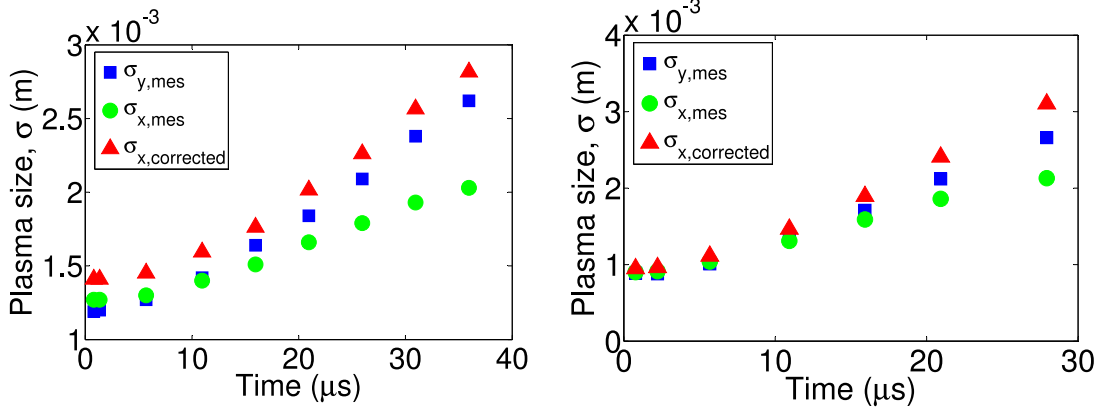
and

$$\frac{1}{2\sigma_x'^2} = \frac{1}{2\sigma^2} + \frac{2}{w^2} \quad (6.7)$$

$$\Rightarrow \sigma = \sqrt{\frac{\sigma_x'^2 w^2}{w^2 - 4\sigma_x'^2}}. \quad (6.8)$$

Thus, we can apply the correction to the observed $1/\sqrt{e}$ size along x and get the actual size σ of the plasma along x . Figure 6.3 illustrates this analysis on the sizes of our plasma. The figures are of two different data-sets having different electron temperature, density and initial sizes. We first plot the observed x and y sizes (circular

and square markers respectively), and as can be seen from the curves, the observed x-size starts deviating from the y-size with increasing time, because, with increasing time, the plasma becomes bigger in size, and the laser size distorts the observed size the most. But as we apply the correction, the corrected x-sizes (triangular markers) match up with the observed y-sizes quite well. This shows that the size anomaly between x and y direction can be understood by properly knowing the laser intensity profile and we can extract the real size of the plasma along x-direction by applying the correction shown in Eqn. 6.8 to the observed x-sizes.



(a) This data-set has initial electron temperature, $2E_e/3k_B = 48 \pm 3$ K, initial peak ion-density of $n_0 = 5.1 \pm 0.2 \times 10^{15} \text{ m}^{-3}$, and initial size, $\sigma_0 = 1.25 \pm 0.1$ mm.

(b) This data-set here has initial electron temperature, $2E_e/3k_B = 105 \pm 3$ K, initial peak ion-density of $n_0 = 18 \pm 0.2 \times 10^{15} \text{ m}^{-3}$, and initial size, $\sigma_0 = 0.84 \pm 0.1$ mm.

Figure 6.3: Size correction along the x-axis. We first plot the observed x and y sizes (circular and square markers respectively), and as can be seen from the curves, the observed x-size starts deviating from the y-size with increasing time, because, with increasing time, the plasma becomes bigger in size, and the laser size distorts the observed size the most. But as we apply the correction, the corrected x-sizes (triangular markers) match up with the observed y-sizes quite well.

6.4 Fluorescence spectroscopy

To do spatially resolved spectroscopy and to get the spectrum, we have to sum the fluorescence signal given by Eqn. 6.3 over a small area $\Delta x \Delta y$ in the $x - y$ (image) plane. In our experiments, we choose a square region where $\Delta x = x_2 - x_1 = 0.05\sigma$ and $\Delta y = y_2 - y_1 = 0.05\sigma$. As a first approximation, assuming $G_1 = G_2 = 1$, and also using the expression of the laser intensity profile from Eqn. 6.4, the spectrum in this region will be given by

$$\begin{aligned}
S_{reg}(\nu) &= \int_{x_1}^{x_2} \int_{y_1}^{y_2} dx dy F(\nu, x, y) \\
&= C \int_{x_1}^{x_2} \int_{y_1}^{y_2} dx dy \int_{-\infty}^{\infty} \frac{dz n_i(r)}{\sqrt{2\pi}\sigma_D [T_i(r)]} \frac{I_0}{I_{sat}} \exp\left(-\frac{2x^2 + 2z^2}{w^2}\right) \times \\
&\quad \int_{-\infty}^{\infty} ds \frac{\gamma_0/\gamma_{eff}}{1 + \left[\frac{2(\nu-s)}{\gamma_{eff}/2\pi}\right]^2} \times \exp\left\{-\frac{[s - \nu_0 - \gamma(t)y/\lambda]^2}{2\sigma_D^2 [T_i(r)]}\right\} \\
&= CN_{reg} \frac{I_0}{I_{sat}} \sqrt{\frac{w^2}{w^2 + \sigma^2}} \exp\left(-\frac{2\tilde{x}^2}{w^2}\right) \int_{-\infty}^{\infty} ds \frac{\gamma_0/\gamma_{eff}}{1 + \left[\frac{2(\nu-s)}{\gamma_{eff}/2\pi}\right]^2} \times \\
&\quad \frac{\exp\left\{-\frac{[s - \nu_0 - \gamma(t)\tilde{y}/\lambda]^2}{2\sigma_D^2 [T_i(\tilde{x}, \tilde{y}, 0.9\sigma)]}\right\}}{\sqrt{2\pi}\sigma_D [T_i(\tilde{x}, \tilde{y}, 0.9\sigma)]} \tag{6.9}
\end{aligned}$$

where, the constant $C = \frac{\gamma_0}{2} \frac{\theta_s}{4\pi} f_{dip} f_{DE}$. Also, in the last expression above, we have replaced the x and y values by their mean values in the integration limits, $\tilde{x} = (x_2 - x_1)/2$ and $\tilde{y} = (y_2 - y_1)/2$. To find out the average value of z to be used in the above equation, we calculated the average thermal temperature of the ions along z using Eqn. 3.1, and also plotted the temperature with respect to z . The result

is shown in Fig.6.4, from which we can see that the average value of the thermal temperature is equal to the actual value of the thermal temperature at $z = 0.9\sigma$. Thus, we substitute 0.9σ as the average value of z in the above expression.

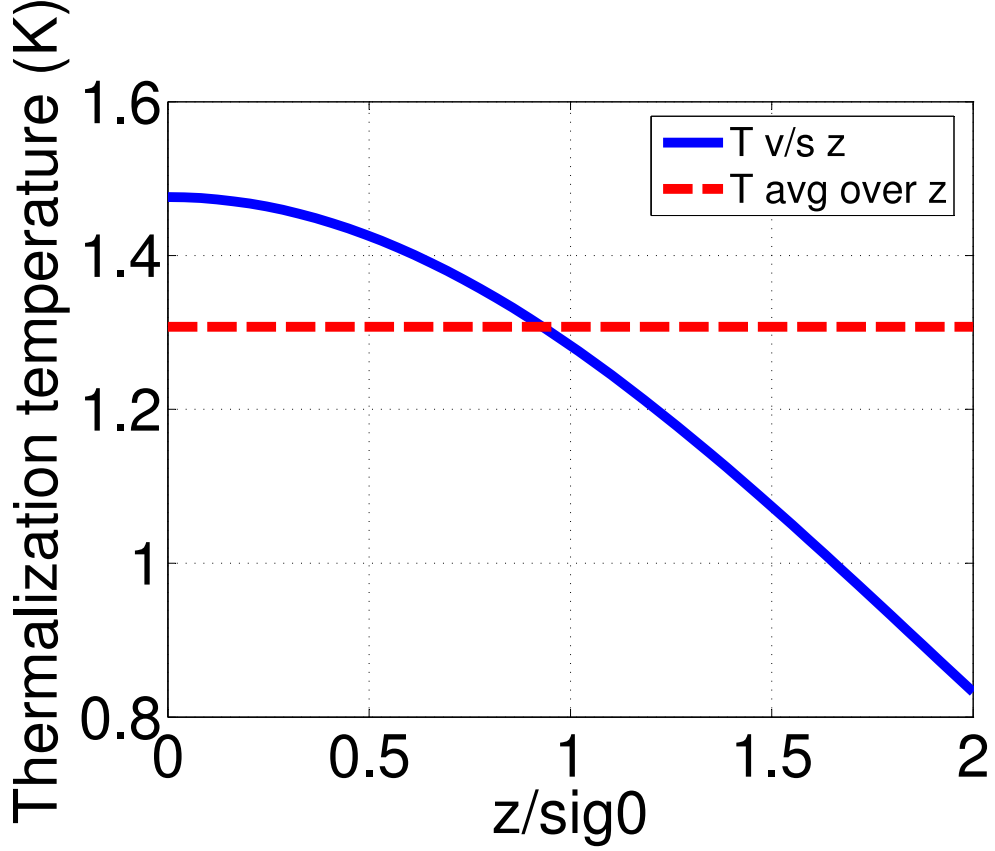


Figure 6.4: Finding average value of z . Plot of the average thermal temperature along z and the actual thermal temperature at z (using Eqn.3.1) is shown here. It can be seen that the average value of the thermal temperature is equal to the actual value of itself at $z = 0.9\sigma$. Although, the peak density of ions used in the plots shown is $n_0 = 5 \times 10^{15} \text{ m}^{-3}$ and the electron temperature as $T_e = 50 \text{ K}$, it was also found out that we get the same result even if we vary the density from 1×10^5 to $6 \times 10^{16} \text{ m}^{-3}$ (keeping $T_e = 50 \text{ K}$) and vary the electron temperature from 5 to 5000 K (keeping $n_0 = 5 \times 10^{15} \text{ m}^{-3}$.)

As we can see from Eqn. 6.9, the fluorescence spectrum of a small region is given by a Voigt profile, which is Doppler shifted by an amount $\gamma(t)\tilde{y}/\lambda$, and Doppler broadened due to the thermal temperature at $x = \tilde{x}$, $x = \tilde{x}$, and $z = 0.9\sigma$. Thus, fitting

the spectrum to a Voigt profile, we will be able to extract the thermal temperature of the ions at a specific region. Although detailed results of the thermal temperatures is presented in the next chapter, Fig. 6.5 shows some of our data, which illustrates the Doppler shift of the spectrum.

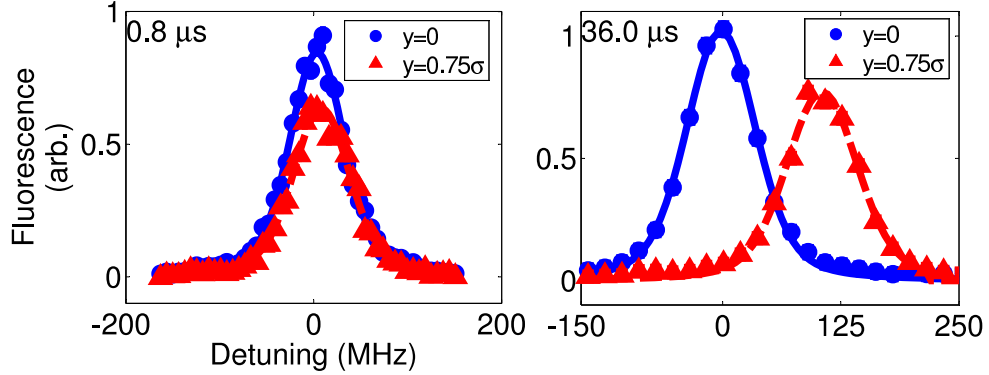


Figure 6.5: Fluorescence spectra of regions. $y = 0$ represents the central region and $y = 0.5\sigma$ represents a region shifted by 0.5σ . The dimensions of both the regions were 0.05σ square. The central region does not show any significant Doppler shift even at higher delay times. Whereas, the outside region ($y = 0.5\sigma$) spectrum is significantly Doppler shifted because the expansion velocity is proportional to both space (r) and time (t).

6.4.1 Spectrum without approximating G_1 and G_2 to 1

If we represent $S'_{reg}(\nu)$ as the spectrum in a small region at (\tilde{x}, \tilde{y}) , without approximating G_1 and G_2 to 1, then it will be given as

$$S'_{reg}(\nu) = S_{reg}(\nu)G_1(\tilde{x}, \tilde{y}, \tilde{z}, \nu)G_2(\tilde{x}, \tilde{y}, \tilde{z}, \nu), \quad (6.10)$$

where, $G_1(x, y, z, \nu)$ and $G_2(x, y, z, \nu)$ are given by Eqns. 6.1 and 6.2. Although, it should be noted that the Doppler shift in the expression of G_1 (due to its dependence on α), will be $\gamma(t)y'/\lambda$, whereas, that of G_2 would be $\gamma(t)z'/\lambda$.

It will be tough to do an exact numerical fitting of our experimental spectrum to Eqn. 6.10. Therefore, the idea here is to first get a theoretical model of the spectrum, assuming that the thermal temperature of the ions at zero time is given by Eqn. 3.1, and varies with time due to adiabatic cooling following Eqn. 3.12c. From this ideal spectrum, we will then calculate the real spectrum ($S'_{reg}(\nu)$) using Eqn. 6.10, and extract the temperature from the real spectrum. We will then compare this extracted temperature with the experimental temperature that we get from the Voigt fitting of Eqn. 6.9. If the temperatures match, then we would be able to say that we observe adiabatic cooling of ions in our system.

6.5 Saturation of the fluorescing level

While doing fluorescence, there is always the risk of saturating the fluorescing transition by having too much intensity (or power) of the laser light, or too much exposure time. If the transition is saturated, then equation 6.3. We therefore, did a study to see if we are in the saturating regime. We were following the rule that if we are not in the saturating regime, then, the total signal that we get keeping the exposure time constant, should vary linearly with the power of the laser.

From the plot in Fig. 6.6 , we can conclude that since we choose an intensity of 26 mW/cm², we won't be in the saturating regime. A similar study also showed that we will not be saturating the transition if we choose an exposure time of up to 3 μ s with 26 mW/cm² of intensity.

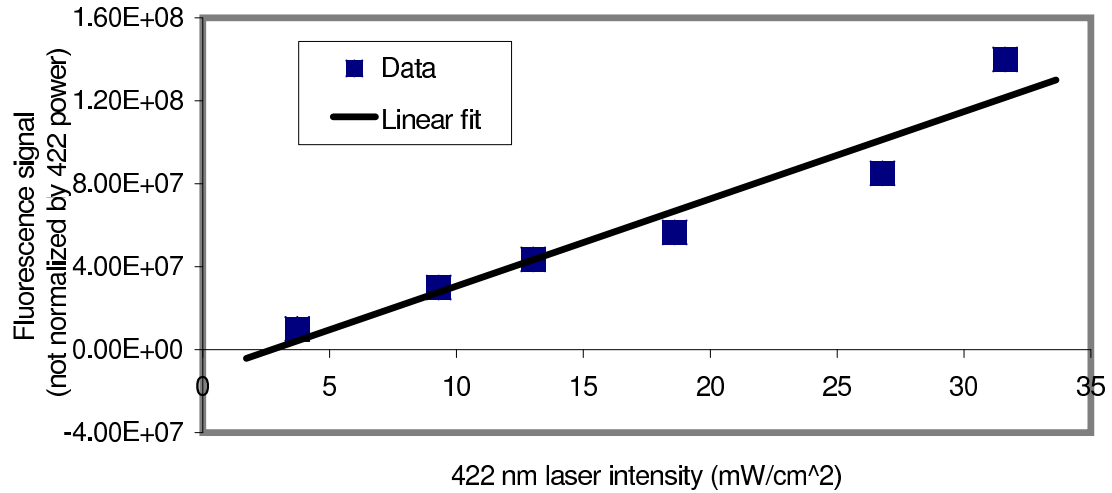


Figure 6.6: The figure shows the data for the peak fluorescence signal (not scaled, and not divided by the laser power) versus the 422 nm laser intensity. A linear fit is also drawn through the points, which shows that at around 26 mW/cm² of intensity, the signal is linear to the power of the laser, showing that we are not in the saturation regime.

6.6 Positioning the camera on image plane

Our imaging optics is set up in a unit magnification telescopic arrangement as shown in Fig. 6.7. The focal length of both the objective and the eyepiece equals 15 cm. The diameter of the objective lens is 2 inch= 5 cm which gives us the f-number as $15/5 = 3$. We wanted to do both absorption and fluorescence imaging with the same optical setup because it is very convenient for us. As the ray diagram in the figure shows, the camera is set so that it can receive the collimated rays in the case of absorption imaging. This is possible because the incoming absorption beam itself is collimated and it passes through unit magnification telescope. Thus, the camera position is not so important in the case of absorption.

But in case of fluorescence, the light will originate from the cloud itself, and it will be focused on a specific point (rather, on the image plane). In order that our imaging

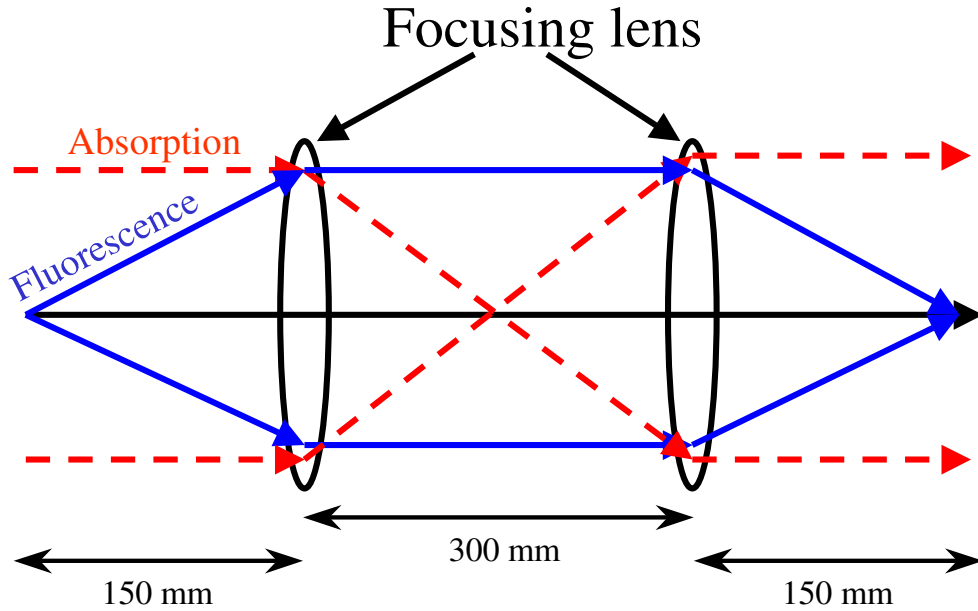


Figure 6.7: Imaging lens setup. The figure shows our imaging optics is set up in a unit magnification telescopic arrangement. The focal length of both the objective and the eyepiece equals 15 cm.

system has one-to-one correspondence, and also so that our resolution is the highest, it becomes very important that the camera itself is placed on the image plane. To achieve this end, we first created plasma and illuminated it with a thin sheet of light propagating along y-axis and whose smaller waist ($1/e^2$ radius) was equal to $40 \mu\text{m}$ and was along the x-axis (pleaser refer to Fig.6.1 for the x,y axes). And then, we moved the camera with a micrometer level translation stage till we got the minimum size image. This implied that the camera is on the image plane now. The figure (left of Fig.6.8) shows the actual image that we obtained from the sheet fluoresced plasma. On the right side of the figure is a Gaussian fit to the image, which gave us the $1/e^2$ radius along the x-axis as $52.5 \mu\text{m}$. This slight increase in the image size compared to the beam size could be because of slight movements of the plasma as we

were doing about 50 sums of image to get a good signal-to-noise ratio.

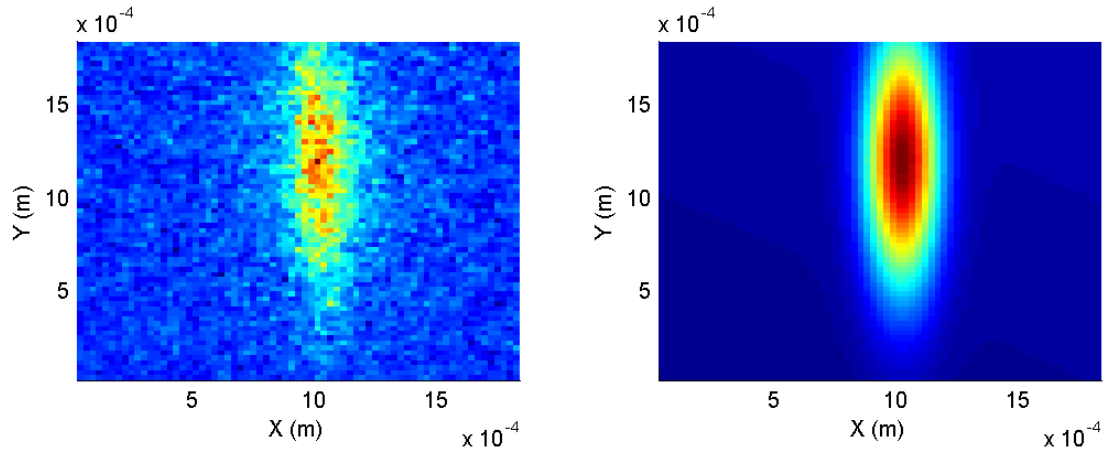


Figure 6.8: Sheet fluorescence image on the camera. The left side image is the real camera image of the plasma when it was illuminated with a thin sheet of light whose waist ($1/e^2$ radius) was equal to $40 \mu\text{m}$. The bright portion of the image is limited along the x-axis because of the laser beam waist, whereas, it is limited along the y-axis because of the Gaussian shape of the plasma. The image on the right side is a Gaussian fit to the image, which gave us the $1/e^2$ radius along the x-axis as $52.5 \mu\text{m}$.

Chapter 7

Results-Fluorescence Data

In this chapter, data from the fluorescence imaging is presented. We have also fitted the various plasma parameters extracted from the data to the theoretical models mentioned in the previous chapter.

7.1 Size expansion of the plasma

To probe the self similar Gaussian expansion, the first thing that we want to see is the spatial profile of the plasma. To achieve this, we follow the cue (mentioned in the previous chapter (Eqn. 6.6)), that the fluorescence signal when summed over frequency space, will have the same Gaussian profile along the y -axis, as the density of the plasma. Thus, we sum all the images that were taken over 50 frequency points, and we get the total summed image. This is the same image as shown in Fig. 6.2.

Now, to get the density profile of the plasma, we sum all the pixel points in a strip along y -axis, which also passes through the center of the plasma. The strip was about 2.6 mm wide which increased the signal to noise in the y -profile of the plasma cloud

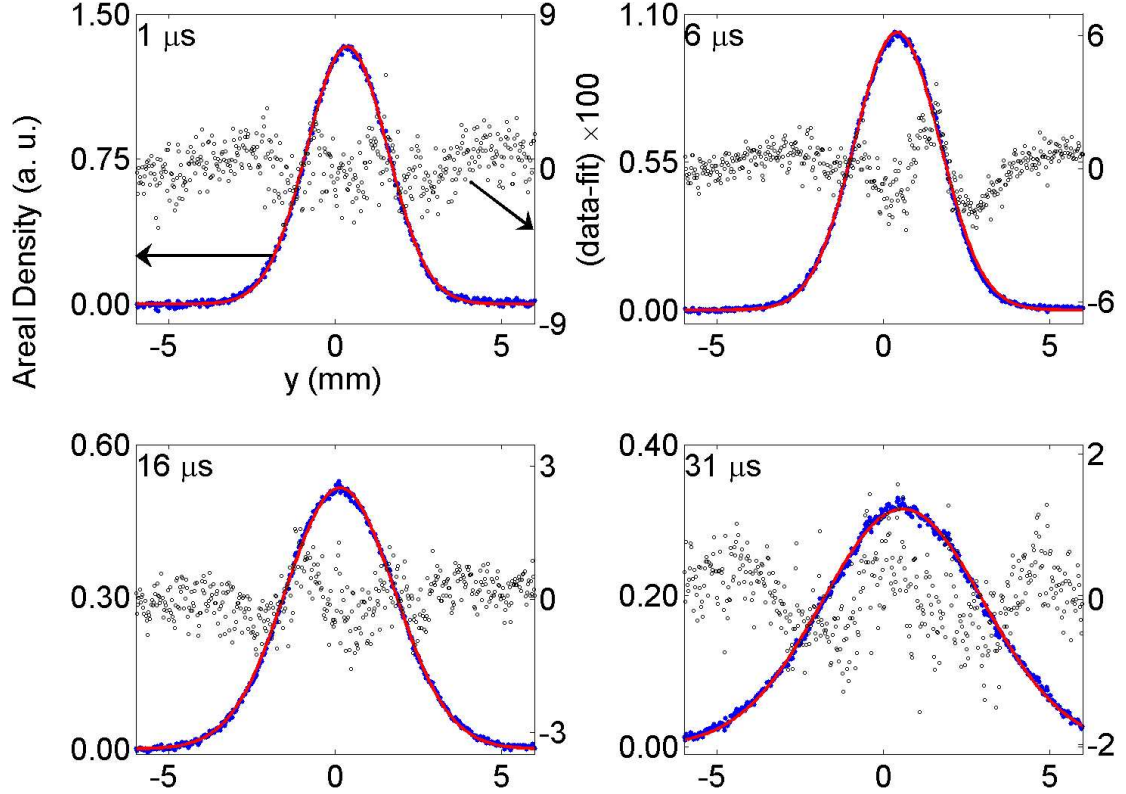


Figure 7.1: Density profile of the plasma shows Gaussian expansion in our plasma. The closed markers are the experimental data points and the continuous curve is a Gaussian fit. The open circles are the residuals (data-fit) times 100. The data has initial electron temperature, $2E_e/3k_B = 48 \pm 3$ K, initial peak ion-density of $n_0 = 5.1 \pm 0.2 \times 10^{15} \text{ m}^{-3}$, and initial size, $\sigma_0 = 1.25 \pm 0.1$ mm.

¹. Three such figures are shown in figures 7.1, 7.2 and 7.3, where each of the figure refer to various different initial condition of plasma formation. In each figure, plots of areal density (which is the spatial profile of the plasma) is plotted with respect to various expansion times mentioned in the upper left corner of the plots. The data is also fitted to a Gaussian function, and as can be seen from the plots, the data follows the Gaussian function really well. In fact, to get a measure of the deviation from

¹The reader can see Appendix B for an analysis where the strip width was smaller than this case, and was equal to $52 \mu\text{m}$. A width of $52 \mu\text{m}$ corresponds to 2 pixels in our plasma image, thus making this the minimum width of the strip (so that at least some averaging can be performed)

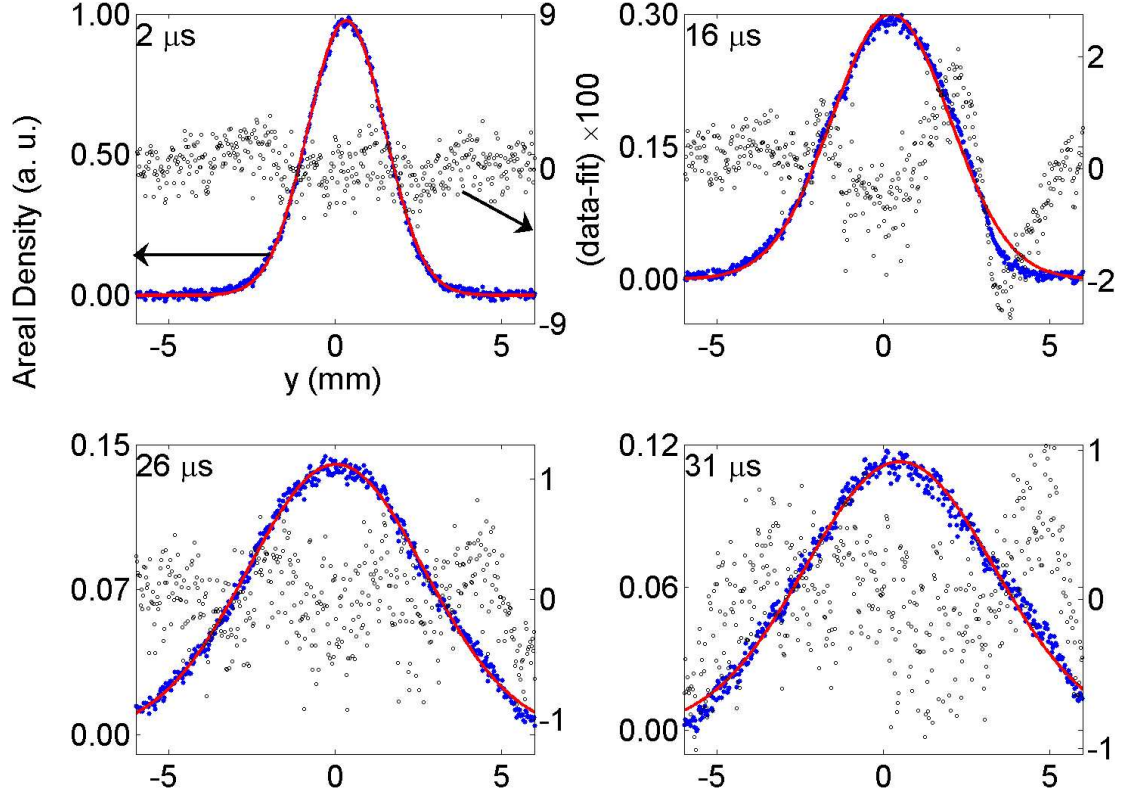


Figure 7.2: Density profile of the plasma shows Gaussian expansion in our plasma. The closed markers are the experimental data points and the continuous curve is a Gaussian fit. The open circles are the residuals (data-fit) times 100. The data has initial electron temperature, $2E_e/3k_B = 105 \pm 3$ K, initial peak ion-density of $n_0 = 2.8e15 \pm 0.2 \times 10^{15} \text{ m}^{-3}$, and initial size, $\sigma_0 = 1.2 \pm 0.1$ mm. In the top-right plot, the experimental data can be seen to be significantly less than the theory for $y > 3.5$ mm. This happened (as we later found out) because the frequency scan range for this particular time ($16 \mu\text{s}$) did not extend so much so that the full plasma could be imaged.

theory, we have plotted the residual along the right side of the y coordinate axis.

This shows that the residuals are well within 0.03 in value. This is a direct proof that the ultracold plasma is indeed undergoing a self similar expansion, a key condition for Vlasov equation solutions to be valid in collisional system.

From the last figure of these data sets (Fig. 7.3), it can be seen that the points are more scattered about the fitted function for two of the latest delay times compared to the other plots. This is because the last delay time in this data set is about $50 \mu\text{s}$, and

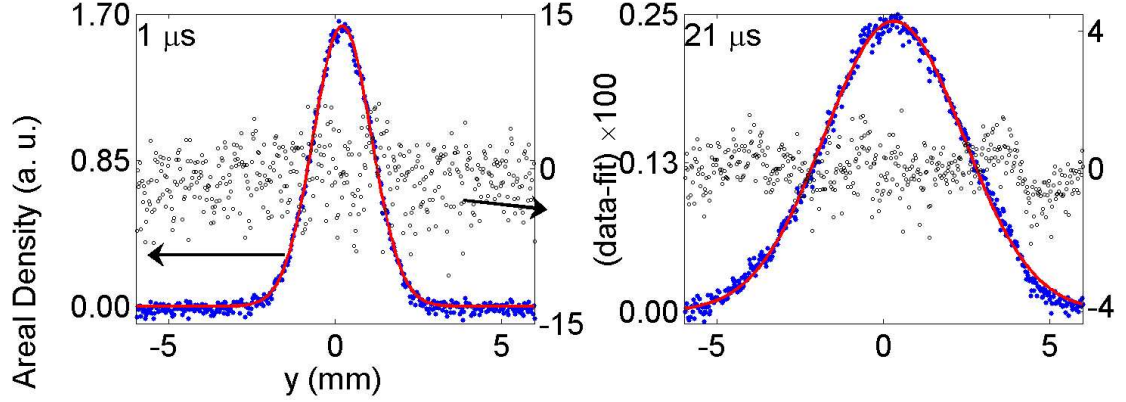


Figure 7.3: Density profile of the plasma shows Gaussian expansion in our plasma. The closed markers are the experimental data points and the continuous curve is a Gaussian fit. The open circles are the residuals (data-fit) times 100. The data has initial electron temperature, $2E_e/3k_B = 105 \pm 3$ K, initial peak ion-density of $n_0 = 18 \pm 0.2 \times 10^{15} \text{ m}^{-3}$, and initial size, $\sigma_0 = 0.84 \pm 0.1$ mm. In the plots for 21, 28 and 51 μs , the experimental data can be seen to be significantly less than the theory for higher values of y . This happened (as we later found out) because the frequency scan range for those particular times did not extend so much so that the full plasma could be imaged.

also because this data set had the highest electron temperature ($2E_e/3k_B = 105 \pm 3$ K) and the lowest initial size, $\sigma_0 = 0.84 \pm 0.1$ mm. These initial conditions made the expansion rate the highest in this data set.

It can also be observed from the figures (7.1, 7.2 and 7.3), that the width of the Gaussian profile of the plasma is increasing with time too. This is because due to the expansion, the size of the plasma is changing with time. Plotting the $1/\sqrt{e}$ size of the plasma (σ) with respect to time, we can also probe if the plasma is undergoing

the theoretical expansion given by Vlasov equation solution (Eqn. 3.12a). To do this, we fit the total summed image of the plasma (as shown in Fig. 6.2) is fitted to a 2-dimensional Gaussian and the $1/\text{sqrt}(\sigma)$ size along the y-axis are plotted with respect to time as shown in Fig. 7.4. In the figure, the markers are the data, and the continuous line is the theoretical curve mentioned in Eqn. 3.12a, which yields $T_e(0)$ which matches reasonably well with the expected value $2E_e/3k_B$. Lot of physics can be learned from the plots. For instance, there are two datasets which have the same initial size, but different initial electron temperature (the blue square data has $2E_e/3k_B = 105$ K and the red triangles has $2E_e/3k_B = 48$ K). It can be clearly seen that the dataset having the higher electron temperature expands with a faster rate, thus showing that the expansion is propelled by the electron's energy. Also, there are two more data sets (blue squares and green circles) which have the same electron temperatures, but different initial sizes. It can be also seen that the data-set having the lower initial size has the faster expansion rate, which signifies that the smaller the size, the higher the electron pressure, and thus faster the expansion rate. Also, the fact that the data is a good fit to Vlasov solutions (with the certain conditions shown in section 3.4), proves that there are no significant collisional or radiative processes in the plasma.

7.2 Fluorescence spectrum and temperature determination

As mentioned in the previous chapter (section 6.4), we can do spectroscopy with our fluorescence imaging to extract the thermal and total (thermal plus expansion)

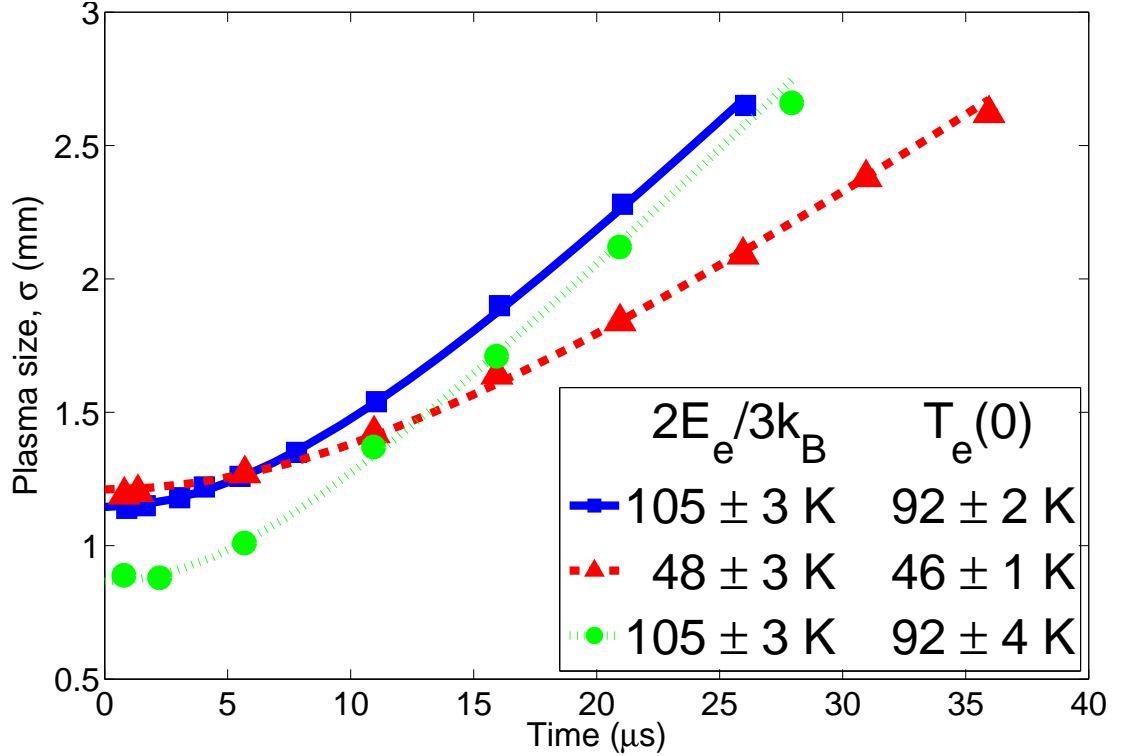


Figure 7.4: Plasma size versus time. The markers are the data, and the continuous line is the theoretical curve mentioned in Eqn. 3.12a, which yields $T_e(0)$ which matches reasonably well with the expected value $2E_e/3k_B$. Uncertainties in $2E_e/3k_B$ reflect 1-standard-deviation calibration uncertainty in the wavelength of the photoionizing laser. Quoted uncertainties in $T_e(0)$ are statistical, but there is an additional systematic uncertainty of a few percent arising from calibration of the imaging-system magnification and overlap of the plasma and fluorescence excitation laser. Statistical uncertainty in the measurement of σ is less than the size of the plotting symbols. This figure is taken from [27].

part of the kinetic energy. Here, I first present the analysis done on the image as a whole. After this, I will also present the results of spatially resolved spectroscopy. If the spectrum is calculated by analyzing the whole image of the plasma, then the Doppler broadening in the spectrum will have contribution from both the expansion and thermal part of kinetic energy. Four such spectra plots at various times are shown in Fig. 7.5.

It can be clearly seen from the spectra (Fig. 7.5), that initially, the width of the

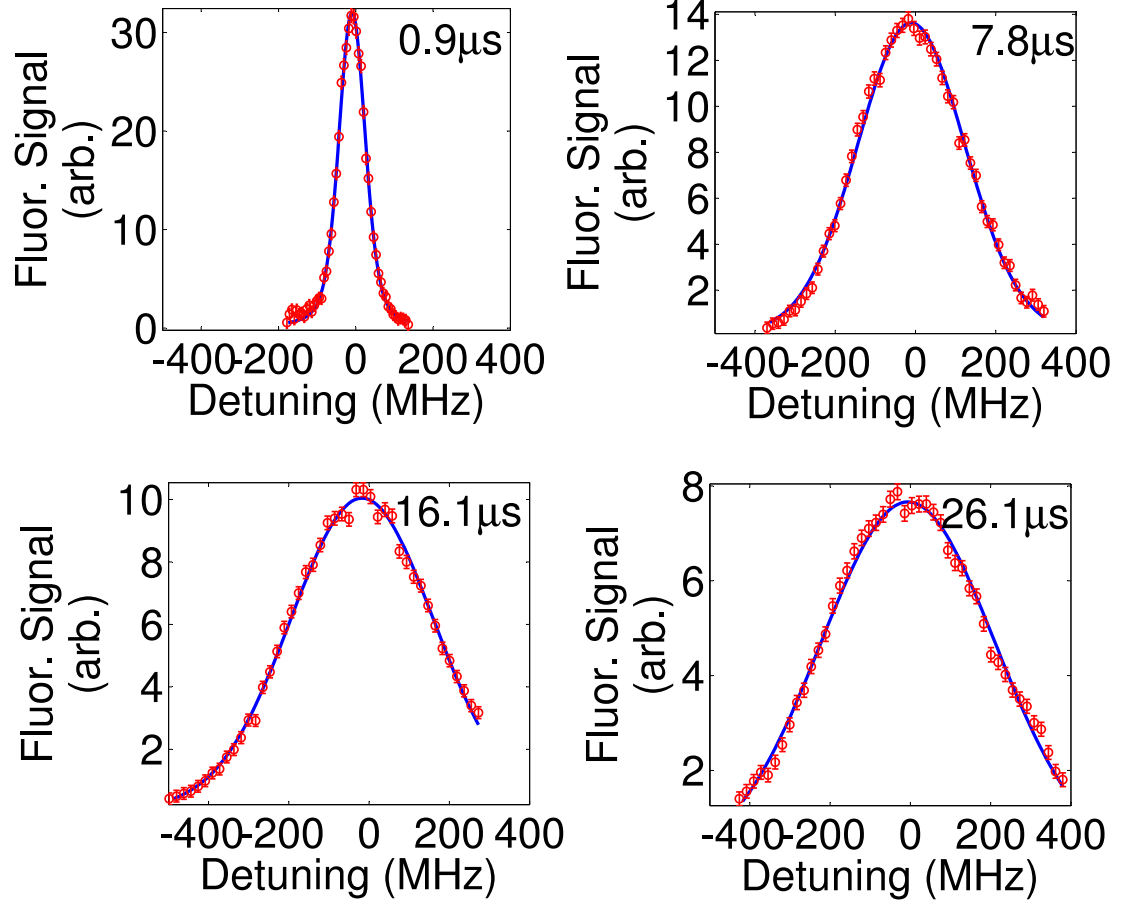


Figure 7.5: Spectra plots versus time. The markers are the fluorescence spectrum data with initial electron temperature, $2E_e/3k_B = 105 \pm 3$ K, initial peak ion-density of $n_0 = 2.8e15 \pm 0.2 \times 10^{15} \text{ m}^{-3}$, and initial size, $\sigma_0 = 1.2 \pm 0.1$ mm. The continuous line is the fit of the data to a Voigt profile. Note the change in the Doppler width of the spectrum with time, which happens because expansion of plasma kicks in at later time, and increases the total energy of the ions.

spectrum is very narrow (it is in fact almost equal to the Lorentzian linewidth, about 28 MHz), because the expansion has not set in yet. But for later delay times, the Doppler broadening of the spectrum becomes larger because these spectra now have contributions from both thermal as well as expansion velocities. The spectra are then fitted to a Voigt profile (continuous line in Fig. 7.5) and the effective Doppler width ($\tilde{\sigma}$) can be extracted. From this width, effective rms velocity of the ions, $v_{i,\text{rms}} = \lambda \tilde{\sigma}$

can be obtained. This velocity when plotted with respect to time (Fig. 7.6) can give us information about the expansion characteristics and we can also verify the Vlasov solutions experimentally. To do this, we fit the $v_{i,\text{rms}}$ data to its theoretical expression given by Eqn. 3.12c. In the figure, the continuous and dashed lines represent this fit, and from the figure we can see that the data matches the theory very well. This is another direct verification of Vlasov equation solutions in our system. In the figure, the offset that $v_{i,\text{rms}}$ has in earliest time arises due to the initial heating of the ions due to disorder induced heating. After this (between 5 to 20 μs), the ions undergo heating due to electron pressure (expansion). After this time, the electrons start cooling adiabatically and that cooling is reflected in the ion rms velocity heating rate slowing down and then achieving a terminal velocity. It can also be seen that this terminal velocity is higher for higher electron temperature and lower for the lower electron temperature. Thus we believe with the fluorescence probe, we have been able to map the expansion completely.

7.3 Spatially resolved spectroscopy

As it can be seen from the previous figure (Fig. 7.6), the highest $v_{i,\text{rms}}$ is about 90 m/s, which implies the total effective temperature of the ions to be about 70 K. To extract the thermal temperature (which is just of the order of 1-3 K) is a tough job. But the fluorescence probe, along with spatially resolved spectroscopy, is very useful in resolving the thermal temperature from the huge expansion energy. So, let's see

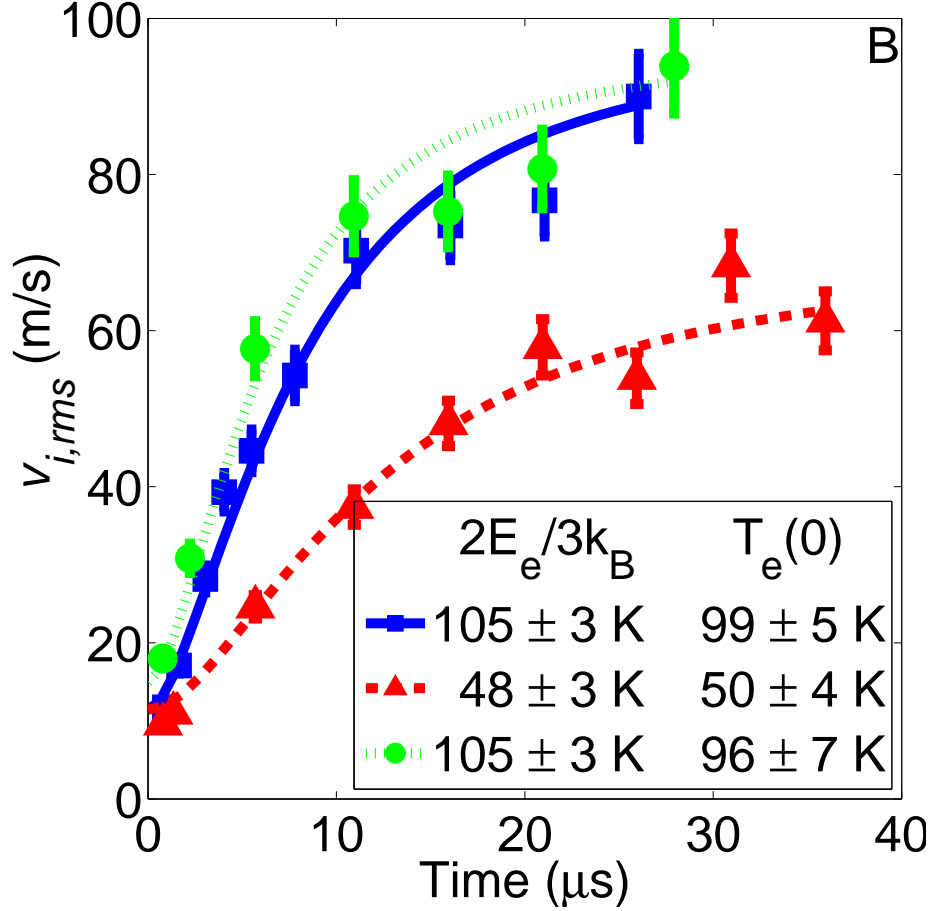


Figure 7.6: RMS velocity versus time. This figure is taken from [27]. Effective rms velocity of the ions, $v_{i,rms}$ can be extracted by fitting fluorescence spectra to a Voigt profile. $v_{i,rms}$ data (markers) is then fit to its theoretical expression given by Eqn.3.12c (lines in the figure). Good match of theory and experiment directly verifies Vlasov equation solutions in our system. In the figure, the offset that $v_{i,rms}$ has in earliest time arises due to the initial heating of the ions due to disorder induced heating. After this (between 5 to 20 μs), the ions undergo heating due to electron pressure (expansion). After this time, the electrons start cooling adiabatically and that cooling is reflected in the ion rms velocity heating rate slowing down and them achieving a terminal velocity. It can also be seen that this terminal velocity is higher for higher electron temperature and lower for the lower electron temperature.

how it is done.

To start with, as explained in the previous chapter (section 6.4), we calculate the spectrum in a very small region $\Delta x \Delta y$, where, as explained, the spectrum should be broadened only due to the thermal temperature. Typical spectra for these small

regions are plotted in Fig. 6.5. In the figure, $y = 0$ represents the central region and $y = 0.75\sigma$ represents a region shifted by 0.75σ . The dimensions of both the regions were 0.05σ square. The central region does not show any significant Doppler shift even at higher delay times, whereas, the outside region ($y = 0.5\sigma$) spectrum is significantly Doppler shifted because the expansion velocity is proportional to both space (r) and time (t). Thus by this technique, we can also study the variation of expansion velocity with respect to time and space (although, it hasn't been studied yet with this probe). It should also be noted here, that the Doppler width of the regional spectra even at $36 \mu\text{s}$ time is not significantly broadened due to the huge expansion velocity. This is direct evidence of the fact that the spectra are not broadened due to the expansion velocity in the regional spectra. Thus, we can say that we have been able to filter out to a large extent the high expansion velocity from the Doppler broadening of the spectra.

We can now fit a Voigt profile (as given by Eqn.6.5) to the spectra as shown in Fig.6.5. From these fits we get the thermal temperature at the region that is being analyzed. A plot of these thermal temperature with time for various datasets is shown in figures 7.7, 7.8 and 7.9. In all the plots, the width of the square region is $\delta_x = \delta_y = 0.05\sigma$. The left most plot is at the center of the plasma, the middle one is shifted by 0.25σ and the right-most plot is shifted by 0.75σ along the y-axis.

From the thermal temperature versus time plots, we see that the temperature first undergoes heating with time and then it starts to cool. The cooling could be happen-

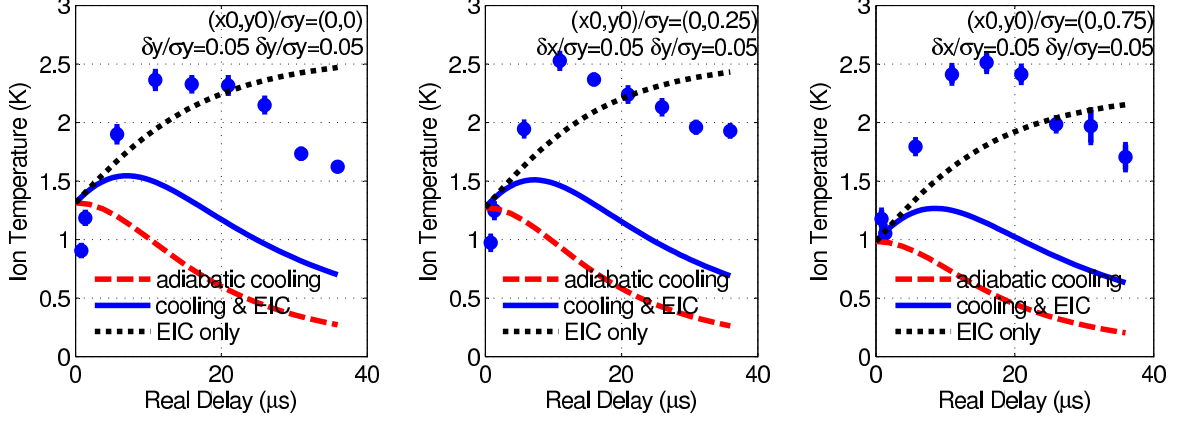


Figure 7.7: Thermal temperature of ions in a small spatial region. In all the plots, the width of the square region is $\delta_x = \delta_y = 0.05\sigma$. The left most plot is at the center of the plasma, the middle one is shifted by 0.25σ and the right-most plot is shifted by 0.75σ along the y-axis. Also plotted are theoretical adiabatic cooling curves (dashed) and adiabatic cooling plus electron ion collisional heating (continuous). The data has initial electron temperature, $2E_e/3k_B = 48 \pm 3$ K, initial peak ion-density of $n_0 = 5.1 \pm 0.2 \times 10^{15} \text{ m}^{-3}$, and initial size, $\sigma_0 = 1.25 \pm 0.1$ mm.

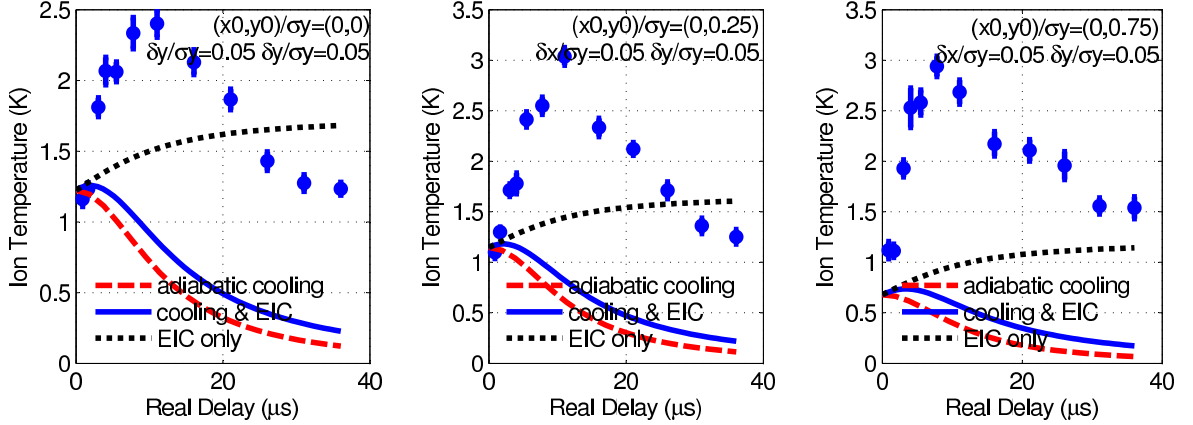


Figure 7.8: Thermal temperature of ions. Same as in Fig. 7.7 with the exception that the data here has initial electron temperature, $2E_e/3k_B = 105 \pm 3$ K, initial peak ion-density of $n_0 = 2.8e15 \pm 0.2 \times 10^{15} \text{ m}^{-3}$, and initial size, $\sigma_0 = 1.2 \pm 0.1$ mm.

ing due to adiabatic cooling of the ions during expansion. But how can we account for the heating? To understand this heating and understand the behavior of ion thermal temperature properly, it should be noted that the theoretical adiabatic cooling expression (Eqn. 3.12c) neglects electron-ion thermalization (or, collision) (EIC). In

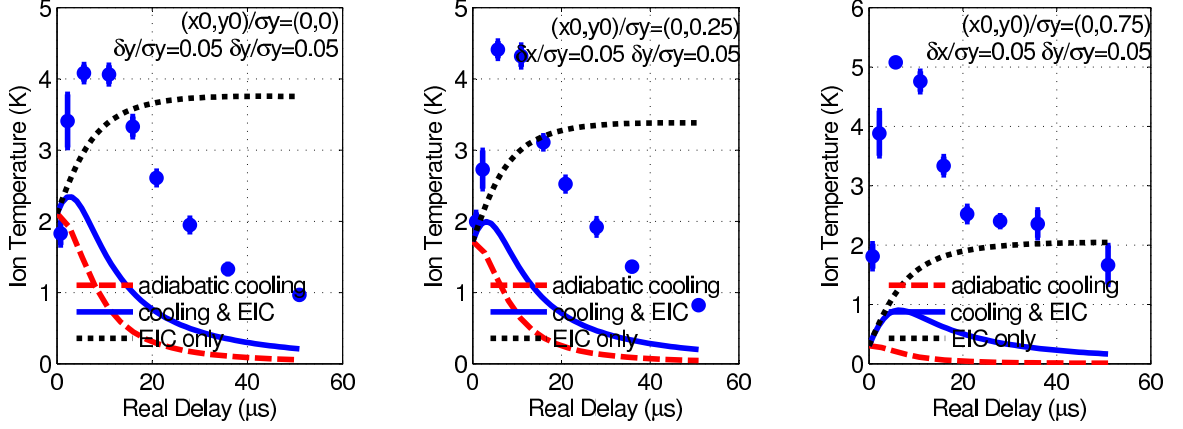


Figure 7.9: Thermal temperature of ions. Same as in Fig. 7.7 with the exception that the data here has initial electron temperature, $2E_e/3k_B = 105 \pm 3$ K, initial peak ion-density of $n_0 = 18 \pm 0.2 \times 10^{15} \text{ m}^{-3}$, and initial size, $\sigma_0 = 0.84 \pm 0.1$ mm.

EIC, electrons and ions undergo collisions and heat is transferred from the hotter species (here, electrons) to the colder species (here, ions). The rate of heat transfer, or more appropriately, the rate of collision, is given by γ_{eic} and depends on the temperature and density of electrons. The expression for γ_{eic} as described by T. Pattard *et al.* in [35], is given by

$$\gamma_{eic} = \sqrt{\frac{2}{3\pi}} \frac{m_e}{m_i} \Gamma_e^{3/2} \omega_{P,e} \ln \Lambda, \quad (7.1)$$

where, Γ_e is the electron Coulomb coupling parameter, $\omega_{P,e}$ is the electron plasma frequency and $\ln \Lambda = \ln(\sqrt{3}/\Gamma_e^{3/2})$ is the so called Coulomb logarithm [35]. A plot of γ_{eic} , as given by Eqn. 7.1, with electron temperature, T_e for various density values is given in Fig. 7.10. As can be seen from the figure, the rate decreases with increasing T_e . This happens because the rate depends on the electron Coulomb coupling parameter Γ_e with a power of $3/2$, and increasing T_e decreases Γ_e . Physically, increasing

temperature can be thought of as decreasing correlations between the electrons, thus reducing the cross-section of electron-ion collisions. It is also noticed from the figure that γ_{eic} increases with increasing electron density. This can also be attributed to the fact that Γ_e increases with increasing density.

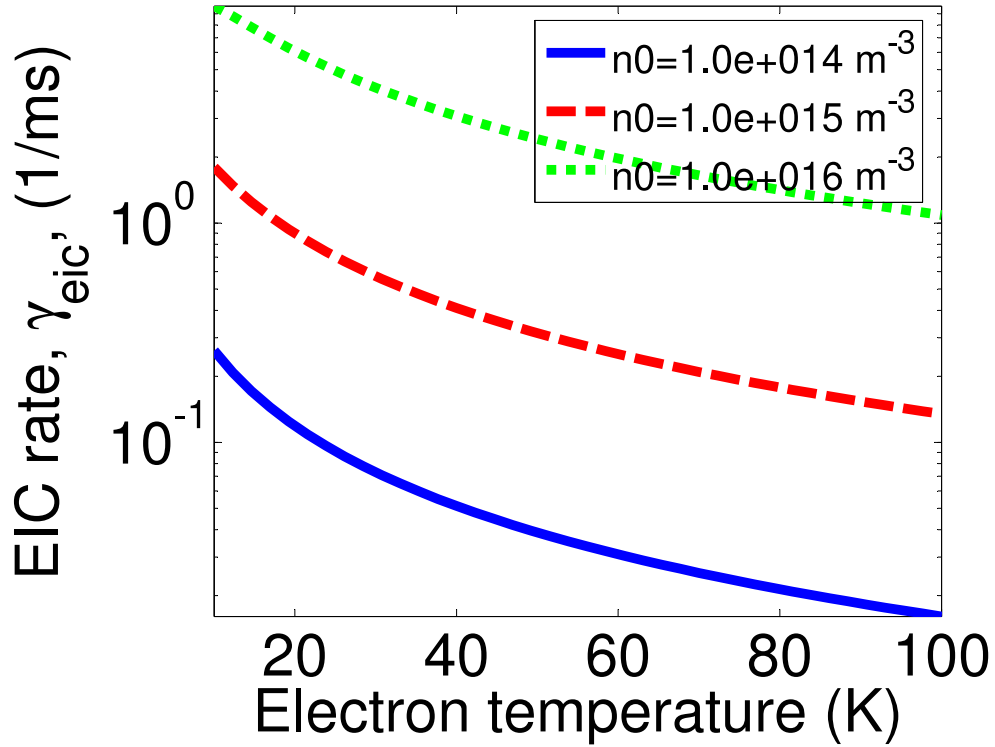


Figure 7.10: Variation of electron-ion collision rate with electron temperature and density. As can be seen from the figure, the rate decreases with increasing T_e . This happens because the rate depends on the electron Coulomb coupling parameter Γ_e with a power of $3/2$, and increasing T_e decreases Γ_e . Physically, increasing temperature can be thought of as decreasing correlations between the electrons, thus reducing the cross-section of electron-ion collisions. It is also noticed from the figure that γ_{eic} increases with increasing electron density. This can also be attributed to the fact that Γ_e increases with increasing density.

With the aid of the plots in the figure, let us calculate how much would electron-ion collisions (EIC) heat up the ions. For example, for the data set given in Fig. 7.7, we have $T_e = 48 \text{ K}$ and density, $n_0 = 5.1 \times 10^{15} \text{ m}^{-3}$. For this condition, we can use

Fig. 7.10, and approximately find out the EIC rate to be about $2 \text{ ms}^{-1} = 2 \times 10^3 \text{ s}^{-1}$. At $10 \mu\text{s}$, this rate would heat up the atoms by approximately $\gamma_{eic} \times T_e \times 10 \mu\text{s}$, which comes out to be roughly equal to 1 K. We see this amount of heating in the data too, where the ion temperature increases from 1.2 K to about 2.4 K. Actually, to calculate the ion temperature due to EIC alone, we have solve the differential equation

$$\frac{\partial k_B T_i}{\partial t} = k_B \gamma_{eic} (T_e - T_i), \quad (7.2)$$

Solution to the above equation is shown in figures 7.7, 7.8 and 7.9 as the black dotted lines. Comparing this plot from the experimental data, we see that the heating behavior of the data could be due to EIC. But after some time, the temperature of the ions stop heating and start cooling down. The heating due to EIC is not able to explain this cooling in any respect, and we believe that this cooling could be due to adiabatic expansion of the ions. This belief is substantiated from the fact that the cooling (deviation of temperature data from EIC theory) is most significant in Fig. 7.9. That data set has the highest electron temperature of all samples (100 K) and the smallest size (0.84 mm), which makes expansion the fastest in that data-set. Thus, adiabatic cooling would be very much dominant in that data set, and we see exactly that from the deviation of the data from the pure EIC curve. Temperature variation with respect to time due to adiabatic cooling alone can be calculated by Eqn. 3.12c. The theoretical curve of the adiabatic cooling (Eqn. 3.12c) is plotted as the red dashed lines in the figures. We can see that adiabatic cooling alone is also

not able to explain fully the behavior of the thermal temperature. So, the question is - are we missing something here?

The fact that we have to remember here is that the adiabatic cooling and EIC is present in every instant of time. In fact, assuming the rate of increase of thermal temperature to be equal to the sum of heating rate due to adiabatic expansion (this term will be negative) and the heating rate due to EIC at any instant of time, the instantaneous thermal temperature, T_i will be given by

$$\frac{\partial k_B T_i}{\partial t} = -2\gamma k_B T_i + k_B \gamma_{eic} (T_e - T_i), \quad (7.3)$$

where, T_e and T_i are the electron and ion temperature respectively and γ_{eic} is the rate of electron-ion collision. Using equations 7.3 and 7.1 above, we can calculate the ion temperature with both adiabatic cooling and EIC heating, the result of which is plotted as continuous lines in the figures 7.7, 7.8 and 7.9. Comparing this theory and our data, and the amount of heating that we see in our data suggests that electron-ion collisional heating starts dominating right from the initial phase of expansion of the cloud. But, adiabatic cooling kicks in eventually, and starts slowing the sample down. This can be seen from the fact that although the dotted curve in 7.7 (which is pure heating due to EIC) is able to roughly explain the heating that we have in our system, but in later time, it fails to match up with the cooling of the sample, which as explained above is most probably happening because of the adiabatic expansion of the cloud. Another observation that we can make from the thermal temperatures

of different regions (for $y = 0$, $y = 0.25\sigma$ and $y = 0.75\sigma$ in Fig. 7.7) is that the experimental temperature is pretty much constant at around 1 K at early time for all the regions. This could be happening if the laser line-width used in the analysis does not exactly match the real laser-linewidth. In our analysis, we have used the laser-linewidth to be equal to 6.72 MHz (which was obtained from Rubidium spectroscopy). But, if the real laser-linewidth is greater than 6.72 MHz, then this would mean that the difference in the linewidths is adding up in the Doppler broadening, and thus, we are not seeing the small change that the temperature is going through. Careful measurement of the laser-linewidth could throw more light on this.

7.3.1 Checking for increase in observed temperature due to re-absorption of fluorescence signal

At this point I would also like to state that the spectral analysis done here is without considering absorption of the fluorescence beams (basically, approximating $G_1=G_2=1$ as given in 6.3). In order to rule out the possibility of the re-absorption of fluorescence signal, we also did a calculation to find out the observed thermal temperature if G_1 and G_2 were to vary. The procedure followed is mentioned in section 6.4.1 and the result is presented in Fig. 7.11 for exactly the same initial conditions ($2E_e/3k_B$, n_0 and σ_0) as in the figures 7.7, 7.8 and 7.9. The circular markers are the ideal thermal temperatures calculated using Eqn. 3.1, and the triangular markers are the observed thermal temperature obtained by fitting a Voigt profile to the generated spectrum (calculating variation of G_1 and G_2 numerically). As it can be seen from

the figure, the observed temperature is higher than the ideal temperature, but the discrepancy is negligible and would be unable to see the kind of heating that we are observing.

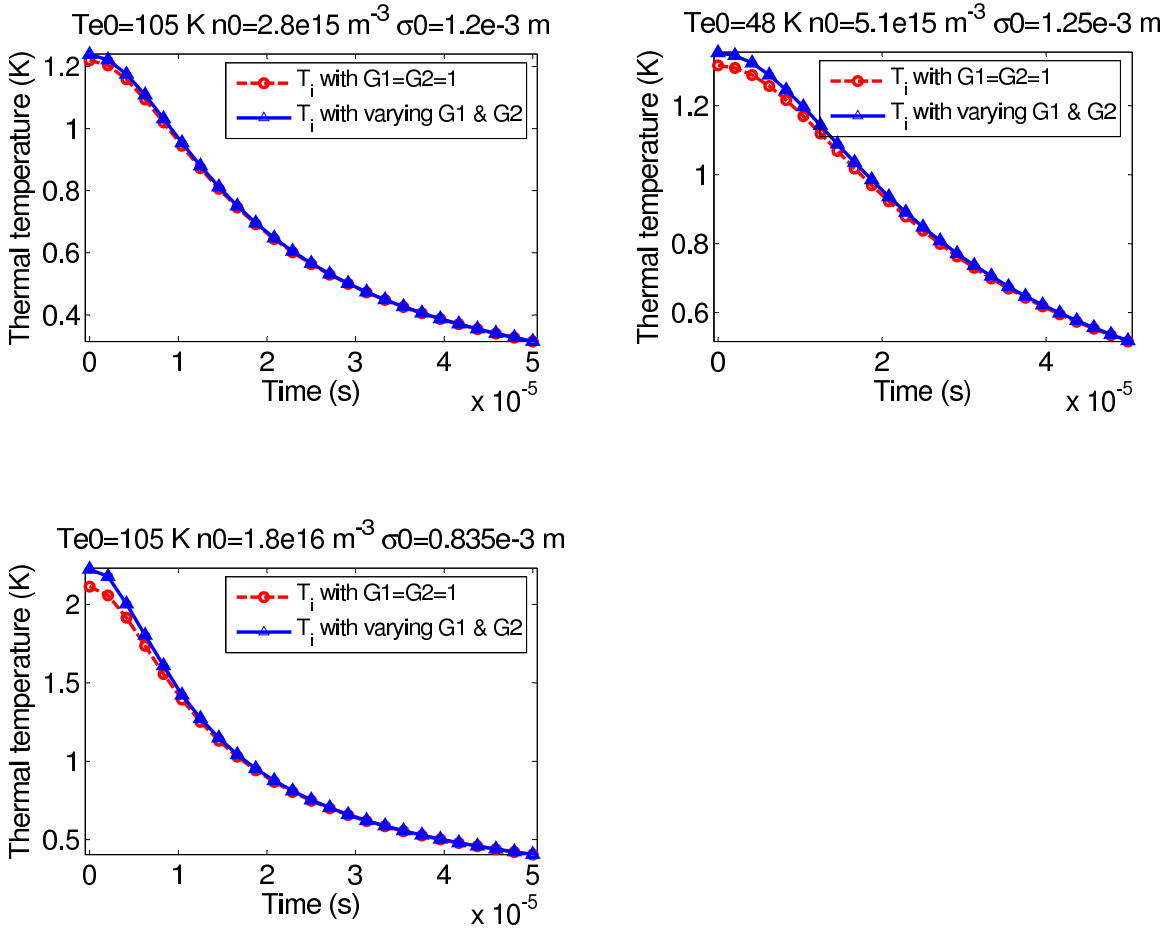


Figure 7.11: Observed thermal temperature with re-absorption of fluorescence signal.

7.3.2 Checking for expansion effect in the experimental thermal temperature

Another test that I performed on our data was to see whether we have any expansion component in the spatially resolved spectra. It is more or less clear from

the thermal temperature plots (figures 7.7, 7.8 and 7.9) that there is no expansion component in our thermal temperature because the temperature for the non-center regions are not significantly higher than the central region. But to get a more concrete result, we increased the width of the region in which the spectrum was calculated. If our data (regional spectrum) have any contribution due to the expansion energy, then we would see the extracted thermal temperature to be higher. This analysis was performed on one of the data set ($2E_e/3k_B = 48 \pm 3$ K), and the new width of the region was chosen as 0.1σ instead of 0.05σ previously. The result is shown in figure below (Fig. 7.12), and it can be seen that the temperature here is a very close match compared to Fig. 7.7 which proves the fact that the temperature that we are measuring is indeed the thermal temperature and we have been able to isolate it from the expansion velocity of the plasma.

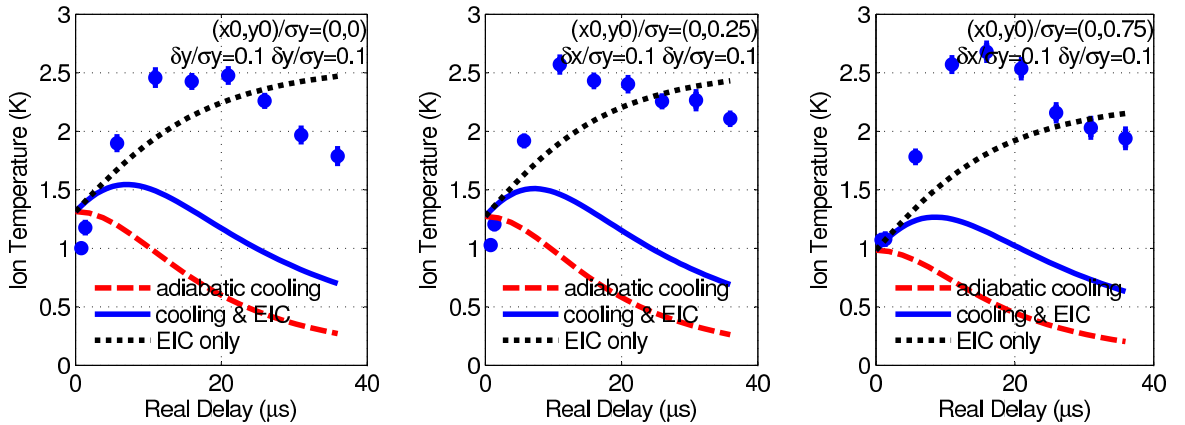


Figure 7.12: Thermal temperature after increasing the width of the spatial region to 0.1σ instead of 0.05σ previously. The data has initial electron temperature, $2E_e/3k_B = 48 \pm 3$ K, initial peak ion-density of $n_0 = 5.1 \pm 0.2 \times 10^{15} \text{ m}^{-3}$, and initial size, $\sigma_0 = 1.25 \pm 0.1$ mm. The temperature here is a very close match compared to Fig. 7.7 which proves the fact that the temperature that we are measuring is indeed thermal temperature and there is not any contribution from the expansion energy.

Furthermore, we wanted to know when actually we start noticing expansion effect in the Doppler broadening of the spectra in our region. To check this, we gradually increased the size of our region (Δ) from 0.05σ to σ and calculated the temperatures by doing spatially resolved spectroscopy. The result is plotted in figure 7.13, where, the left most plot is at the center of the plasma, the middle one is shifted by 0.25σ and the right-most plot is shifted by 0.75σ along the y -axis. From the plots it can be seen that the expansion starts effecting the Doppler width of the regions from $\Delta = 0.25\sigma$. And after this, the effects of expansion is significant, and it is clear from the data, that we won't be seeing any effect of cooling whatsoever. Another observation from the curves is that for a given time and for a given width of the region, the temperature obtained is almost the same for different mean y values. This happens because the Doppler broadening due to the expansion energy depends on the spatial width of the region only, and not on the location of the region.

The variation in the mean y values in the earlier thermal temperature plots (figures 7.7, 7.8 and 7.9), was not too much (it varied from 0 to 0.75σ). We restricted ourselves to this space because the signal to noise was nice, owing to higher density of the plasma near the center. But let us see, if we can increase the variation of the mean y values, and what information would it convey us. Figure 7.14 shows the thermal temperature for $y = \sigma$ and $y = 1.5\sigma$. If we go Beyond $y = 1.5\sigma$, the fitting the spectrum to Voigt gets tougher as we were limited in our frequency scan range, and we see significant Doppler shift in the spectrum for those regions. From figure 7.14, it can be seen that

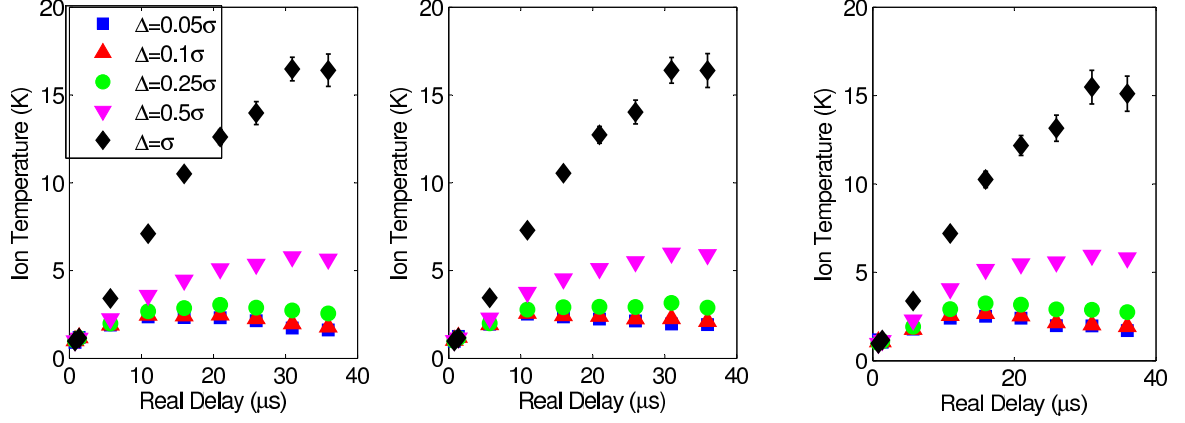


Figure 7.13: Thermal temperature after increasing the width of the spatial region from 0.5σ to σ (in the plots, Δ denotes the width of the region). The left most plot is at the center of the plasma, the middle one is shifted by 0.25σ and the right-most plot is shifted by 0.75σ along the y-axis. This particular dataset has initial electron temperature, $2E_e/3k_B = 48 \pm 3$ K, initial peak ion-density of $n_0 = 5.1 \pm 0.2 \times 10^{15} \text{ m}^{-3}$, and initial size, $\sigma_0 = 1.25 \pm 0.1$ mm. From the plots it can be seen that the expansion starts effecting the Doppler width of the regions from $\Delta = 0.25\sigma$. And beyond this, the effects of expansion is significant, and it is clear from the plots, that we won't be seeing any effect of cooling whatsoever.

for $y = \sigma$, the thermal temperature variation is the same as the inner regions. But we see some heating in $y = 1.5\sigma$, although the data starts becoming lot noisier in this case. This heating could be due to the expansion effect coming in, or it could also be because the plasma might have lost some electrons in this outer region, which lessens the screening between the ions and thus, the ions correlation energy might be heating them up. Two more datasets (figure 7.15), show slight heating for $y = \sigma$ region only. This puts the reason of heating more on expansion because in these datasets, because of the high electron temperature (100 K), we have more expansion compared to the $T_e = 48$ K dataset, and thus, we see heating at $y = \sigma$ only.

To conclude this chapter, I would like to say that by spatially resolved fluorescence spectroscopy, we have been able to isolate and measure the small thermal temperature

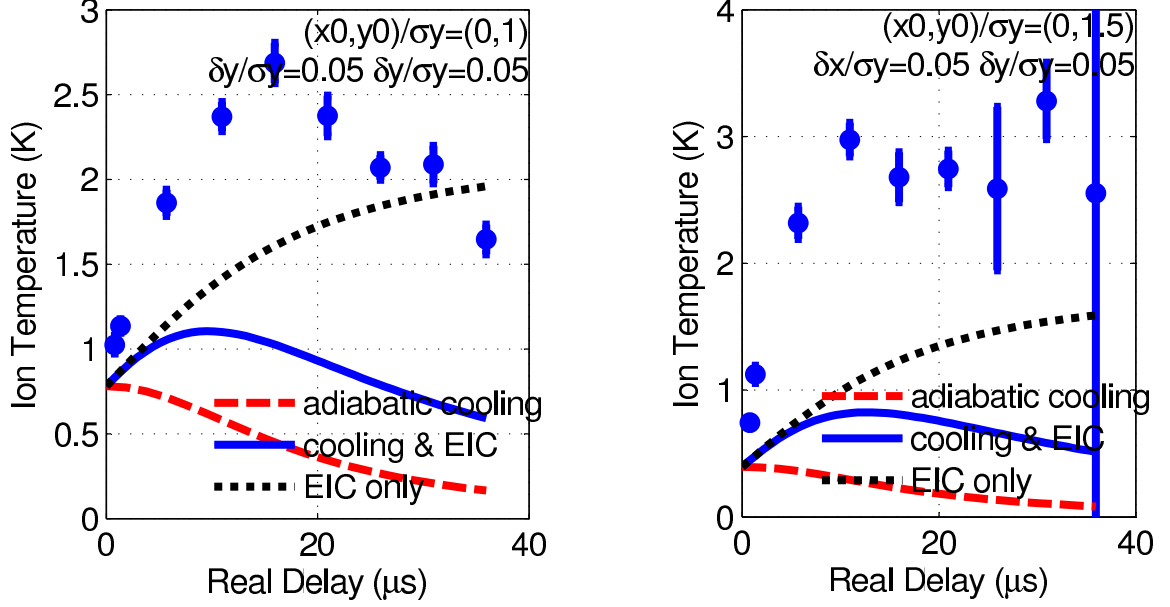


Figure 7.14: Thermal temperature variation in outer regions. This particular dataset has initial electron temperature, $2E_e/3k_B = 48 \pm 3$ K, initial peak ion-density of $n_0 = 5.1 \pm 0.2 \times 10^{15} \text{ m}^{-3}$, and initial size, $\sigma_0 = 1.25 \pm 0.1$ mm. The plots show the thermal temperature for $y = \sigma$ (left) and $y = 1.5\sigma$ (right) both having $\Delta = 0.05\sigma$.

of the ions from the big expansion energy, provided the width of the spatial regions are small enough (smaller than 0.25σ , as we saw above). We also saw that the thermal temperature so extracted first undergoes heating (due to electron-ion collisions) and then it starts cooling due to adiabatic expansion.

The experimental data for the thermal temperature that we got is colder than the theory for the pure EIC heating. And in the same time, it is hotter than the theoretical value that comes only from adiabatic cooling. At this point of time, we believe that that the two processes could be contributing in a different manner than is currently accepted. For example, EIC could be setting in too early in our data and/or adiabatic expansion could be setting in too late. In the same note, from our experimental data, we can also see how much more EIC would be able to explain the

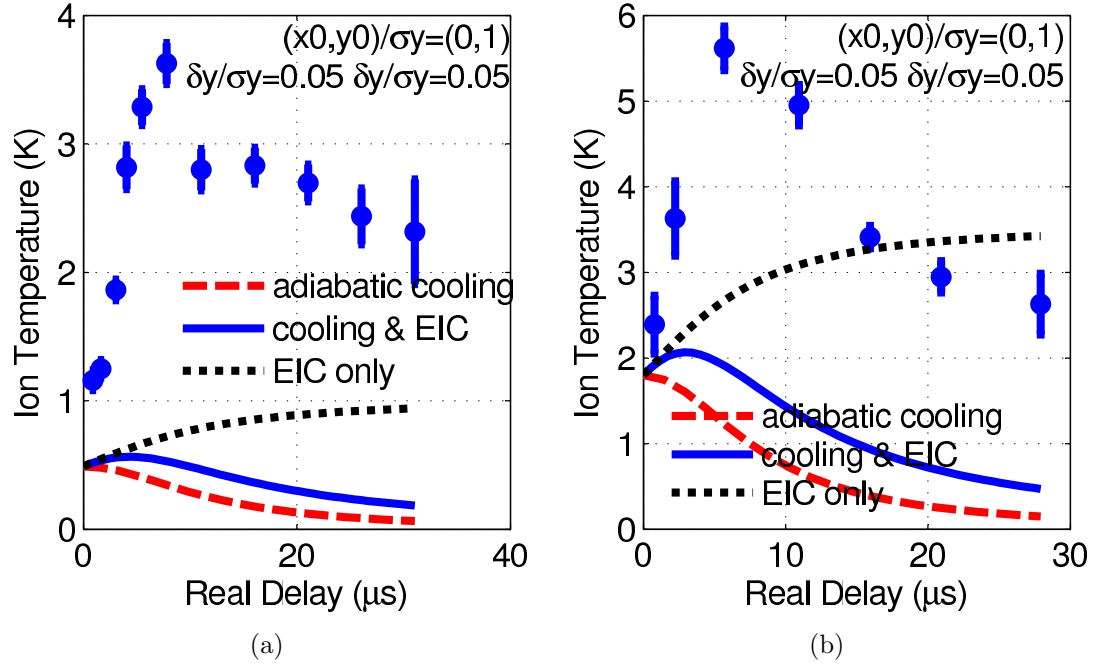


Figure 7.15: Thermal temperature variation in outer regions. The figure on the left has initial parameters as $n_0 = 2.8e15 \pm 0.2 \times 10^{15} \text{ m}^{-3}$, and initial size, $\sigma_0 = 1.2 \pm 0.1 \text{ mm}$ and that on the right has those as $n_0 = 18 \pm 0.2 \times 10^{15} \text{ m}^{-3}$, and initial size, $\sigma_0 = 0.84 \pm 0.1 \text{ mm}$. Both have initial electron temperature as 100 K. The plots show the thermal temperature at $y = \sigma$ having $\Delta = 0.05\sigma$.

excess heating that we see in our temperatures. Playing with the proportions of the adiabatic cooling rate and EIC rate, I saw that for the 48 K data set, if we have the adiabatic cooling rate as 0.9 times the actual rate (as given by Eqn. 7.3), and the EIC rate as 3 times the actual rate (as given by Eqn. 7.3), then, the resultant calculated temperature will be able to explain the thermal temperature data to some extent (see figure 7.16). But on the other hand, the same modified rates of cooling and EIC are not able to explain the temperature behavior of the 100 K data. In fact, in this case, if we change the cooling rate to 0.9 times of the actual and the EIC rate to 9 times of the actual, then the calculated temperatures come close to the observed values.

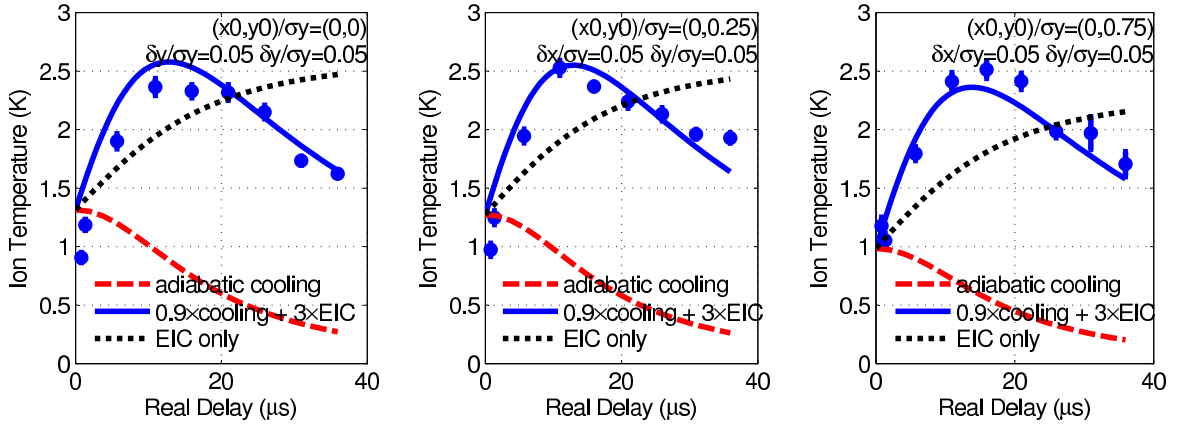


Figure 7.16: Calculating thermal temperature with modified cooling and EIC rates. The continuous blue line shows the calculated thermal temperature (using Eqn. 7.3) if we have the adiabatic cooling rate as 0.9 times the actual rate, and the EIC rate as 9 times the actual rate. The markers are experimental thermal temperature data of our plasma whose initial parameters are $2E_e/3k_B = 48 \pm 3$ K, initial peak ion-density of $n_0 = 5.1 \pm 0.2 \times 10^{15} \text{ m}^{-3}$, and initial size, $\sigma_0 = 1.25 \pm 0.1$ mm.

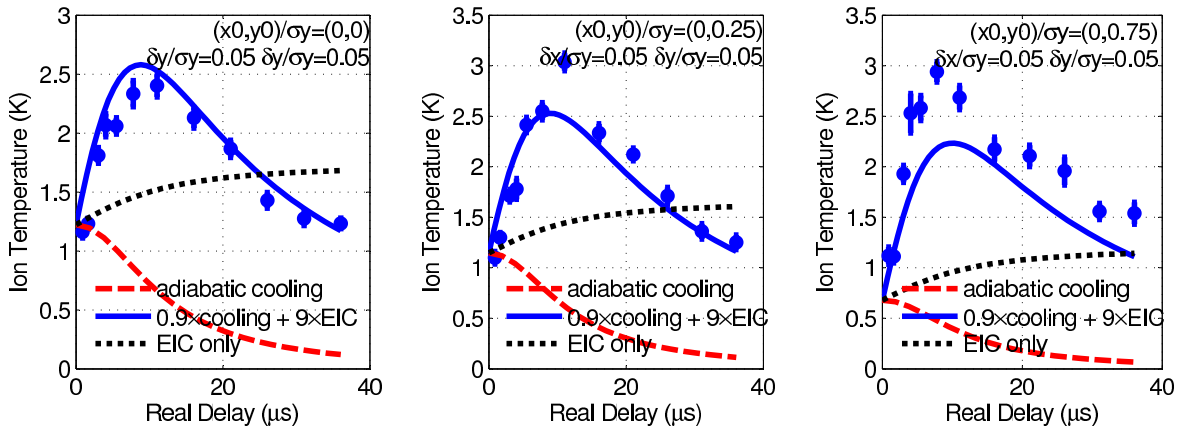


Figure 7.17: Calculating thermal temperature with modified cooling and EIC rates. The continuous blue line shows the calculated thermal temperature (using Eqn. 7.3) if we have the adiabatic cooling rate as 0.8 times the actual rate, and the EIC rate as 3 times the actual rate. The markers are experimental thermal temperature data of our plasma whose initial parameters are $2E_e/3k_B = 105 \pm 3$ K, initial peak ion-density of $n_0 = 2.8e15 \pm 0.2 \times 10^{15} \text{ m}^{-3}$, and initial size, $\sigma_0 = 1.2 \pm 0.1$ mm.

Chapter 8

Conclusion

To conclude, I would like to say that we have successfully developed and used absorption and fluorescence imaging to probe ultracold plasma characteristics. We are now in a better position to talk about plasma expansion in general and how to relate that expansion to ion thermal temperature in particular.

We have also found a very good technique of spatially resolved spectroscopy using a fluorescence imaging probe. With this technique we have been successfully able to resolve the expansion energy as Doppler shift rather than Doppler broadening in the spectrum. With this feature, we have been able to extract the value of small ion thermal temperature from large expansion energy. Studying the ion thermal temperature can lead us to greater depth of ultracold neutral plasma physics. The theory to fit the data needs work though, but I hope that it will throw more light on our understanding of physics.

By using fluorescence imaging we have also been able to see self-similar Gaussian expansion of our plasma. With this we have also been able to verify an exact analytical solution of Vlasov equations in UCNP.

All this understanding of our probes and the ultracold plasma will greatly benefit our lab in future work such as laser cooling of strontium ions. Apart from better understanding of the physical principles, fluorescence probes can serve as a method to detect the thermal temperature of ions during laser cooling, and thus, we can verify if we are able to cool the ions.

Appendix A

Code to calculate T_i using equation 3.1

The following is the Matlab code for TionofrTevector.m

```
function TionofrTevector=myfunction(peakdens,rhovector,z,Telec,sigi)
% This program calculates the thermalization temperature using Murillo's formula.
% The inputs to this program are : peak density on ions(peakdens) in m.-3,
% Electron temperature (Telec) in K and the ion cloud size, sigma (sigi) in m.
% This program accepts a vector rhovector (which is useful when dblquad.m
% calls it), a scalar z, both in m, (r.2=rhovector.2+z.2) and returns a
% vector TionofrTevector of the same size as rhovector.
% This program also calls another function uex.m
for i=1:length(rhovector)
    rho=rhovector(i);
%    sigi=1; % sigi=1, if rho and z are in units of sigi
    ec=1.6e-19; epton=8.85e-12;
    kb=1.38e-23; precision=1e-5;
%    n=peakdens.*exp(-(rho2+z2)/2/sigi2);
```

```

n=peakdens.*exp(-(rho^2+z^2)/2/sigi^2)+eps;

Te=Telec;

a=(3/(4*pi*n))^(1/3);

lambda=(epson*kb*Te/(n*ec^2))^(0.5);

k=a/lambda;

T0=2/3*(ec^2/(4*pi*epson*a*kb))*0.5;

Gamma0=ec^2/(4*pi*epson*kb*T0*a);

T1=2/3*(ec^2/(4*pi*epson*a*kb))*abs(uex(k,Gamma0)+k/2); % Initial guess

delta=abs((T1-T0)/T0);

count=1;

while((delta>precision)&(count<200)) % recursive approaching the solution

    Gamma1=ec^2/(4*pi*epson*kb*T1*a);

    sma=abs(uex(k,Gamma1)+k/2);

    T2=2/3*(ec^2/(4*pi*epson*a*kb))*sma;

    delta=abs((T2-T1)/T1);

    count=count+1;

    T1=T2;

end

TionofrTevector(i)=T1;

end

```

The following is the Matlab code for uex.m

```
% Based on J. Chem. Phys. 101,9885(1994) (Ref A),  
% J. Chem. Phys. 105,7641(1996) (Ref B) and PRE 56, 4671(1997) (Ref C)
```

```
function uex=myfunction(kapa,gamma);
```

```
k=kapa;
```

```
g=gamma;
```

```
s=1/3;
```

```
kb=1.38e-23;
```

```
if (g>1)
```

```
    if (k<=1) % Ref B formula 11-16
```

```
        da=-0.003366+0.00066*k^2-0.000089*k^4;
```

```
        Ebcc=-0.895929-0.103731*k^2+0.003084*k^4-0.000131*k^6;
```

```
        a=Ebcc+da;
```

```
        b=0.565004-0.026134*k^2-0.002689*k^4;
```

```
        c=-0.206893-0.086384*k^2+0.018278*k^4;
```

```
        d=-0.031402+0.042429*k^2-0.008037*k^4;
```

```
    end
```

```

if(k>1) % Ref C Table VIII, and polynomial fitting

    a=-0.0007*k^4+0.0154*k^3-0.1305*k^2+0.0228*k-0.9065;

    b=-0.0046*k^4+0.0538*k^3-0.2265*k^2+0.2812*k+0.4314;

    c=0.0044*k^4-0.045*k^3+0.2126*k^2-0.5031*k+0.0565;

    d=-0.0011*k^4+0.0057*k^3-0.0209*k^2+0.1406*k-0.1202;

    % this function form is only good for k<3.6

end

uex=(a*g+b*g^s+c+d*g^(-s))/g;

elseif ((g<=1)&(g>0)) %Ref A, Table IV and Ref C, Table VI

    gmatrix=[0 0.1 0.2 0.4 0.6 0.8 1];

    kmatrix=[0 0.2 0.4 0.6 0.8 1 1.2 1.4 2 2.6 3 3.6 4 4.6 5];

    umatrix=[0 -0.2652 -0.3483 -0.4431 -0.4962 -0.5406 -0.5717
              -0.1 -0.2809 -0.36 -0.4509 -0.5088 -0.5476 -0.5787
              -0.2 -0.3294 -0.394 -0.4794 -0.5319 -0.5708 -0.5991
              -0.3 -0.392 -0.452 -0.5251 -0.5732 -0.6087 -0.6317

```

```
-0.4 -0.475 -0.5195 -0.5799 -0.6238 -0.6561 -0.6788
-0.5 -0.5578 -0.5964 -0.6481 -0.6846 -0.7139 -0.7342
-0.6 -0.648425 -0.680595 -0.724539 -0.757346 -0.782004 -0.797097
-0.7 -0.740415 -0.770037 -0.806296 -0.831754 -0.852470 -0.869746
-1 -1.025685 -1.042716 -1.06775 -1.085879 -1.099115 -1.110066
-1.3 -1.319127 -1.331495 -1.348344 -1.360226 -1.369705 -1.377115
-1.5 -1.517696 -1.527809 -1.540813 -1.549763 -1.558136 -1.563017
-1.8 -1.815104 -1.821103 -1.831725 -1.83661 -1.843731 -1.847809
-2 -2.009731 -2.01827 -2.027327 -2.033013 -2.037149 -2.040283
-2.3 -2.30972 -2.315081 -2.321292 -2.327181 -2.329887 -2.332756
-2.5 -2.50901 -2.512796 -2.520736 -2.523305 -2.525945 -2.528765];
```

```
uex=interp2(gmatrix,kmatrix,umatrix,g,k,'spline');
```

```
% It is good only for k<5.
```

```
else %g==0
```

```
    uex=-k/2;
```

```
end
```

Appendix B

Analysis of plasma image strip with smaller strip width

In Chapter 7 (section 7.1), the result of the analysis using strip was shown for which the strip width was equal to 2.6 mm (figures 7.1, 7.2 and 7.3). We had chosen such a wide width so that the signal-to-noise be better. Some spatial information which might arise due to shock waves (or, for any reason) could be lost in areal density profile thus obtained, whose features are smaller than the strip width.

Thus, here, I am presenting results from such an analysis where the strip is equal to $52 \mu\text{m}$ (one-fortieth of the width used in the analysis of section 7.1). It should be noted here that the width of $52 \mu\text{m}$ corresponds to 2 pixels on our plasma image, thus making this the minimum width of the strip (so that some averaging can be performed). It can be seen from the figures here, that there are no extra spatial features which are not present in the corresponding figures in section 7.1.

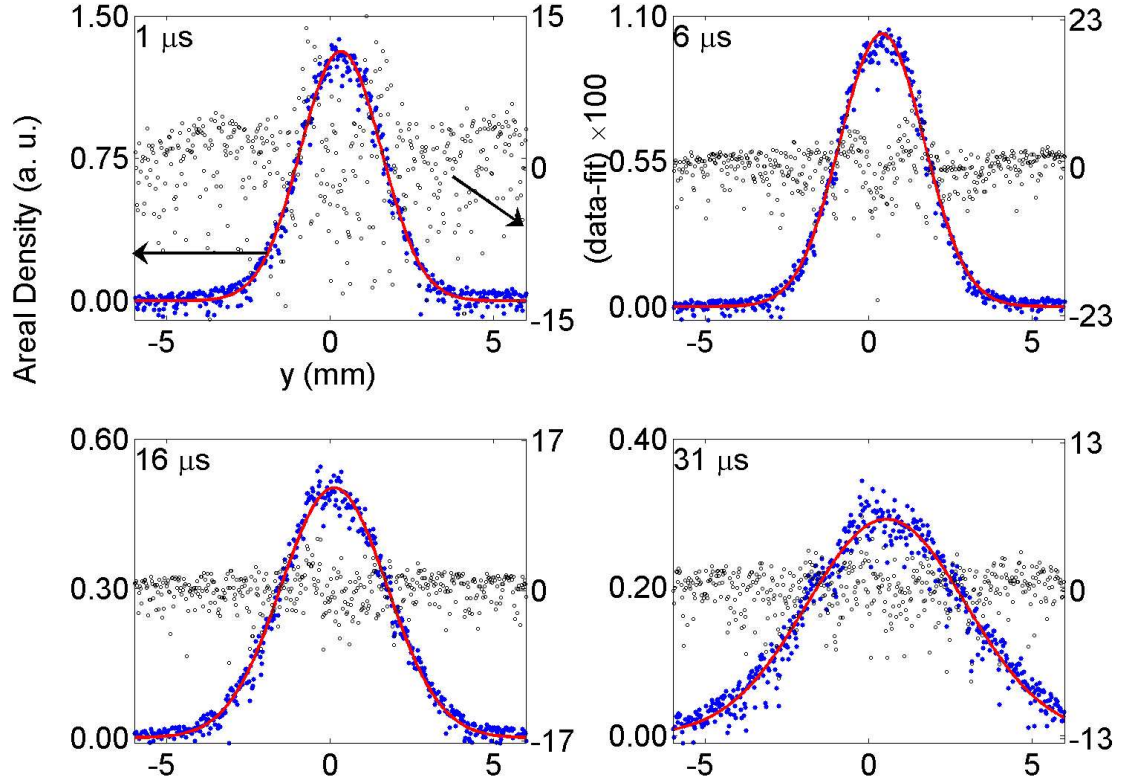


Figure B.1: Density profile of the plasma shows Gaussian expansion in our plasma. The closed markers are the experimental data points and the continuous curve is a Gaussian fit. The open circles are the residuals (data-fit) times 100. The data has initial electron temperature, $2E_e/3k_B = 48 \pm 3$ K, initial peak ion-density of $n_0 = 5.1 \pm 0.2 \times 10^{15} \text{ m}^{-3}$, and initial size, $\sigma_0 = 1.25 \pm 0.1$ mm.

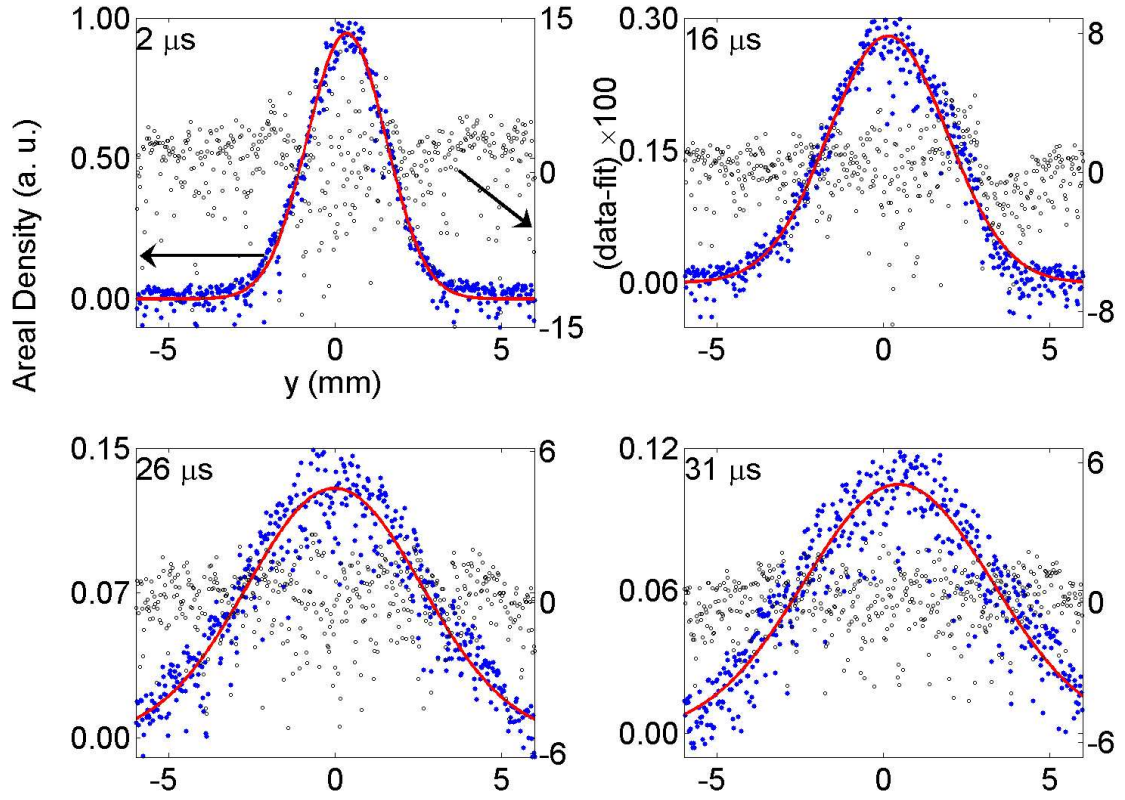


Figure B.2: Density profile of the plasma shows Gaussian expansion in our plasma. The closed markers are the experimental data points and the continuous curve is a Gaussian fit. The open circles are the residuals (data-fit) times 100. The data has initial electron temperature, $2E_e/3k_B = 105 \pm 3$ K, initial peak ion-density of $n_0 = 2.8e15 \pm 0.2 \times 10^{15} \text{ m}^{-3}$, and initial size, $\sigma_0 = 1.2 \pm 0.1$ mm.

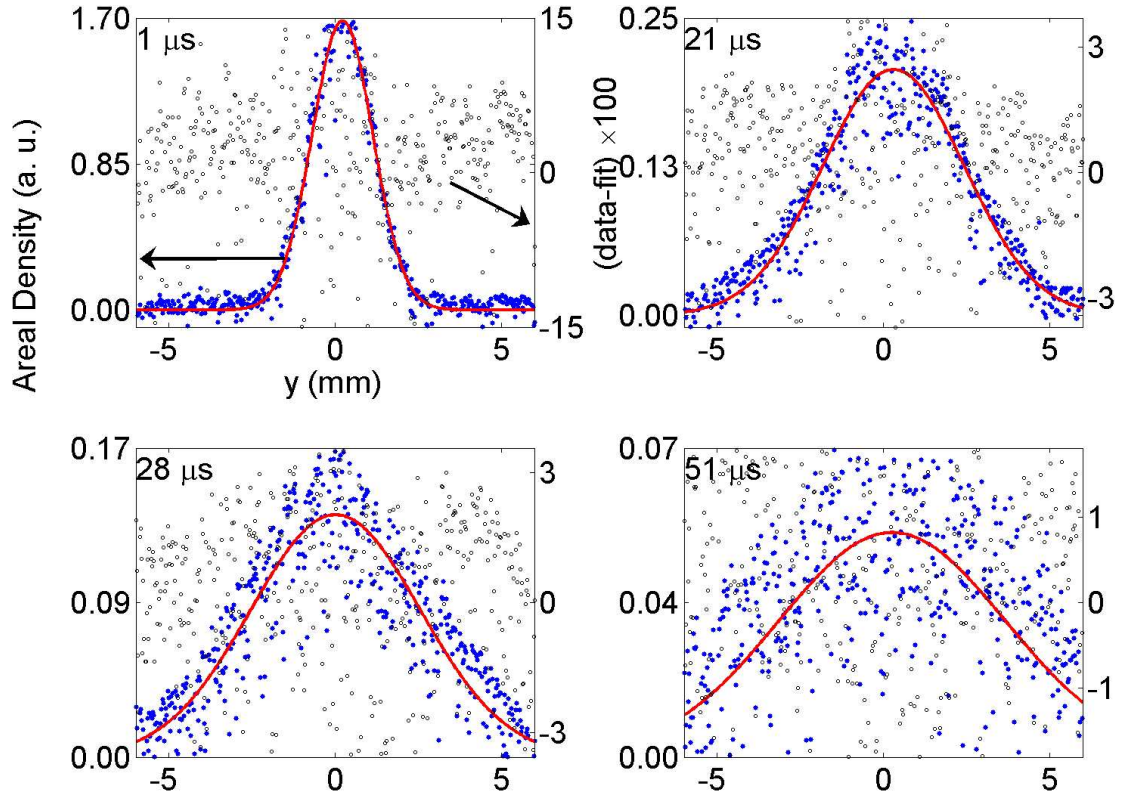


Figure B.3: Density profile of the plasma shows Gaussian expansion in our plasma. The closed markers are the experimental data points and the continuous curve is a Gaussian fit. The open circles are the residuals (data-fit) times 100. The data has initial electron temperature, $2E_e/3k_B = 105 \pm 3$ K, initial peak ion-density of $n_0 = 18 \pm 0.2 \times 10^{15} \text{ m}^{-3}$, and initial size, $\sigma_0 = 0.84 \pm 0.1$ mm.

Appendix C

Experimental Realization of an Exact Solution to the Vlasov Equations for an Expanding Plasma

This is the full text of the manuscript given in [27], which is also submitted to Physical Review Letters for publication.

Abstract: We study the expansion of ultracold neutral plasmas in the regime in which inelastic collisions are negligible. The plasma expands due to the thermal pressure of the electrons, and for an initial spherically symmetric Gaussian density profile, the expansion is self-similar. Measurements of the plasma size and ion kinetic energy using fluorescence imaging and spectroscopy show that the expansion follows an analytic solution of the Vlasov equations for an adiabatically expanding plasma.

Exactly solvable problems are rare in physics and serve as ideal models that provide a starting point for understanding more complex systems. Here, we report the experimental realization of a laser-produced plasma whose dynamics can be described by an analytic solution to the Vlasov equations [48, 26], which are central equations in the kinetic theory of plasmas. Expansion into a surrounding vacuum is fundamentally important and typically dominates the dynamics of plasmas created with

pulsed lasers [49], such as in experiments pursuing inertial confinement fusion [50], x-ray lasers [51], or the production of energetic ($> \text{MeV}$) ions through irradiation of solids [31, 52], thin foils [53, 54, 55, 32, 56, 57, 58], clusters [59].

We study plasma expansion with ultracold neutral plasmas (UNPs) [4, 60], which are created by photoionizing laser-cooled strontium atoms [13] just above the ionization threshold. The well-controlled initial conditions and relatively slow dynamics of these systems [20, 34] provide distinct advantages for studying this problem. In addition, we use fluorescence imaging and spectroscopy for the first time in UNPs. Although the typical energy and density of UNPs is much lower than in traditional hot plasmas produced by intense laser irradiation, the ratio of electron kinetic to potential energy and the resulting expansion dynamics is similar.

The investigation of plasma expansion dates back many decades [61, 62]. Recently, exact solutions for spatially finite plasmas expanding into vacuum were identified for a 1-dimensional plasmas [48] and later extended to 3-dimensions [26, 63]. This work was motivated by plasmas produced with short-pulse lasers.

The Vlasov equations, along with Poisson's equation, describe the evolution of electron ($\alpha = e$) and ion ($\alpha = i$) distribution functions, $f_\alpha(\mathbf{r}, \mathbf{v})$. The Vlasov equations neglect radiative processes and collisional phenomena such as electron-ion thermalization and three-body recombination [64], but they describe many types of plasmas and are part of the foundation of kinetic theory.

Among broad classes of general analytic solutions to the Vlasov equations [63],

UNPs realize a particular solution that is valid for a quasi-neutral plasma with spherical Gaussian distribution functions

$$f_\alpha \propto \exp \left[-\frac{r^2}{2\sigma^2} - \frac{m_\alpha(\mathbf{v} - \mathbf{u})^2}{2k_B T_\alpha} \right]. \quad (\text{C.1})$$

Quasi-neutrality is defined by $n_e \approx n_i$, where electron and ion densities are $n_\alpha(\mathbf{r}) = \int d\mathbf{v} f_\alpha(\mathbf{r}, \mathbf{v})$. T_α are electron and ion temperatures, and the local average velocity varies in space according to $\mathbf{u}(\mathbf{r}, t) = \gamma(t)\mathbf{r}$. The temperatures must scale as $\sigma^2 T_\alpha = \text{constant}$ [48], which is expected for adiabatic cooling in a spherical UNP [23, 65].

Under these conditions, the plasma dynamics is given by $T_\alpha(t) = T_\alpha(0)/(1 + t^2/\tau_{\text{exp}}^2)$, where the characteristic expansion time τ_{exp} is given by $\tau_{\text{exp}} = \sqrt{m_i \sigma(0)^2 / k_B [T_e(0) + T_i(0)]}$. Also,

$$\sigma(t)^2 = \sigma(0)^2 (1 + t^2/\tau_{\text{exp}}^2), \quad (\text{C.2})$$

and

$$v_{i,rms} = \sqrt{\frac{k_B}{m_i} \left\{ \frac{t^2}{\tau_{\text{exp}}^2} [T_e(t) + T_i(t)] + T_i(t) \right\}} \quad (\text{C.3})$$

describe the evolution of the characteristic plasma size and ion velocity. We define the rms 1-dimensional ion velocity $\sqrt{\langle (\mathbf{v} \cdot \hat{\mathbf{y}})^2 \rangle} \equiv v_{i,rms}$, where $\hat{\mathbf{y}}$ is the laser propagation direction, \mathbf{v} is the total ion velocity including random thermal motion and expansion, and angled brackets refer to an average over the distribution function.

The expansion is self-similar because thermal pressure produces a radial acceleration given by [26, 65]

$$\dot{\mathbf{u}} = -\frac{k_B [T_e(t) + T_i(t)]}{m_i} \frac{\nabla n(r, t)}{n(r, t)} = \frac{k_B [T_e(t) + T_i(t)]}{m_i \sigma(t)^2} \mathbf{r}. \quad (\text{C.4})$$

The simplification implied by the last equality is only valid for a spherical Gaussian plasma, and the linearity in \mathbf{r} preserves the shape of the distribution functions.

Plasmas produced with solid targets, foils, and clusters are often quasi-neutral and well-described by the Vlasov equations, and electrons typically cool adiabatically after the laser is extinguished [57, 56], but experimental conditions studied are typically very complicated and evolve extremely rapidly, which frustrates detailed comparison between experiment and theory. Final ion kinetic energy distributions have been shown to agree with simple models [56, 59], but in general, these systems lack the Gaussian distribution functions necessary to realize the analytically describable self-similar expansion [57].

For appropriate initial conditions, UNPs [4] fulfill the requirements for the analytic solution. In general, UNP peak densities are on the order of 10^{15} m^{-3} , and the profile follows that of the laser-cooled atom cloud, which we adjust to be a spherically symmetric Gaussian. The ion temperature is about 1 K determined by disorder-induced heating [6, 20]. Electron temperatures can range from 1 to 1000 K and are set by the detuning, E_e , of the ionization laser above threshold. For this study, we use intermediate initial electron temperatures ($\sim 100 \text{ K}$), which at this density are high enough to avoid

inelastic collisional and radiative processes [22, 66, 67, 23] but low enough to maintain quasi-neutrality [4]. The photoionization pulse length (~ 10 ns) is much less than the expansion time scale (~ 10 μ s).

The electron distribution equilibrates locally within 100 ns and globally within 1 μ s after photoionization [23, 65]. This ensures a Gaussian electron distribution function at the start of the expansion. Despite these very rapid electron-electron collisions the corresponding collision integral vanishes for the spherically symmetric, Gaussian velocity distribution eq.(1). Hence the highly collisional UNP considered here provides an ideal model system for truly collisionless plasmas behavior.

Ions reach local thermal equilibrium within a few 100 ns [20]. They do not equilibrate globally on the time scale of the expansion [34], but the ions are so cold compared to the electrons, that the lack of a global ion temperature does not cause any significant deviation from the exact solution. The low ion temperature also implies that the ions form a strongly coupled fluid [1, 20], which, however, negligibly affects the plasma expansion [65].

The analytic expansion solution has been discussed previously for UNPs [23, 65], and it has been checked against average terminal ion expansion velocities [22] and measured electron temperatures [25] that qualitatively affirm the importance of adiabatic cooling for appropriate initial conditions. The lack of spatial and temporal resolution, however, prevented conclusive tests of the analytic predictions. Cummings *et al.* [68, 69] adapted the formalism of [23, 65] and used light-scattering from

a small region of the plasma to study the expansion of ultracold plasmas with an elongated aspect ratio, but they found significant deviations from the predictions of the model that perhaps arose because the condition of spherical symmetry was not fulfilled.

To demonstrate that ultracold neutral plasmas can realize the analytic expansion solution, we will first describe our diagnostic and show that the plasma remains Gaussian during its expansion. Then we will show the size variation and ion velocity are given by Eqs. C.2 and C.3 respectively.

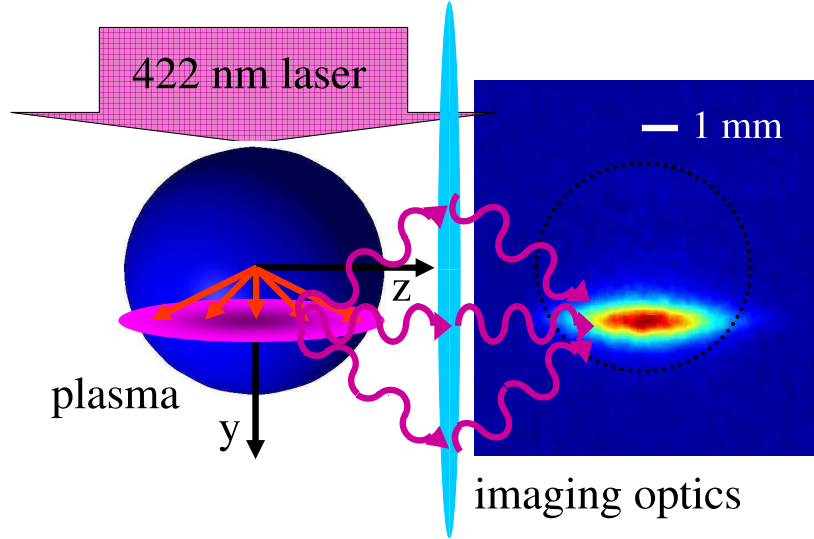


Figure C.1: Recording fluorescence of UNPs. The correlation between position and expansion velocity (red arrows) produces a striped image when the Doppler-shift due to expansion exceeds the Doppler broadening associated with thermal ion velocity. The number of ions in the plasma shown is 2×10^8 , and it can be calibrated absolutely with absorption imaging [20]. The fluorescence laser is blue-detuned by 193 MHz from resonance. We collect about 1% of the scattered photons due to solid angle limitations. The theoretically expected resolution is $40 \mu\text{m}$ for our optical setup.

Figure C.1 shows a schematic of the fluorescence imaging experiment. A laser beam that is near resonance with the $^2S_{1/2} - ^2P_{1/2}$ transition in Sr^+ at $\lambda = 422 \text{ nm}$

propagates along \hat{y} and illuminates the plasma. Fluorescence in a perpendicular direction (\hat{z}) is imaged with a 1:1 relay telescope onto an image-intensified CCD camera. The 422 nm light is typically applied in a $1\ \mu\text{s}$ pulse to provide temporal resolution, with an intensity of a few mW/cm^2 .

A general expression for the fluorescence is

$$F(\nu, x, y) \propto \int ds \frac{1}{1 + \left[\frac{2(\nu-s)}{\gamma_{eff}/2\pi} \right]^2} \times \int \frac{dz n(\mathbf{r})}{\sqrt{2\pi}\sigma_D [T_{i,therm}(\mathbf{r})]} \exp \left\{ - \frac{[s - (\nu_0 + \nu_{exp}^y(\mathbf{r}))]^2}{2\sigma_D^2 [T_{i,therm}(\mathbf{r})]} \right\}, \quad (\text{C.5})$$

where ν is the laser frequency and $\gamma_{eff} = \gamma_0 + \gamma_{laser}$ is the sum of the natural linewidth of the transition ($2\pi \times 20\ \text{MHz}$) and the imaging laser linewidth ($2\pi \times 8\ \text{MHz}$). $T_{i,therm}(\mathbf{r})$ is the local temperature of the ions describing random thermal motion, which gives rise to the Doppler width σ_D . Due to the directed expansion velocity, the average resonance frequency of the transition for atoms at \mathbf{r} is Doppler-shifted from the unperturbed value, ν_0 , by $\nu_{exp}^y(\mathbf{r}) = \mathbf{u}(\mathbf{r}) \cdot \hat{y}/\lambda$. The spatial variation in $T_{i,therm} \sim n_i^{1/3}$ [34] is small compared to the directed expansion energy, so $T_{i,therm}$ can be taken as constant.

Images can be analyzed in several different ways, which each provide access to different plasma properties. Summing a series of images taken at equally spaced frequencies covering the entire ion resonance is equivalent to integrating $F(\nu, x, y)$ over frequency. This yields a signal proportional to the areal plasma density, $\int n(x, y, z) dz$,

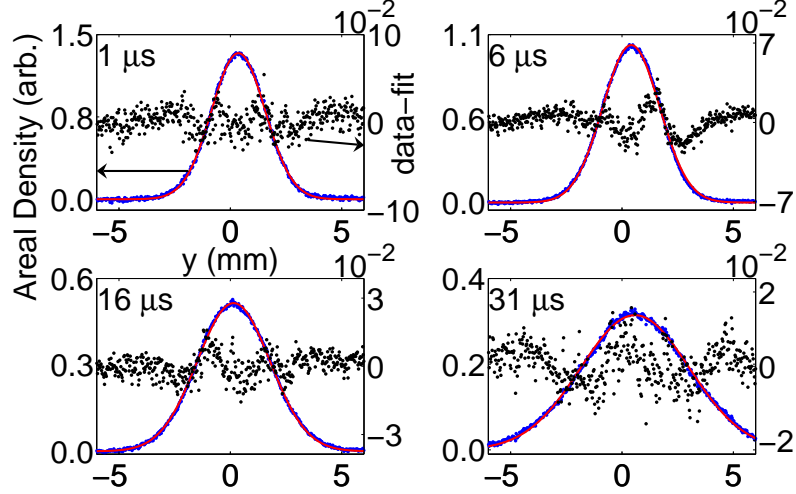


Figure C.2: Evolution of the areal density for a plasma with $1.6 \pm 0.1 \times 10^8$ ions, $2E_e/3k_B = 48 \pm 3$ K, and $\sigma(0) = 1.3 \pm 0.1$ mm. The areal density (arbitrary units) is found by summing together 50 images taken at equally spaced frequencies that fully cover the ion resonance. The Gaussian fits (solid line) to linear cuts show that the expansion is self-similar. The time indicated is the evolution time since plasma creation. The right-hand axes show that the differences between data and fit are small.

which for a Gaussian density distribution should take the form

$$n_{areal}(x, y) = \sqrt{2\pi}\sigma n_0 \exp[-(x^2 + y^2)/2\sigma^2].$$

Figure C.2 shows that Gaussian fits of the areal density are excellent during more than a factor of two change in σ from the earliest times until the signal expands beyond the range of the imaging system. This provides direct confirmation of the self-similar nature of the expansion.

There is no sign of any deviation from the gaussian shape at large radius. This might seem surprising because self-similarity follows from Eq. C.4, and this equation must break down at large r where it implies unphysical accelerations arising from unphysically large electric fields. One would expect a breakdown where the plasma is not quasineutral, which should occur when the local Debye screening length exceeds

the length scale for ion density variation, or $\sigma < \lambda_D(r) = [\varepsilon_0 k_B T_e / n_e(r) e^2]^{1/2}$ for a Gaussian plasma. At the radius where $\sigma \approx \lambda_D(r)$, which is typically at $r \sim 4 \times \sigma$ for UNPs, the accelerating electric field reaches a maximum of $\sim k_B T_e / e \lambda_D$, identical to peak accelerating fields in plasmas generated from foil targets [58]. A peak in the electric field can lead to wave-breaking, shock waves, and the formation of an ion front as seen in theories for UNPs [23, 65] and traditional short-pulse laser-produced plasmas [57, 70], and can determine the maximum ion kinetic energy [56]. The lack of such features in data such as Fig. C.2 confirms the extent of quasineutrality one would expect for such a low electron temperature [23] and may also suggest that finite ion temperature and strong coupling effects damp wave-breaking at the plasma edge [65].

The evolution of σ (Fig. C.3) can be extracted from fits such as Fig. C.2. Again, data evolve as predicted by theory. Higher electron temperature and smaller size lead to a faster expansion because this increases the thermal pressure (Eq. C.4). Fits of the data using Eq. C.2 yield values of $T_e(0)$ that agree reasonably well with the expected values of $2E_e/3k_B$. This confirms that on the time scale of the expansion there are no significant collisional or radiative processes changing the electron temperature such as three-body recombination or electron-ion thermalization, as assumed in the Vlasov equations.

In order to completely characterize the plasma expansion we also measure the light-scattering resonance spectrum, formed from the integrated fluorescence in each

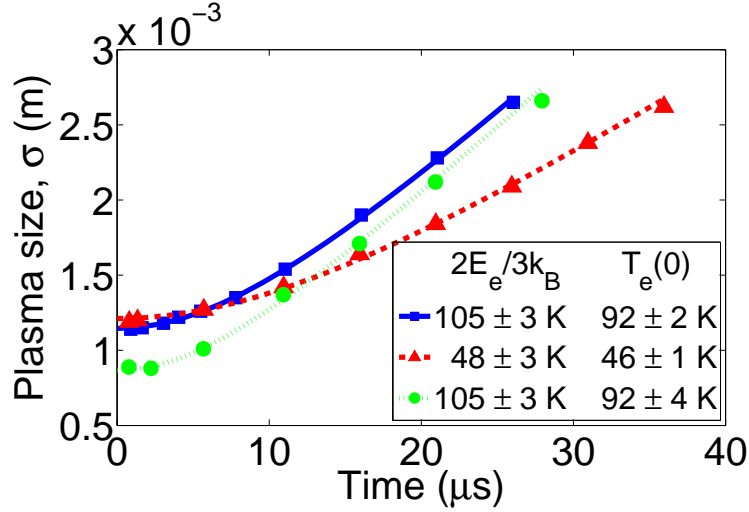


Figure C.3: Evolution of the plasma size, extracted from fits such as in Fig. C.2. $T_e(0)$ and $\sigma(0)$ are fit, while $T_i(0)$ is taken from the theoretical expression for disorder-induced heating [6, 20]. Uncertainties in $2E_e/3k_B$ reflect 1-standard-deviation calibration uncertainty in the wavelength of the photoionizing laser. Quoted uncertainties in $T_e(0)$ are statistical, but there is an additional systematic uncertainty of a few percent arising from calibration of the imaging-system magnification and overlap of the plasma and fluorescence excitation laser. Statistical uncertainty in the measurement of σ is less than the size of the plotting symbols. Initial peak densities for these samples are $\sim 10^{16} \text{ m}^{-3}$.

of a series of images taken at different frequencies, as shown in Fig. C.4A. Eq. C.5, combined with the expansion velocity $\mathbf{u}(\mathbf{r})$ predicted by the Vlasov equations, implies that the resulting signal ($\int dx dy F(\nu, x, y)$) should take the form of a Voigt profile. The rms width of the Gaussian component of this profile arising from Doppler broadening reflects both thermal ion motion and directed expansion and is given by

$$\tilde{\sigma}_D = v_{i,rms}/\lambda.$$

Equation C.3 provides an excellent fit to the data, and the extracted values of $T_e(0)$ are consistent with $2E_e/3k_B$ within experimental uncertainty. The small initial offset of $v_{i,rms}$ in each plot is due to disorder-induced heating of the ions within the first microsecond [20], which locally produces a thermal ion velocity distribution. But

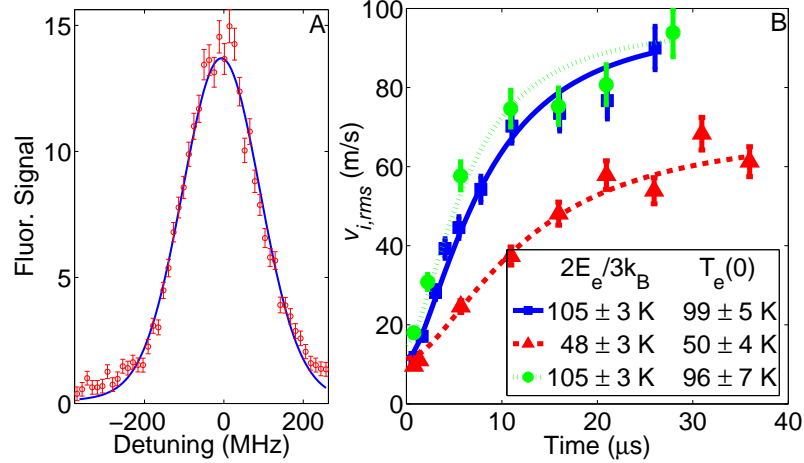


Figure C.4: (A) Sample spectrum and (B) evolution of the rms ion velocity ($v_{i,rms}$). (A) Spectrum for $2E_e/3k_B = 105 \pm 3$ K, peak ion density of $3 \times 10^{15} \text{ m}^{-3}$, and plasma evolution time of $3 \mu\text{s}$. Fits to a Voigt profile provide $v_{i,rms}$. (B) The velocity evolution is fit well by Eq. C.3 with $T_e(0)$ as a fit parameter, $\sigma(0)$ determined from the cloud size measurements (Fig. C.3), and $T_i(0)$ taken from the theoretical expression for disorder-induced heating [6, 20].

$v_{i,rms}$ quickly increases well above this value as the electron pressure drives the plasma expansion and electron thermal energy is converted into directed radial ion velocity. As σ increases and the electrons cool adiabatically, the acceleration decreases (Eq. C.4) and the ions eventually reach terminal velocity when essentially all electron kinetic energy is transferred to the ions.

Our measured density profiles (Fig. C.3) confirm the validity of Eq. C.3, which shows that the ion acceleration is sensitive at all times to the instantaneous electron temperature and width of the plasma. Agreement between experiment and theory for both the size evolution and the ion velocity dynamics hence demonstrates that $T_e(t)$ also follows the dynamics predicted by the analytical solution to the Vlasov equations.

We have demonstrated a plasma in which the expansion matches an analytic solution to the Vlasov equations [26] proposed as a basic model for the dynamics of quasineutral laser-produced plasmas. To realize this situation, it is necessary to create UNPs with a spherical Gaussian density distribution and appropriate density and electron temperature to avoid inelastic collisions that would heat electrons or lead to electron-ion equilibration. The expansion dynamics shown here provide a general tool for developing a greater understanding and intuition for complex systems, and they should provide insight on the implications when initial conditions deviate from what is required for validity of the analytic solution. Important examples are higher energy plasmas that evolve rapidly and have initial geometries that are difficult to model, or UNPs with lower initial T_e and higher density in which inelastic collisions can increase electron temperature by an order of magnitude or more [71].

This work was supported by the National Science Foundation (Grants PHY-0355069 and PHY-0140320) and the David and Lucille Packard Foundation.

Bibliography

- [1] S. Ichamuru. Strongly coupled plasmas: high-density classical plasmas and degenerate electron liquids. *Rev. Mod. Phys.*, 54(4):1017, 1982.
- [2] J. H. Chu and Lin I. Direct observation of coulomb crystals and liquids in strongly coupled rf dusty plasmas. *Phys. Rev. Lett.*, 72(25):4009–4012, Jun 1994.
- [3] S. Laha, Y.C. Chen, P. Gupta, C.E. Simien, Y.N. Martinez, P.G. Mickelson, S.B. Nagel, and T.C. Killian. Kinetic energy oscillations in annular regions of ultracold neutral plasmas. *Eur. Phys. J. D*, 40:51–56, 2006.
- [4] T. C. Killian, S. Kulin, S. D. Bergeson, L. A. Orozco, C. Orzel, and S. L. Rolston. Creation of an ultracold neutral plasma. *Phys. Rev. Lett.*, 83(23):4776, 1999.
- [5] A. E. Leanhardt, T. A. Pasquini, M. Saba, A. Schirotzek, Y. Shin, D. Kielpinski, D. E. Pritchard, and W. Ketterle. Cooling Bose-Einstein Condensates Below 500 Picokelvin. *Science*, 301(5639):1513–1515, 2003.
- [6] M. S. Murillo. Using Fermi statistics to create strongly coupled ion plasmas in atom traps. *Phys. Rev. Lett.*, 87(11):115003, 2001.
- [7] W. Ertmer, R. Blatt, J. L. Hall, and M. Zhu. Laser manipulation of atomic

- beam velocities: Demonstration of stopped atoms and velocity reversal. *Phys. Rev. Lett.*, 54(10):996–999, Mar 1985.
- [8] William D. Phillips and Harold Metcalf. Laser deceleration of an atomic beam. *Phys. Rev. Lett.*, 48(9):596–599, Mar 1982.
- [9] A. L. Migdall, J. V. Prodan, W. D. Phillips, T. H. Bergeman, and H. J. Metcalf. First observation of magnetically trapped neutral atoms. *Phys. Rev. Lett.*, 54(24):2596, 1985.
- [10] Steven Chu, J. E. Bjorkholm, A. Ashkin, and A. Cable. Experimental observation of optically trapped atoms. *Phys. Rev. Lett.*, 57(3):314–317, Jul 1986.
- [11] E. L. Raab, M. Prentiss, A. Cable, S. Chu, and D. E. Pritchard. Trapping of neutral sodium atoms with radiation pressure. *Phys. Rev. Lett.*, 59(23):2631, 1987.
- [12] H. J. Metcalf and P. van der Straten. *Laser Cooling and Trapping*. Springer-Verlag New York, New York, 1999.
- [13] S. B. Nagel, C. E. Simien, S. Laha, P. Gupta, V. S. Ashoka, and T. C. Killian. Magnetic trapping of metastable 3P_2 atomic strontium. *Phys. Rev. A*, 67:011401, 2003.
- [14] Priya Gupta. Pulsed dye laser for excitation of strontium. Master’s thesis, Rice University, 2004.

- [15] T. F. Gallagher. *Rydberg Atoms*. Cambridge University Press, 1994.
- [16] M. P. Robinson, B. L. Tolra, M. W. Noel, T. F. Gallagher, and P. Pillet. Spontaneous evolution of rydberg atoms into an ultracold plasma. *Phys. Rev. Lett.*, 85(21):4466, 2000.
- [17] F. Robicheaux and J. D. Hanson. Simulation of the expansion of an ultracold neutral plasma. *Phys. Rev. Lett.*, 88(5):55002, 2002.
- [18] E. A. Cummings, J. E. Daily, D. S. Durfee, and S. D. Bergeson. Fluorescence measurements of expanding strongly-coupled neutral plasmas. *Phys. Rev. Lett.*, 95:235001, 2005.
- [19] G. Kalman, M. Rosenberg, and H. E. DeWitt. Collective modes in strongly correlated yukawa liquids: Waves in dusty plasmas. *Phys. Rev. Lett.*, 84(26):6030–6033, Jun 2000.
- [20] C. E. Simien, Y. C. Chen, P. Gupta, S. Laha, Y. N. Martinez, P. G. Mickelson, S. B. Nagel, and T. C. Killian. Using absorption imaging to study ion dynamics in an ultracold neutral plasma. *Phys. Rev. Lett.*, 92(14):143001, 2004.
- [21] T. Pohl, T. Pattard, and J. M. Rost. Coulomb crystallization in expanding laser-cooled neutral plasmas. *Phys. Rev. Lett.*, 92(15):155003, 2004.
- [22] S. Kulin, T. C. Killian, S. D. Bergeson, and S. L. Rolston. Plasma oscillations and expansion of an ultracold neutral plasma. *Phys. Rev. Lett.*, 85(2):318, 2000.

- [23] F. Robicheaux and J. D. Hanson. Simulated expansion of an ultra-cold, neutral plasma. *Phys. Plasmas*, 10(6):2217, 2003.
- [24] P. Gupta, S. Laha, C. E. Simien, H. Gao, J. Castro, T. Pohl, and T. C. Killian. Electron temperature evolution in expanding ultracold neutral plasmas, 2007. arXiv:0705.3416v1. Submitted to *Phys. Rev. Lett.*
- [25] J. L. Roberts, C. D. Fertig, M. J. Lim, and S. L. Rolston. Electron temperature of ultracold plasmas. *Physical Review Letters*, 92(25):253003, 2004.
- [26] D. S. Dorozhkina and V. E. Semenov. Exact solution of vlasov equations for quasineutral expansion of plasma bunch into vacuum. *Phys. Rev. Lett.*, 81(13):2691, 1998.
- [27] S. Laha, P. Gupta, C. E. Simien, H. Gao, J. Castro, T. Pohl, and T. C. Killian. Experimental realization of an exact solution to the vlasov equations for an expanding plasma, 2007. arXiv:0705.3416v1. Submitted to *Phys. Rev. Lett.*
- [28] Patrick Mora and R. Pellat. Self-similar expansion of a plasma into a vacuum. *Physics of Fluids*, 22(12):2300–2304, 1979.
- [29] H. Luo and M. Y. Yu. Self-similar expansion of dusts in a plasma. *Physics of Fluids B: Plasma Physics*, 4(10):3066–3069, 1992.
- [30] P. Mora. Plasma expansion into a vacuum. *Phys. Rev. Lett.*, 90(18):185002, May 2003.

- [31] E. L. Clark, K. Krushelnick, M. Zepf, F. N. Beg, M. Tatarakis, A. Machacek, M. I. K. Santala, I. Watts, P. A. Norreys, and A. E. Dangor. Energetic heavy-ion and proton generation from ultraintense laser-plasma interactions with solids. *Phys. Rev. Lett.*, 85(8):1654–1657, Aug 2000.
- [32] L. Romagnani, J. Fuchs, M. Borghesi, P. Antici, P. Audebert, F. Ceccherini, T. Cowan, T. Grismayer, S. Kar, A. Macchi, P. Mora, G. Pretzler, A. Schiavi, T. Toncian, and O. Willi. Dynamics of electric fields driving the laser acceleration of multi-mev protons. *Physical Review Letters*, 95(19):195001, 2005.
- [33] L. M. Wickens, J. E. Allen, and P. T. Rumsby. Ion emission from laser-produced plasmas with two electron temperatures. *Phys. Rev. Lett.*, 41(4):243–246, Jul 1978.
- [34] Y. C. Chen, C. E. Simien, S. Laha, P. Gupta, Y. N. Martinez, P. G. Mickelson, S. B. Nagel, and T. C. Killian. Electron screening and kinetic energy oscillations in a strongly coupled plasma. *Phys. Rev. Lett.*, 93:265003, 2004.
- [35] T Pattard T Pohl and J M Rost. Influence of electron-ion collisions on coulomb crystallization of ultracold neutral plasmas. *Journal of Physics B: Atomic, Molecular and Optical Physics*, 38(2):S343–S350, 2005.
- [36] Priya Gupta. *Expansion and Electron Temperature Evolution in an Ultracold Neutral Plasma*. PhD thesis, Rice University, 2007.

- [37] S. Hamaguchi, R. T. Farouki, and D. H. E. Dubin. Triple point of Yukawa systems. *Phys. Rev. E*, 56(4):4671, 1997.
- [38] L. Tonks and I. Langmuir. Oscillations in ionized gases. *Phys. Rev.*, 33(2):195, 1929.
- [39] W. D. Jones, H. J. Doucet, and J. M. Buzzi. *An introduction to the linear theories and methods of electrostatic waves in plasmas*. Plenum Press, New York, 1985.
- [40] Sampad Laha. Kinetic energy oscillations in annular regions of an ultracold neutral plasma. Master’s thesis, Rice University, 2005.
- [41] T. C. Killian, Y. C. Chen, P. Gupta, S. Laha, Y. N. Martinez, P. G. Mickelson, S. B. Nagel, A. D. Saenz, and C. E. Simien. Absorption imaging and spectroscopy of ultracold neutral plasmas. *J. Phys. B*, 38:351, 2005. The RHS of Eqn. (7) in [41] needs to be multiplied by a factor of $\frac{\gamma_0}{\gamma_{eff}}$.
- [42] T. C. Killian, T. Pattard, T. Pohl, and J. M. Rost. Ultracold neutral plasmas, 2006. arXiv:physics/0612097v1.
- [43] Richard L. Liboff. *Kinetic theory*. John Wiley & Sons, Inc., 1998.
- [44] R. Piejak, V. Godyak, and B. Alexandrovich. The electric field and current density in a low-pressure inductive discharge measured with different b-dot probes. *Journal of Applied Physics*, 81(8):3416–3421, 1997.

- [45] Clayton Earl Simien. *Early Time Ion Dynamics and Progress Towards Laser cooling an Ultracold Neutral Plasma*. PhD thesis, Rice University, 2007.
- [46] Clayton Earl Simien. 422 nm laser. Master's thesis, Rice University, 2004.
- [47] A. E. Siegman. *Lasers*. University Science Books, Sausalito, California, 1986.
- [48] A. V. Baitin and K. M. Kuzanyan. A self-similar solution for expansion into a vacuum of a collisionless plasma bunch. *J. Plasma Phys.*, 59:83, 1998.
- [49] Michael D. Perry and Gerard Mourou. Terawatt to Petawatt Subpicosecond Lasers. *Science*, 264(5161):917–924, 1994.
- [50] John Lindl. Development of the indirect-drive approach to inertial confinement fusion and the target physics basis for ignition and gain. *Physics of Plasmas*, 2(11):3933–4024, 1995.
- [51] Hiroyuki Daido. Review of soft x-ray laser researches and developments. *Reports on Progress in Physics*, 65(10):1513–1576, 2002.
- [52] R. A. Snavely, M. H. Key, S. P. Hatchett, T. E. Cowan, M. Roth, T. W. Phillips, M. A. Stoyer, E. A. Henry, T. C. Sangster, M. S. Singh, S. C. Wilks, A. MacKinnon, A. Offenberger, D. M. Pennington, K. Yasuike, A. B. Langdon, B. F. Lasinski, J. Johnson, M. D. Perry, and E. M. Campbell. Intense high-energy proton beams from petawatt-laser irradiation of solids. *Phys. Rev. Lett.*, 85(14):2945–2948, Oct 2000.

- [53] A. Maksimchuk, S. Gu, K. Flipppo, D. Umstadter, and V. Yu. Bychenkov. Forward ion acceleration in thin films driven by a high-intensity laser. *Phys. Rev. Lett.*, 84(18):4108–4111, May 2000.
- [54] J. Badziak, E. Woryna, P. Parys, K. Yu. Platonov, S. Jabłoński, L. Ryć, A. B. Vankov, and J. Wołowski. Fast proton generation from ultrashort laser pulse interaction with double-layer foil targets. *Phys. Rev. Lett.*, 87(21):215001, Nov 2001.
- [55] J. Fuchs, Y. Sentoku, S. Karsch, J. Cobble, P. Audebert, A. Kemp, A. Nikroo, P. Antici, E. Brambrink, A. Blazevic, E. M. Campbell, J. C. Fernandez, J.-C. Gauthier, M. Geissel, M. Hegelich, H. Pepin, H. Popescu, N. Renard-LeGalloudec, M. Roth, J. Schreiber, R. Stephens, and T. E. Cowan. Comparison of laser ion acceleration from the front and rear surfaces of thin foils. *Physical Review Letters*, 94(4):045004, 2005.
- [56] M. Murakami, Y.-G. Kang, K. Nishihara, S. Fujioka, and H. Nishimura. Ion energy spectrum of expanding laser-plasma with limited mass. *Physics of Plasmas*, 12(6):062706, 2005.
- [57] P. Mora. Collisionless expansion of a gaussian plasma into a vacuum. *Physics of Plasmas*, 12(11):112102, 2005.
- [58] T. Grismayer and P. Mora. Influence of a finite initial ion density gradient on plasma expansion into a vacuum. *Physics of Plasmas*, 13(3):032103, 2006.

- [59] D. R. Symes, M. Hohenberger, A. Henig, and T. Ditmire. Anisotropic explosions of hydrogen clusters under intense femtosecond laser irradiation. *Physical Review Letters*, 98(12):123401, 2007.
- [60] Thomas C. Killian. Ultracold Neutral Plasmas. *Science*, 316(5825):705–708, 2007.
- [61] A. V. Gurevich, L. V. Pariskaya, and L. P. Pitaevskii. *Sov. Phys. JETP*, 22:449, 1966.
- [62] Ch. Sack and H. Schamel. Plasma expansion into vacuum a hydrodynamic approach. *Phys. Rep.*, 156:311–395, 1987.
- [63] V. F. Kovalev and V. Yu. Bychenkov. Analytic solutions to the vlasov equations for expanding plasmas. *Phys. Rev. Lett.*, 90(18):185004, May 2003.
- [64] P. Mansbach and J. Keck. Monte Carlo trajectory calculations of atomic excitation and ionization by thermal electrons. *Phys. Rev.*, 181:275, 1969.
- [65] T. Pohl, T. Pattard, and J. M. Rost. Kinetic modeling and molecular dynamics simulation of ultracold neutral plasmas including ionic correlations. *Phys. Rev. A*, 70(3):033416, 2004.
- [66] S. G. Kuzmin and T. M. O’Neil. Numerical simulation of ultracold plasmas. *Phys. Plasmas*, 9(9):3743, 2002.

- [67] S. Mazevet, L. A. Collins, and J. D. Kress. Evolution of ultracold neutral plasmas. *Phys. Rev. Lett.*, 88(5):55001, 2002.
- [68] E. A. Cummings, J. E. Daily, D. S. Durfee, and S. D. Bergeson. Ultracold neutral plasma expansion in two dimensions. *Phys. Plasmas*, 12:123501, 2005.
- [69] E. A. Cummings, J. E. Daily, D. S. Durfee, and S. D. Bergeson. Ultracold neutral plasma expansion in two dimensions. *Physics of Plasmas*, 12(12):123501, 2005.
- [70] A. E. Kaplan, B. Y. Dubetsky, and P.L. Shkolnikow. Shock shells in coulomb explosions of nanoclusters. *Phys. Rev. Lett.*, 91(14):143401, 2003.
- [71] P. Gupta, S. Laha, C. E. Simien, H. Gao, J. Castro, T. Pohl, and T. C. Killian. Electron temperature evolution in expanding ultracold neutral plasmas, 2007. arXiv:0705.3416v1. Accepted in *Phys. Rev. Lett.*